ANALYTICAL AND EXPERIMENTAL ASSESSMENT OF AN AASHTO I-GIRDER TYPE I PRESTRESSED WITH AFRP TENDONS

A Thesis

by

WESLEY DAVID CUMMINGS

Submitted to the Office of Graduate and Professional Studies of
Texas A&M University
in partial fulfillment of the requirements for the degree of

MASTER OF SCIENCE

Chair of Committee,	Stefan Hurlebaus
Committee Members,	John B. Mander
	Anastasia H. Muliana
Head of Department,	Robin Autenrieth

December 2014

Major Subject: Civil Engineering

ABSTRACT

Corrosion induced deterioration is one of the main reason for repair and rehabilitation programs in conventional steel reinforced concrete bridge decks. Of all bridges in the United States, over 50 percent are constructed of conventional reinforced or prestressed concrete (NACE, 2013), where one in three bridges are considered structurally deficient or functionally obsolete due to corrosion of the steel reinforcement. According to NACE International (2013) the annual cost of corrosion-related maintenance for highway bridges in the U.S. is estimated at $13.6 billion.

Over the past couple of decades, fiber reinforced polymer (FRP) bars have been noted by researchers and engineers as a corrosion-resistant alternative for either conventional reinforcing steel or prestressing strands. High strength-to-weight ratio, corrosion resistance, ease in placement of the bars and accelerated implementation due to light weight are the special characteristics that make these bars an appealing alternative. Up to this end, extensive research has been conducted on the structural performance of FRP reinforced concrete beams and slabs; however, less attention has been paid to FRP reinforced concrete bridge girders in composite action with the bridge deck. Accounting for the effect of composite action between the bridge girder and deck can significantly impact the structural performance of the girder including the load and deformation capacities as well as the failure mode. Therefore, separate tests of the FRP concrete beams and slabs may not be sufficient to study the structural behavior and to provide design guidelines for engineers.

This thesis presents the experimental and analytical investigations on structural performance of a full-scale AASHTO I-girder Type I, reinforced and prestressed with aramid fiber reinforced polymer (AFRP) bars, where the bridge girder is composite with the deck. The major objectives of this research were to develop a reliable prestressing anchorage system, examine the constructability of the full-scale specimen, study the load and deformation capacities, determine whether or not the design criteria per AASHTO LRFD were met, and improve the performance of the specimen by adjusting the prestressing layout.

The specimen was constructed at a prestressing plant in San Marcos, Texas and tested at the High Bay Structural and Material Testing Laboratory on the campus of Texas A&M

University. The cross-section of the bridge girder was composed of self-consolidating concrete with a total of 24 prestressed and 8 non-prestressed AFRP bars. The bridge deck consisted of a 203 mm (8 in.) conventional steel reinforced concrete slab. A flexure test was conducted to determine the moment-curvature relationship, flexure load capacity, and failure mode. The test was conducted as a simply supported, four point bending test in order to create a region of constant moment at the center of the beam. Two shear tests were conducted to determine the shear capacity, failure mode, maximum strain in the web, and moment-curvature relationship. The shear tests were conducted as a simply supported, three point bending test with varying load placement. The results of these tests were compared to a similar study which investigated the structural performance of a conventional steel reinforced AASHTO I-girder Type I with topping deck (Trejo et al. 2008).

The specimen was also analyzed analytically to determine the effect on performance of varying the prestressing ratio of the separate layers in the bottom flange of the girder. The goal of this analysis was to determine an optimal prestressing layout to improve the performance at the ultimate state, while still satisfying serviceability limits. The prestressing ratio of the layers were varied from 0 to 50 percent in 5 percent increments to study the moment and curvature at both the cracking and ultimate states, along with the available compressive stress due to prestressing at the bottom of the girder.

The results of this research confirms that the experimental specimen showed adequate strength and deformation capacities, satisfying the AASHTO LRFD design criteria. Additionally, the experimental specimen showed significantly greater cracking when compared to the conventional steel reinforced specimen, which is an early warning of impending failure. It was also determined that reducing the prestressing ratio of the AFRP bars in the lower layers improves the ductility of the specimen. The moment capacity can also be improved depending on the prestressing layout. However, reducing the prestressing ratio of the bottom layers causes the cracking moment and available compressive stress at the bottom of the girder to diminish. In order to compensate for this loss, the non-prestressed bars in the web can be prestressed. The optimal prestressing layout features the bottom three layers of the specimen prestressed to 35, 40, and 45 percent of their ultimate capacity, and two of the three layers of middle bars prestressed to 50 percent of their ultimate capacity.

DEDICATION

I would like to dedicate my thesis work to my loving grandmother Marietta Cummings. You are truly loved and missed.

ACKNOWLEDGMENTS

I would like to thank my committee chair, Dr. Stefan Hurlebaus for his guidance and support throughout my undergraduate and graduate research. I would also like to thank my committee members, Dr. John B. Mander, and Dr. Anastasia H. Muliana for their support in this research.

Thank you also to Joshua B. White, Kyle T. Wieghaus, J. Michelle Prouty, and Madhu M, Karthik for their support in the construction and testing of the full-scale bridge girder. I would also like to extend my gratitude to S. Pirayeh Gar for his contributions in analyzing the experimental results. I would also like to recognize that support for the research was provided by a grant from the U.S. Department of Transportation which is funded, in part, with general revenue funds from the State of Texas.

Finally, I would like to thank my family and friends for all of their love and support.

TABLE OF CONTENTS

Page

LIST OF FIGURES

Page

LIST OF TABLES

Page

1 INTRODUCTION

1.1 Research Motivation

Deterioration of the nation's infrastructure is rapidly becoming a nationwide problem. One of the most immediate concerns is the corrosion of the reinforcing and prestressed steel in bridge decks and girders. The age of the structure and the aggressiveness of the environment plays a significant role in the rate of deterioration of the structure. This is a major concern, especially in regions where deicing salts are frequently used, due to the fact that the United States' economy and security is closely tied to its transportation system.

Steel corrosion can compromise structural integrity and lead to possible sudden collapse. This issue has proved to be a significant challenge in the engineering community. Over the past decade, billions of dollars have been spent to maintain and rehabilitate concrete bridges subject to corrosion. In fact, according to NACE International (2013) the annual cost of corrosion in highway bridges is estimated to be $13.6 billion. In order to reduce the annual maintenance cost and extend the service life and overall condition of the nation's highway bridges, an alternative solution is needed to reduce the effect of corrosion in concrete structures.

One solution to overcome corrosion, is to replace the reinforcing and prestressing steel with corrosion resistant materials. Recent advancements in the field of material science have produced products such as fiber reinforced polymer (FRP) bars that are non-metallic and inherently corrosion resistant. These bars are typically reinforced with glass (GFRP), carbon (CFRP), or aramid (AFRP) fibers. These bars have very high strength-to-weight ratios which make them an attractive replacement for steel reinforcement in concrete structures. FRP bars can be manufactured for a variety of applications including, bars for reinforced and prestressed concrete applications, and sheets for external strengthening of deteriorating structures.

Previously, much of the research regarding the performance of concrete structures reinforced and prestressed with FRP has focused on beams and slabs. However, for the application of highway bridge girders, the topping deck considerably effects the performance of the girder. The most significant effect that the topping deck will have on the performance of the girder is the failure mode, as it is dependent on the reinforcement ratio of the specimen.

Another significant effect is the short term deformations as the topping deck adds a significant amount of area to the specimen. Also constructing a full-scale specimen with real dimensions, prestressed with FRP bars, will provide more insight into the possible constructability and practicality issues associated with full-scale implementation of FRP in concrete structures.

The analytical performance of concrete structures reinforced and prestressed with FRP has also mainly focused on beams and slabs. Given that the topping deck will greatly affect the performance of the full-scale specimen, the topping deck should be properly accounted for in the analysis. Also for vertically distributed tendons, varying the prestressing ratio for each layer can significantly change its performance. These knowledge gaps are the main motivation behind the present research.

This research is intended to experimentally and analytically evaluate the structural performance and constructability of a full-scale concrete bridge girder, with composite topping deck, reinforced and prestressed with AFRP bars through flexure and shear tests. An analytical study will also be performed to determine the optimal prestressing layout of the bars that will improve the performance of the specimen at the ultimate state, while still satisfying serviceability limits.

1.2 Research Need

As discussed, much of the research involving FRP reinforced and prestressed concrete has focused on beams and slabs, with little investigation into full-scale specimens with real dimensions. One of the main elements that must be properly modeled is the topping deck as it provides composite action with the girder and largely affects the failure mode and deflection profile. Also, in order to reliably recommend FRP prestressed concrete for practical use the behavior of a full-scale specimen must be investigated. Using this research, reliable design guidelines can be established to incorporate FRP reinforcement in practical applications.

The design of FRP reinforced and prestressed concrete is less established than conventional steel. Conventional steel reinforcement is extremely uniform in its manufacturing and has a predictable yielding point and stress-strain behavior. FRP, on the other hand, lacks clear manufacturing standards, and behaves linearly to up to a somewhat unpredictable rupture stress. For this reason it is common to over-reinforce the section so that it fails due to concrete

crushing instead of FRP rupture. However, in a full-scale specimen with a topping deck, it may be difficult to over-reinforce and prestress the section due to congestion of the bars, and their susceptibility to premature failure during prestressing. Therefore, further research is needed to accurately predict the failure mode.

1.3 Research Objectives

This research investigated the performance of a full-scale AASHTO I-girder Type I with a composite topping deck reinforced and prestressed with AFRP bars. The main objectives of this research were to:

- Develop an anchorage system to successfully prestress the congested AFRP bars within the cross-section of the specimen.
- Evaluate the constructability of the full-scale specimen.
- Experimentally and analytically evaluate the load and deformation capacities through flexure and shear tests.
- Evaluate the structural performance per American Association of State Highway and Transportation Officials (AASHTO) load and resistance factor design (LRFD) criteria.
- Analytically determine the optimal prestressing layout of the AFRP bars within the cross-section of the girder.

1.4 Research Approach

A full-scale AASHTO I-girder Type I with composite topping deck was reinforced and prestressed with AFRP bars, and the structural performance was evaluated both experimentally and analytically. In the first stage of this project, the mechanical properties of the materials used were established, and the design of the girder was finalized corresponding the specimen designed by Pirayeh Gar et al (2014). Once the design of the girder was finalized, the construction process was established. The major concern when constructing the girder was successfully prestressing the AFRP bars. AFRP bars are much weaker in the transverse direction when compared to conventional steel prestressing stands. A conventional steel wedge anchorage would crush the AFRP bar causing premature failure inside the anchorage.

Therefore a reliable anchorage system must be developed in the laboratory to successfully prestress the AFRP bars without causing premature failure in the field.

The AASHTO I-girder Type I along with composite topping deck was constructed at a prestressing plant in San Marcos, TX and then transported to the High Bay Structural and Materials Testing Laboratory at Texas A&M University for testing. A flexure test was conducted first on the full-scale specimen, then shear tests were conducted on the two uncracked ends of the girder.

The experimental results were evaluated to determine if the AASHTO LRFD design criteria were met. The results were also compared with a companion specimen with identical dimension prestressed with conventional steel strands (Trejo et al. 2008). Finally, the girder was examined analytically to determine the optimal prestressing layout of the AFRP bars within the cross-section of the girder.

1.5 Research Background

As discussed much of the research involving FRP reinforced and prestressed concrete has focused on beams and slabs. One of the earliest studies was carried out by Naaman (1993). Two T-beams were partially prestressed using CFRP bars. During the prestressing operation a CFRP bar failed prematurely, suggesting that a reliable anchorage system should be developed first before construction. The authors also found that sections prestressed and reinforced with CFRP tendons have a much lower cracking moment when compared to a similar section prestressed with conventional steel tendons. It was also determined that the conventional equations of force equilibrium and strain compatibility, used to design conventional steel prestressed sections, also apply to FRP prestressed specimens.

Abdelrahman et al. (1995) examined the moment-curvature behavior of concrete T-beams prestressed with carbon fiber composite cables (CFCC). The authors concluded that FRP cables showed a bilinear elastic behavior up to failure. It was also determined that sections with large compression zones fail due to rupture of the FRP bars as opposed to concrete crushing. A method to reliably measure the ductility of beams prestressed with FRP was also proposed.

AFRP ARAPREE® bars were used in this project. Shahawy and Beitelman (1995) examined the flexural behavior of a double-tee beam prestressed with multiple layers of AFRP ARAPREE® bars, and demonstrated that they can be successfully introduced as prestressing strands. Large post-cracking deflections were observed demonstrating that there exists significant warning of failure when using FRP reinforcement. This result was confirmed by Abdelrahman (1997) who also determined that partially prestressing improves the ductility of beams, when compared to fully prestressed members.

Lu (1998) investigated and compared the performance of beams prestressed with AFRP bars to beams prestressed with CFRP bars. The moment-curvature and load-deflection of the specimens were evaluated. It was concluded that beams prestressed with AFRP bars showed much larger curvature capacities while beams prestressed with CFRP bars had improved moment capacities.

Dolan et al. (2001) developed a new method of determining the flexural capacity of vertically distributed FRP bars. The difference between the newly developed method and the simplified equations assuming one layer of prestressed bars was within 1 percent. Nanni et al. (2000) investigated the performance of concrete beams prestressed with CFRP tendons both experimentally and analytically. The beams had 152.4 mm (6 in.) width and height varying between 228.6 and 304.8 mm (9 and 12 in.) with varying partially and fully prestressed layouts. The results showed that the behavior of prestressed concrete beams can be significantly affected by the prestressing layout of the specimen.

The research clearly shows that the structural behavior of a full-scale FRP concrete bridge girder in composite action with the topping deck where the realistic dimensions, boundary conditions, and structural details are all physically modeled, has not been well studied. Conducting a full-scale test with realistic details, where the effect of the bridge deck has been accounted, is crucial because it significantly impacts the structural capacity and failure mode of the bridge girder. Moreover, only under such circumstances are the experimental and analytical results reliable. Design guidelines can be established based on these results, and the overall system can be recommended for practical use.

1.6 Thesis Organization

This thesis includes eight main chapters. The introduction to this research investigation is given in Chapter 1. Chapter 2 presents the experimental program including structural details, and testing plan. Chapter 3 illustrates the newly developed anchorage system for prestressing operations and portrays the state of the art and state of the practice on this topic. Chapter 4 presents the construction process along with discussion of advantages and difficulties using AFRP bars. Chapter 5 presents the experimental results, verifications with numerical analyses, and comparison with the control specimen. Chapter 6 discusses the analytical program including design equations used to create and validate the analytical program. Chapter 7 presents the analytical results including the optimal prestressing layout of the AFRP bars in the girder's cross-section. Chapter 8 summarizes the conclusions and recommendations.

2 EXPERIMENTAL PROGRAM

2.1 Introduction

The experimental program of this research was basically divided into two different tests, flexure and shear. The first test plan was the flexure test, where a large region at the middle of the girder was cracked and damaged to some extent after the test. The second test plan was the shear tests, which was conducted on the two uncracked ends of the girder close to the supports. These flexure and shear tests were both conducted at the High Bay Structural and Materials Testing Laboratory on the campus of Texas A&M University.

A flexure test was conducted to determine the load and curvature capacities of the specimen. The flexure test was set up as a four-point bending test in order to create a region of constant maximum moment in the center of the specimen. The main factors that were studied in the flexure test included flexure load, curvature capacities, failure mode, cracking pattern, strain distribution over the height of the section, deflection profile, and moment-curvature relationship. The flexure load was determined by monitoring the pressure from the 2700-kN (600-kips) actuator used to load the specimen. Concrete strain gages were attached to the top of the deck to determine the failure mode of the specimen. Conventional steel reinforced concrete sections typically fail when the top fiber reaches a strain of 0.003; however, an AFRP reinforced section typically fails due to rupture of the AFRP bars in the bottom flange. LVDTs were attached to the top and bottom flanges of the specimen to investigate the strain distribution over the height of the section, along with the crack widths. String potentiometers were attached to the bottom of the specimen to monitor the deflection profile, curvature capacity, and moment-curvature relationship. A data acquisition (DAQ) system collected data every 5 seconds to determine the following characteristics:

- Moment-curvature relationship (load-displacement relationship).
- Initial stiffness.
- Bond performance prior to cracking.
- Bond performance after cracking.
- Crack patterns.

After the flexure test was completed, both ends of the specimen were tested in shear to determine the shear capacity, failure mode, and maximum strain in the web of the specimen. The specimen was moved via a 178-kN (40-kips) overhead crane in the High Bay Structural and Materials Testing Laboratory, and the supports were adjusted to create the proper clear span. The non-testing end was raised using the overhead crane to ensure that it did not affect the results. A load cell was attached to the overhead crane, and the load was held constant to ensure consistent testing. The placement of the load point varied to determine the transition point from flexure to shear failure along the length of the specimen. The main factors that were studied in the shear test included shear capacity, failure mode, and maximum strain in the web. Concrete strain gages were attached to the top of the deck to determine the failure mode of the specimen. The shear capacity was investigated by monitoring the load applied to the specimen via the pressure from the 2700-kN (600-kips) actuator. LVDTs were attached in a crossing pattern in the center of the web to determine the maximum strain in the web. The cracking patterns and crack widths were also monitored. A DAQ system collected data every 5 seconds to determine the following characteristics:

- Moment-curvature relationship.
- Bond characteristics of the development length region.
- Shear performance.
- Crack patterns.

2.2 The Experimental Specimen

The cross-section of the AASHTO I-girder Type I was composed of self-consolidating concrete reinforced and prestressed with AFRP bars having a 10-mm (0.393-in.) diameter. The dimensions and reinforcement layout are shown in Figure 2-1. Twenty-four prestressed AFRP bars were used within the girder section: 22 in the bottom flange and two in the top flange. In addition, eight non-prestressed AFRP bars were used within the girder section: six in the web and two in the top flange. The shear reinforcement dimensions and layout for the R-shape, top, and bottom stirrups are presented in Figure 2-1 and Figure 2-2. R-shape stirrups were spaced 203 mm (8 in.) apart along the length of the girder except at the support region, where the stirrup spacing was reduced to 102 mm (4 in.) to better resist the diagonal shear. The top and

bottom stirrups were placed only at the support region and spaced 102 mm (4 in.) apart. In addition to AFRP shear reinforcement, steel bolts were added at the girder-to-deck interface for a better transfer of horizontal shear through the girder-to-deck composite action. The shear bolts were spaced 457 mm (18 in.) apart along the girder.

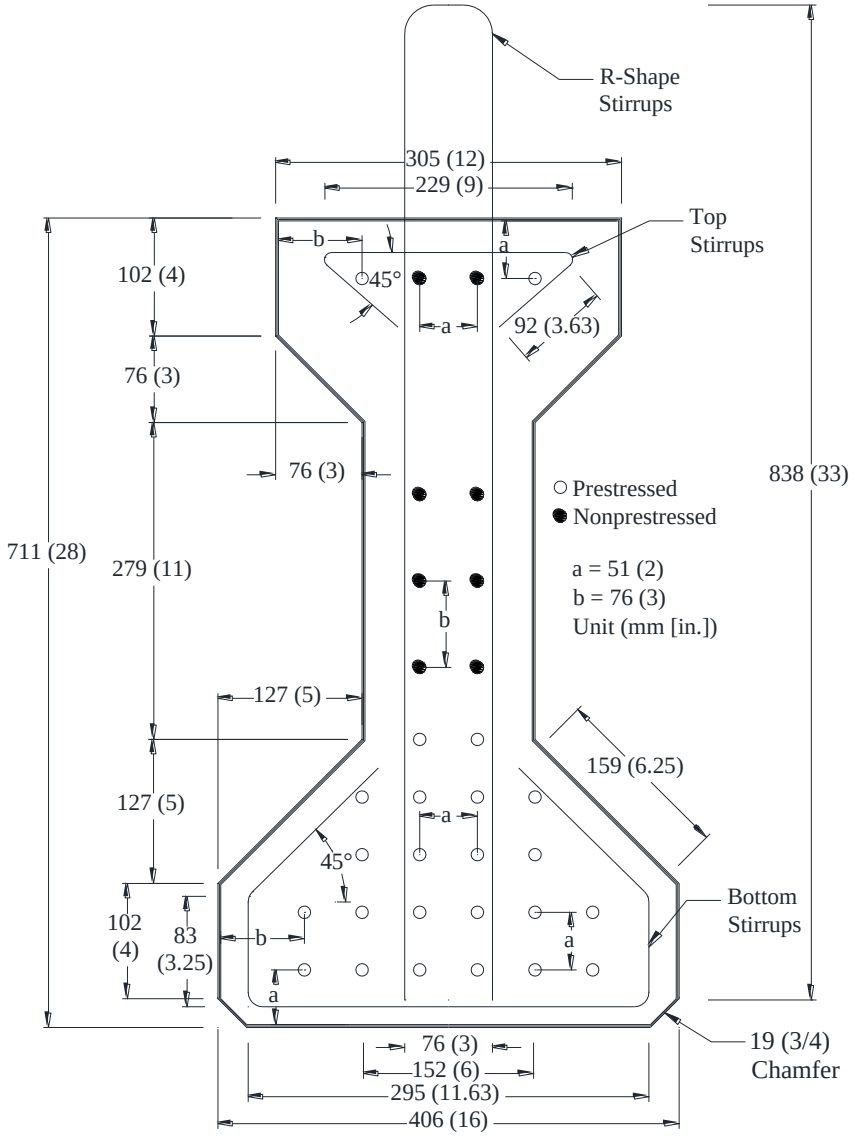

Figure 2-1. AASHTO I-Girder Type I with Composite Topping Deck Dimensions and Reinforcement.

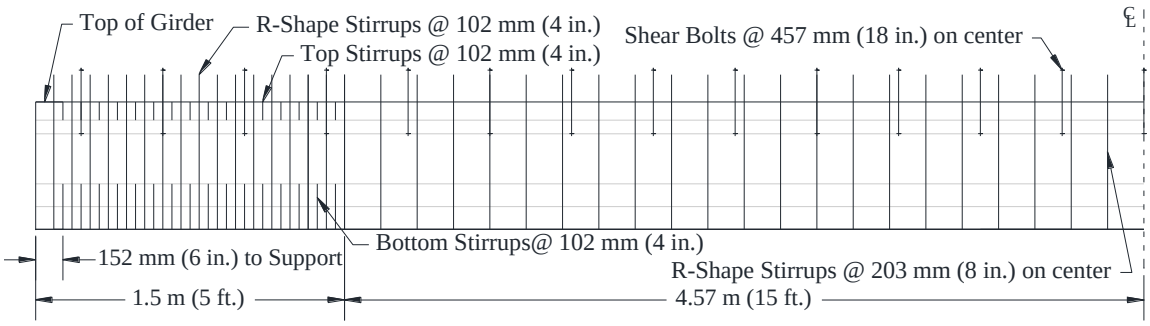

Figure 2-2. Shear Reinforcement Layout of the Girder.

The reinforcement for the topping deck consisted of conventional steel rebar to reinforce the slab either longitudinally or transversely. AFRP reinforcement was not used in the topping deck because the deck was modeled only to provide composite action with the girder. The reinforcement layout for the topping deck is shown in Figure 2-3. The longitudinal reinforcement was composed of two D16 (#5) rebar bisecting the center, six D13 (#4) rebar spaced at 203 mm (8 in.) apart on the bottom, and nine D13 (#4) rebar spaced at 178 mm (7 in.) at the center on the top. The transverse reinforcement was composed of D13 (#4) rebar placed 203 mm (8 in.) apart on the top and bottom.

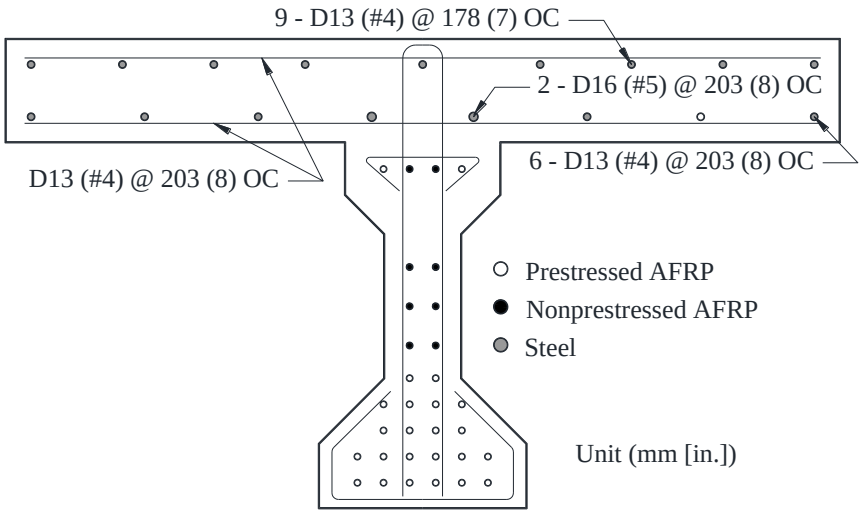

Figure 2-3. Deck Reinforcement Detail.

2.3 Flexure Test Setup

The flexure test setup is shown in Figure 2-4 to Figure 2-6. Steel frames were anchored to the strong floor at the High Bay Structural and Materials Testing Laboratory using post-tensioned DYWIDAG threaded rods. A 2700-kN (600-kips) actuator was attached to the steel frame and used to load the specimen. A steel W-shape was positioned under the load point and supported by two 914×203-mm (36×8-in.) rocker supports placed 915 mm (36 in.) apart to distribute the load evenly throughout the composite topping deck. Rocker supports with 203×203×76-mm (8×8×3-in.) Neoprene bearing pads supported the girder. The bearing pads were positioned to create an 11.8-m (39-ft.) clear span. The specimen was manually loaded under displacement control at a rate approximately equal to 44 kN (10 kips) per minute before first cracking at the midspan, and then the rate was decreased to 22 kN (5 kips) per minute after cracking. The load was halted periodically to record and mark crack locations and widths.

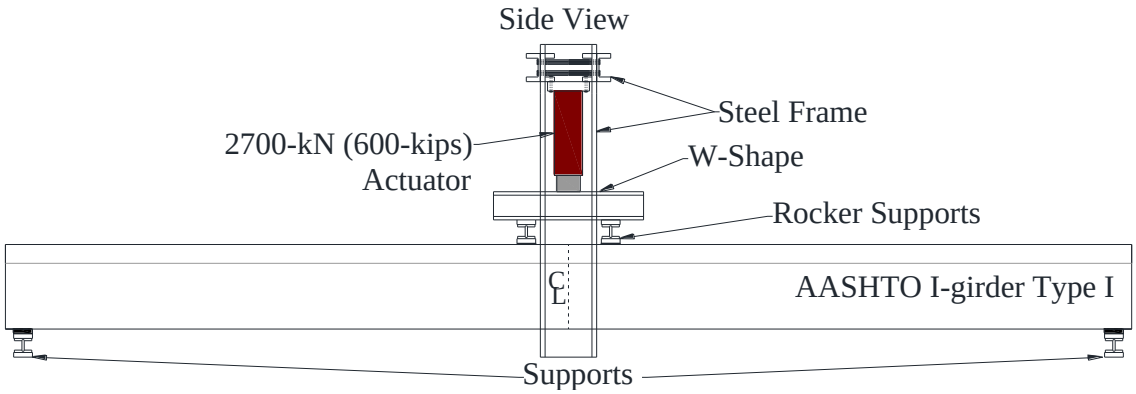

Figure 2-4. Side View of Flexure Test Setup.

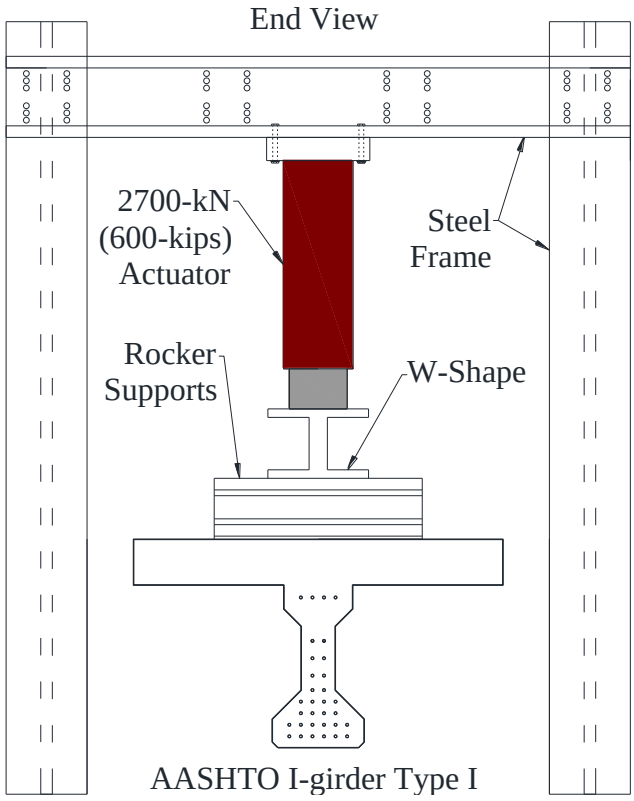

Figure 2-5. End View of Flexure Test Setup.

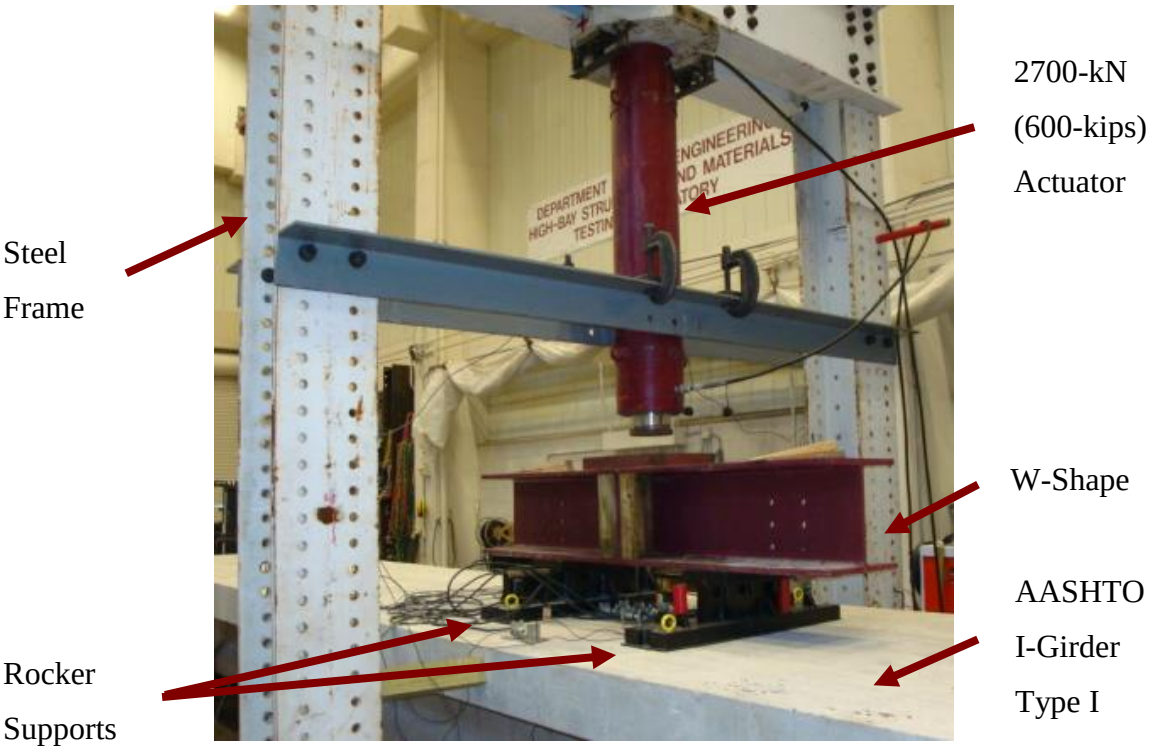

Figure 2-6. Flexure Test Setup.

2.4 Instrumentation for Flexure Test

Concrete strain gages and LVDTs were placed on the top of the deck to measure the strain at the top fiber of the concrete. The top of the deck was sanded with a concrete grinder to create a smooth surface for the gages to adhere to. The gages were attached to the deck using a quick-setting epoxy resin. The locations of the concrete strain gages are shown in Figure 2-7.

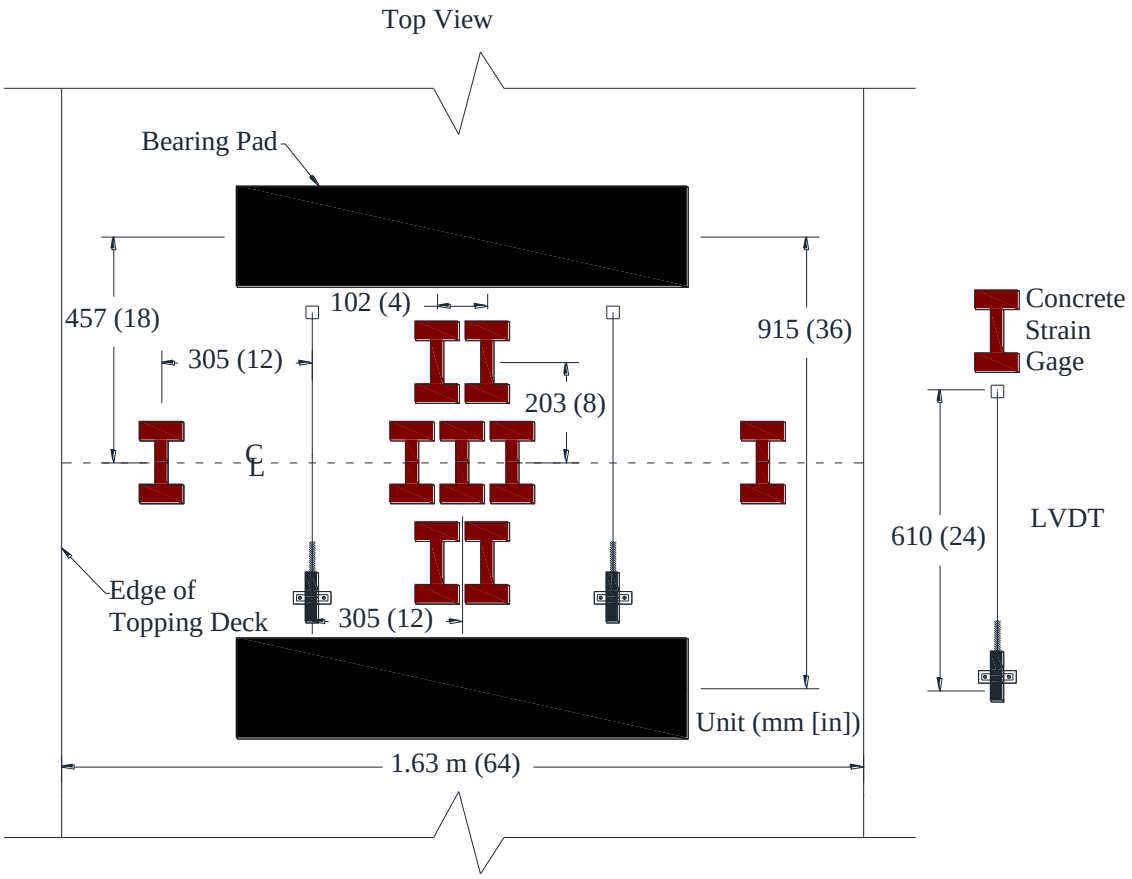

Figure 2-7. Strain Gage and LVDT Layout on Topping Deck at Middle of the Girder (Flexure Test).

Eight LVDTs were attached to measure the strain distribution over the height of the section: five to the bottom flange and three to the top flange of the girder. The LVDTs were attached by securing the body to a piece of wood epoxied to the girder. Small-diameter threaded rods were attached to the carrier in order to extend the gage length to 610 mm (24 in.) for a better capture of the strains and crack widths. The layout of the LVDTs is presented in Figure 2-8.

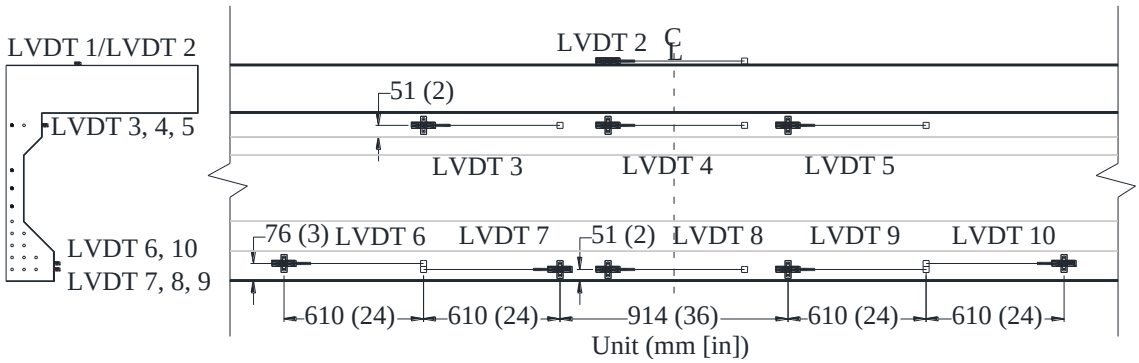

Figure 2-8. LVDT Layout (Flexure Test).

Thirty-one string potentiometers were attached to the bottom of the girder to measure the deflection along the girder. The string potentiometers were secured to a piece of wood that was epoxied to a steel plate in order to overcome the retracting force. A piece of wood with a small metal hook was attached to the bottom of the girder and connected to the measuring cable of the string potentiometer via fishing line. The locations of the string potentiometers are presented in Figure 2-9. The test was terminated when the AFRP in the bottom flange ruptured.

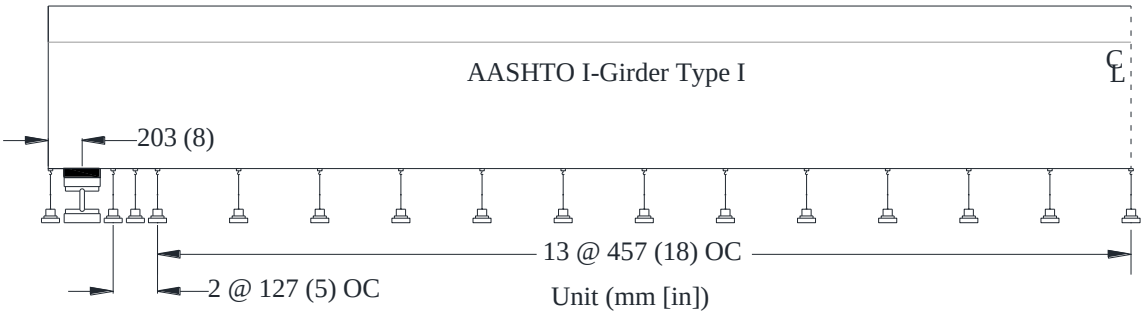

Figure 2-9. String Potentiometer Layout (Flexure Test).

2.5 Shear Test Setup

Following the flexure test, both ends of the girder were tested to determine the shear capacity of the girder. The steel frame and actuator remained stationary while the girder and supports were repositioned for the shear tests. The shear test setup is shown in Figure 2-10, to Figure 2-12. The non-testing end was raised using the overhead crane to ensure that it did not affect the results. A load cell was attached to the overhead crane, and the load was held constant to ensure consistent testing. A 914×203-mm (36×8-in.) rocker support was placed under the actuator to distribute the load evenly throughout the topping deck. Rocker supports with 203×203×76-mm (8×8×3-in.) Neoprene bearing pads were positioned 3.7 m (12 ft.) apart to support the girder. The specimen was manually loaded under displacement control at a rate approximately equal to 22 kN (5 kips) per minute. The load was halted periodically to record and mark crack locations and widths. The test was terminated when the AFRP in the bottom flange ruptured.

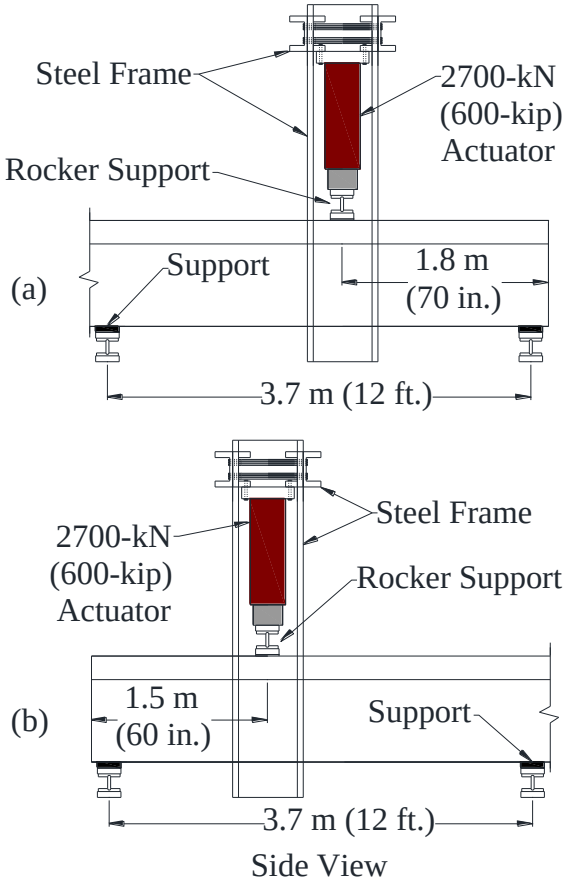

Figure 2-10. Side View of Shear Test Setup: (a) Shear Test 1 and (b) Shear Test 2.

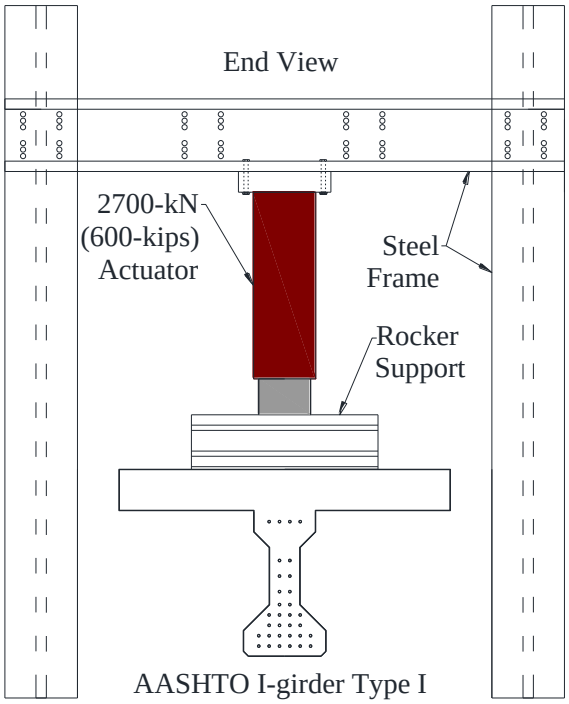

Figure 2-11. End View of Shear Test Setup.

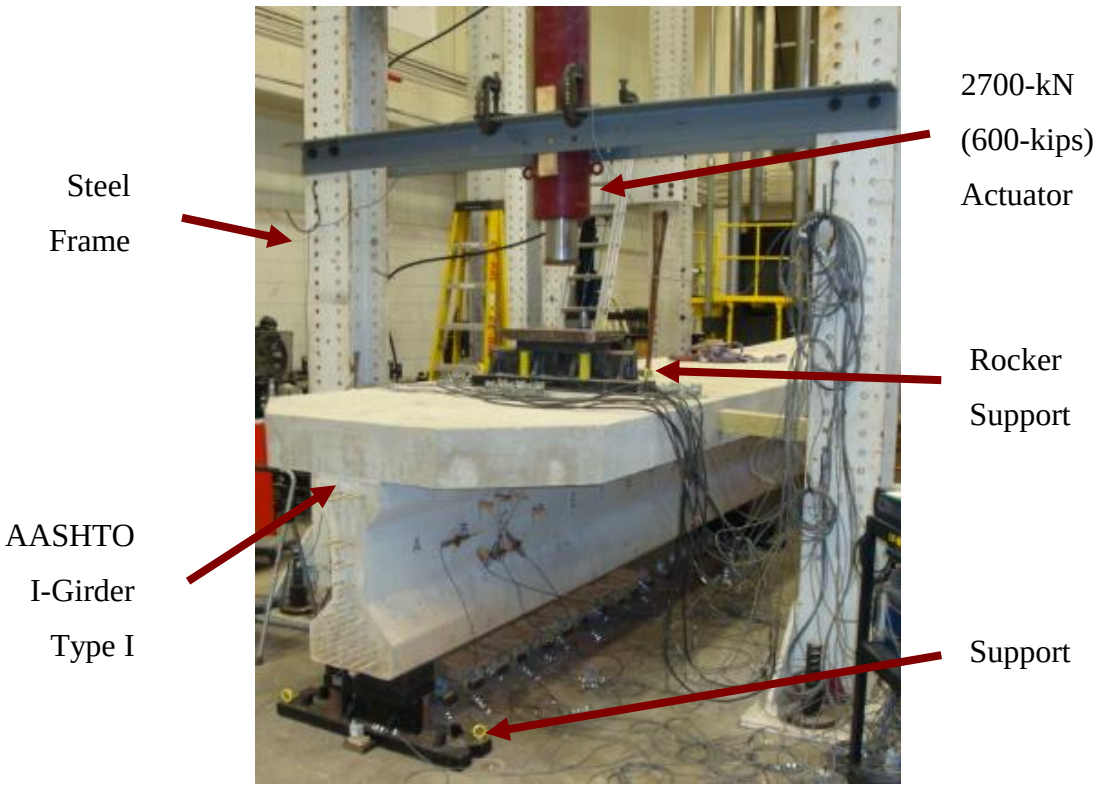

Figure 2-12. Shear Test Setup.

The embedment length and test span varied between the tests to determine the transition point from flexure to shear failure. In order for the specimen to fail in shear, the embedment length must be shorter than the required development length. The embedment length is defined as the length of the embedded AFRP bars from the end of the girder to the loading point. The embedment lengths for shear test 1 and shear test 2 were 1.8 m (70 in.) and 1.5 m (60 in.), respectively.

2.6 Instrumentation for Shear Tests

Concrete strain gages were attached to the top of the deck to measure the strain in the top fiber of the concrete. The gages were attached in the same manner as described earlier, and the layout is shown in Figure 2-13. The concrete gage layout for the second shear test was identical to the first.

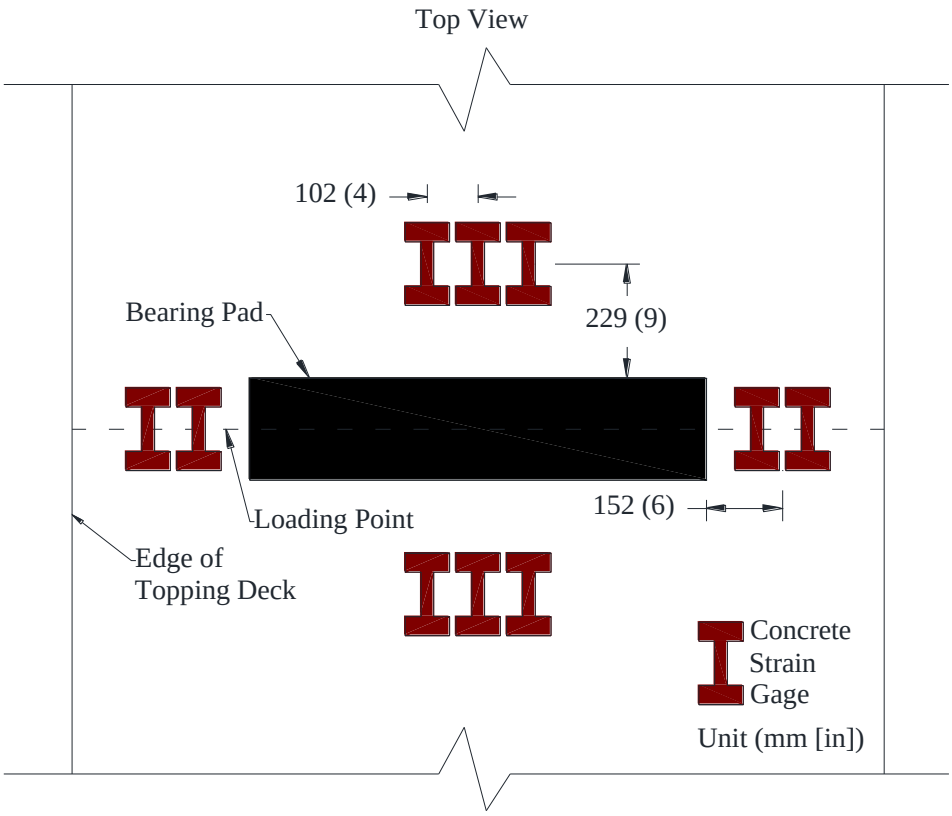

Figure 2-13. Concrete Gage Layout (Shear Test).

Four LVDTs were attached to the web on each side of the girder to measure diagonal tensile and shear strains. The LVDTs were attached using the same procedure as discussed previously. The LVDT layout for the shear tests is shown in Figure 2-14. In order to install the LVDTs in the locations presented in Figure 2-14, the bodies of the LVDTs were attached to the girder using pieces of wood of varying thicknesses.

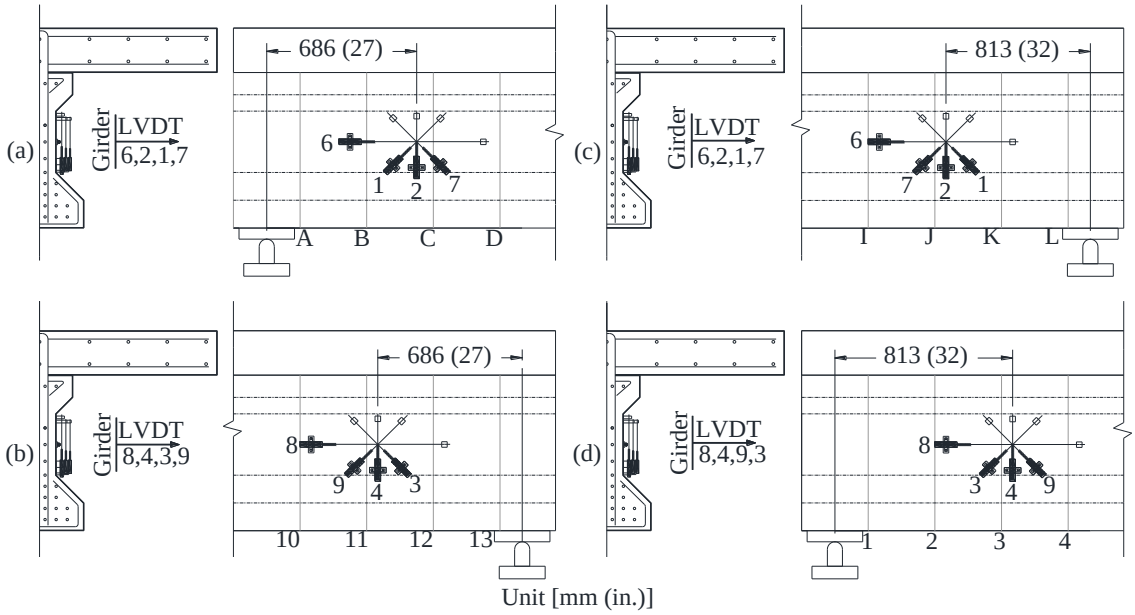

Figure 2-14. LVDT Layout: (a and b) Shear Test 1 and (c and d) Shear Test 2.

String potentiometers were attached to the bottom of the girder, using the same procedure as discussed previously, to measure the deflection of the girder. One string potentiometers was placed directly under the load point, and the remaining potentiometers were spaced 203 mm (8 in.) apart. Additional string potentiometers were placed on either side of the Neoprene bearing pads at the supports. The string potentiometer layout for the shear tests are shown in Figure 2-15.

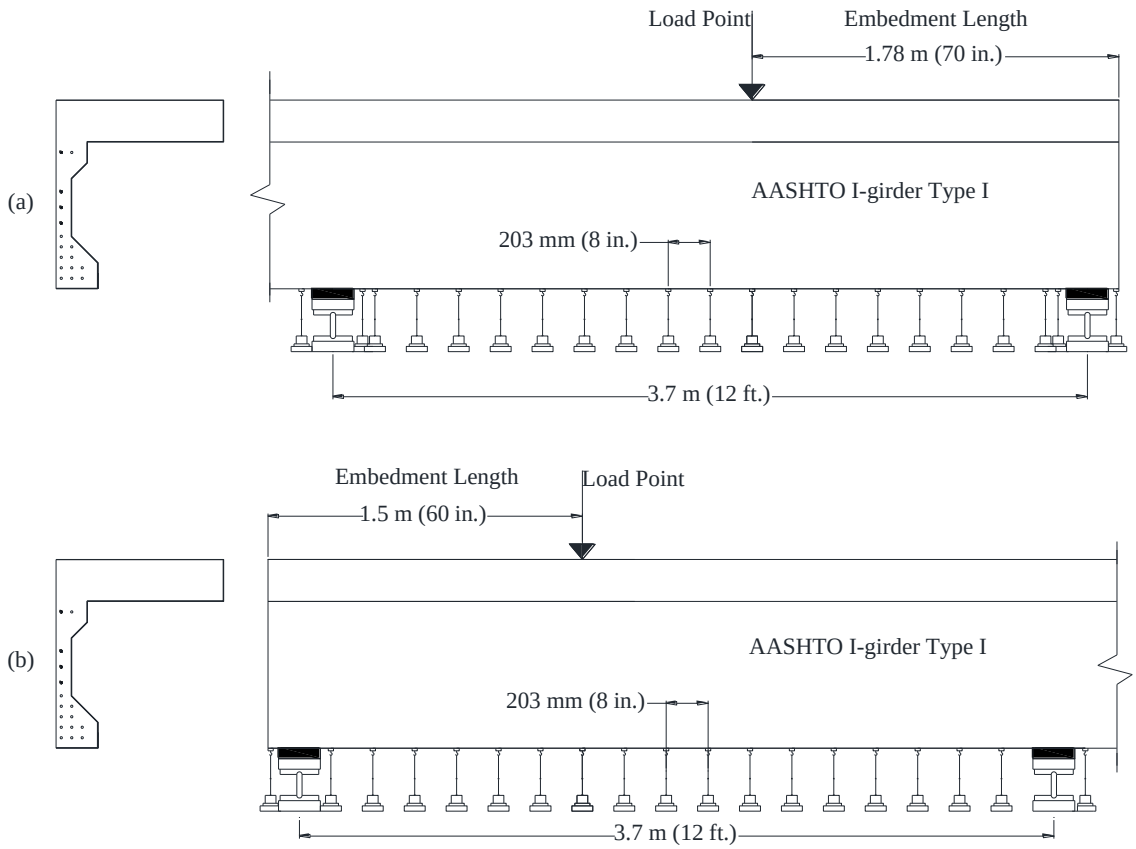

Figure 2-15. String Potentiometer Layout: (a) Shear Test 1 and (b) Shear Test

3 PRESTRESSING ANCHORAGE SYSTEM

3.1 Introduction

Due to the weak strength of FRP bars in the transverse direction, the prestressing level (prestressing force over strength) is a critical design parameter that needs to be carefully selected to avoid either short-term or long-term failure. For instance, ACI 440.4R (2004) limits the prestressing level to 0.5 and 0.65 for AFRP and CFRP bars, respectively. This limitation depends upon the anchorage type and creep-rupture characteristics of FRP bars. It has also been stipulated that the prestressing level should not exceed 65 percent of the anchorage capacity (ACI 440.4R 2004), and also the tertiary stage of creep rupture should never be reached. Thus, GFRP bars are not recommended for prestressing application since they have poor resistance to creep.

Therefore, a practical anchorage system should have a minimum capacity equal to the prestressing level with a safety factor of 0.65, and transfer the prestressing load to the bar in a uniform manner to avoid stress concentration, which may cause fatigue and creep issues. Furthermore, the anchorage system should sustain the load without any considerable loss in prestressing force. Thus, a practical and reliable anchorage system is a design concern because FRP bars are weak in the transverse direction, and the fibers can be damaged under the gripping force of the anchorage.

For prestressing application there are basically two common types of anchorage systems, wedge anchorages and potted anchorages. Wedge anchorages are composed of a number of wedges, a conical barrel, and an optional sleeve. Wedge anchorages are mostly preferred over potted anchorages because of the wedge anchorages' reusability, ease of assembly, compactness, and familiarity. Figure 3-1 shows a wedge anchorage system schematically. As the bar is forced into the conical barrel, the wedges apply a compressive force along the bar. These compressive forces grip the bar and allow the bar to be pre-tensioned. A sleeve can also be used to uniformly distribute the compressive forces and protect the bar from premature failure due to compressive stress concentrations.

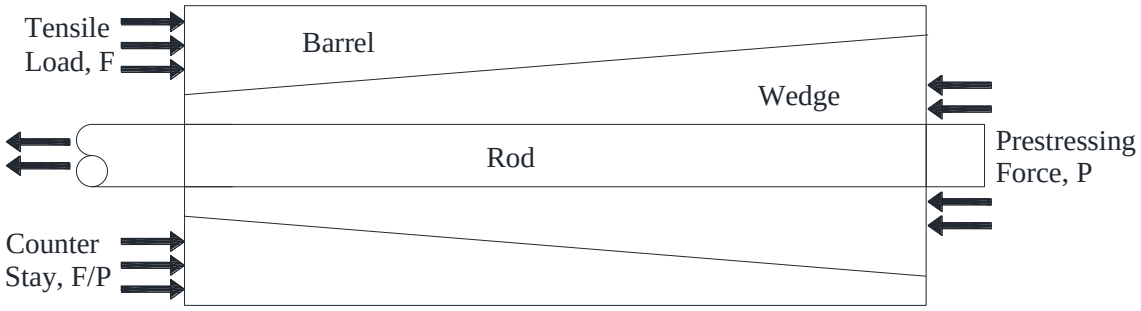

Figure 3-1. Schematic of Conventional Wedge Anchor System (Bennitz and Schmidt 2012).

3.2 State of the Art

3.2.1 Wedge Anchorage Systems

Considerable experimental investigations have been conducted on wedge anchorage systems for use in FRP prestressed concrete. Conventional wedge anchorages consist of a multi-wedge and barrel system, where the wedges apply a transverse gripping force to the exterior surface of the prestressing strand. Because FRP bars are not strong in the transverse direction, the wedge tends to crush the fibers with a large stress concentration, followed by a premature failure (Al-Mayah et al. 2001b, Bennitz and Schmidt 2012). Therefore, to overcome this problem, the conventional wedge anchorage needs to be properly modified to avoid direct contact between the wedge and FRP bar, and also to transfer the gripping force in a more distributed manner. Using a sleeve between the wedge and FRP bar is one solution that researchers have recently introduced and investigated (ACI 440.4R 2004).

Shrive (2000) introduced a stainless steel anchorage system, similar to that shown in Figure 3-2, for CFRP bars and investigated the effect of the wedge, sleeve, and barrel material. The preliminary tests on the wedge anchorage without a sleeve showed high stress concentrations and resulted in premature failure due to crushing of the fibers. In the next step, a sleeve was used to alleviate the stress concentration and to avoid premature failure. A sandblasted copper sleeve of 0.48-mm (0.019-in.) thickness was tested against an aluminum sleeve of 0.64-mm (0.025-in.) thickness. The aluminum sleeve performed better than the copper sleeve because

the softer aluminum had the ability to plastically deform and flow into the indentations of the CFRP bar, providing a better grip. The authors recommend the use of steel wedges because they performed better than either aluminum or copper wedges in preliminary tests.

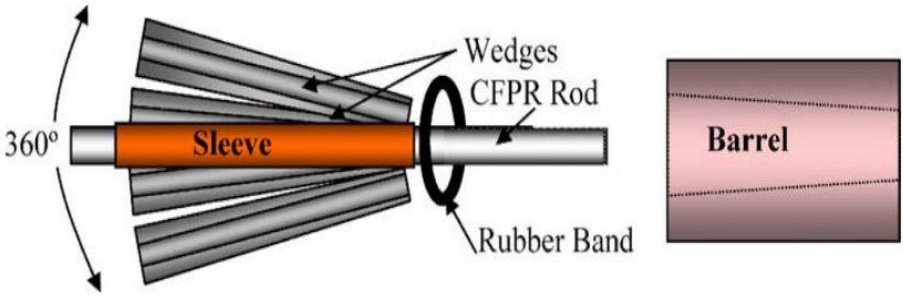

Figure 3-2. Schematic of a Wedge Anchorage System (Al-Mayah et al. 2006).

Al-Mayah et al. (2001a) investigated a similar wedge-type anchorage system consisting of a stainless steel barrel, a four-piece stainless steel conical wedge set, and an aluminum sleeve. Two LVDTs were attached to the CFRP bar to measure the slip of the bar and sleeve relative to the barrel. Prestressing loads equal to 48, 63, 77, and 96 percent of the ultimate strength of the CFRP bar were applied. As shown in Figure 3-3, the test results revealed three distinct regions of slippage. When the load reached the first threshold value (F1), only the bar moved. This behavior continued until the load reached the second threshold value (F2) when the sleeve started to slip. At a load of 100 kN (22.5 kips), the bar moved by an amount Slip1, and the sleeve moved by an amount Slip2. During the third stage, the sleeve and wedges moved together. This slip behavior was similarly observed in all the tests conducted, where the threshold values F1 and F2 varied for each experiment. As the prestressing load increased, the slippage of the bar decreased due to the larger gripping force. Al-Mayah recommended that a prestressing load in the range of 60 to 80 percent of the ultimate strength of the bar be applied using the anchorage system tested.

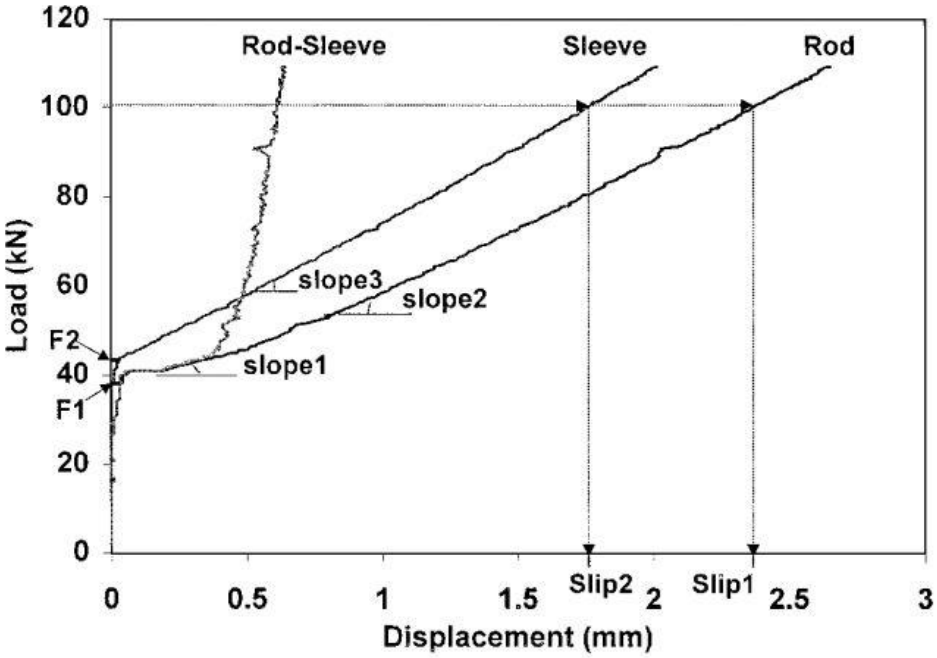

Figure 3-3. Typical Slip Behavior of Wedge Anchorage Components (Al-Mayah et al. 2001b).

Al-Mayah et al. (2001b) also studied the effect of sleeve material on performance of the anchorage for CFRP bars. The researchers designed the sleeve material such that it would be able to plastically deform into the indentations of the CFRP bar, but be strong enough not to fail during the prestressing process. The same prestressing loads of 48, 63, 77, and 96 percent of the ultimate strength of the bar were used. Sleeves with an inner diameter of 7.9 mm (0.31 in.) and outer diameter of 9.18 mm (0.39 in.) made of 6061-T6 aluminum and oxygen-free high thermal conductivity (OFHC) copper were tested. The typical slippage showing three distinct regions was observed. The static tests showed that the copper sleeve performed poorly at low presetting loads but better at high presetting loads, when compared to aluminum sleeves. Due to unreliability, however, further investigation was recommended as to the performance of copper sleeves.

Although the experimental tests showed that using a sleeve could enhance the load capacity of the wedge anchorage, the bond strength between the sleeve and FRP bar could still be

improved to reduce the slippage and the subsequent prestressing loss. For this purpose, the effect of sandblasting the inner surface of the sleeve was investigated by Al-Mayah et al. (2005). The sandblasting technique increases the coefficient of friction between the sleeve and FRP bar, thereby improving the bond strength. A similar load-slippage relationship to that of Figure 3-3 was observed. In fact, this graph represents the stick-slip behavior of the anchorage. When the contact pressure was low, the load rose to threshold level F1, and the bar gradually slipped out of the sleeve. When the contact pressure was high, region2 was significantly reduced, and sticking occurred after a slippage of about 10–25 mm (0.4–1.0 in.). These tests have revealed that complete sticking occurred earlier, and within a shorter sliding distance, when a sandblasted sleeve was used. Also in the case of very high contact pressures, region3 appeared where sticking occurred after a little slip, which is a desired outcome for a CFRP anchorage system. This experiment confirmed that that the friction coefficients and the contact pressure are the two critical design parameters that can improve sleeve-to-bar bond strength. In an ideal design, the contact pressure should be lowest at the loading end and highest at the free end, where little to no tensile stress is applied, as shown in Figure 3-4. This ideal contact pressure distribution prevents stress concentrations from forming at the loading end of the anchorage, which in turn prevents premature failure due to crushing of the bar.

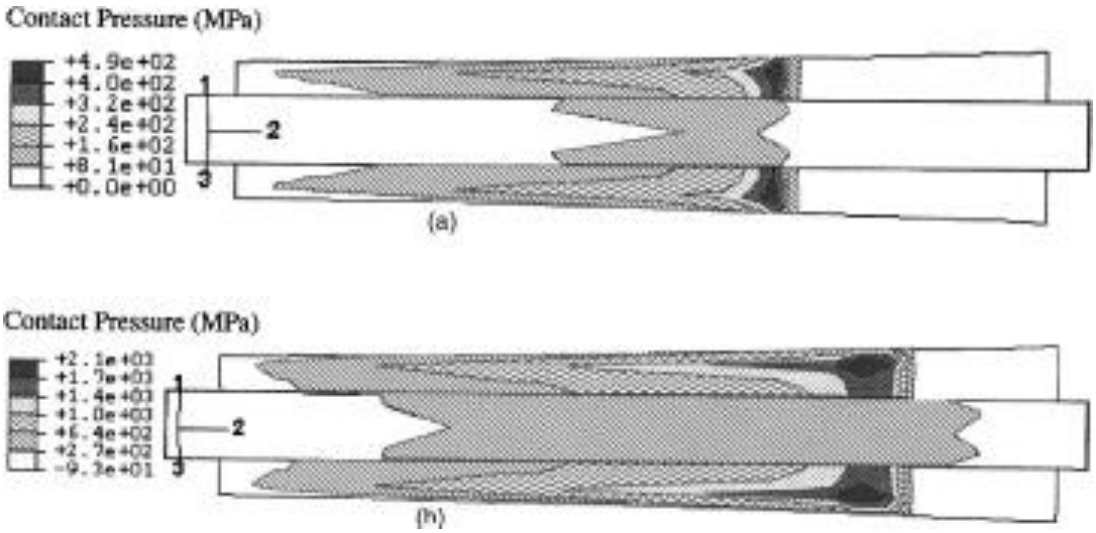

Figure 3-4. Contact Pressure Distribution (Al-Mayah et al. 2007).

To increase the sleeve-to-bar bond strength, there are some other alternatives such as using swaged sleeves, resin-filled sleeves, and epoxy-bonded sleeves. Swaging is the process of gradually reducing the diameter of tubes or rods by radial hammering inside a dye. This is used to permanently attach the sleeve to the bar and provides a clamping pressure to develop shear friction between the sleeve and bar. The clamping pressure, reduction in cross-sectional area, and swaged length are the critical parameters directly affecting the anchorage's performance. Pincheira et al. (2005) investigated the performance of cold-swaged sleeves, resin-filled sleeves, and epoxy-bonded sleeves in tension and under displacement-control loading conditions. All specimens with epoxy-bonded sleeves failed due to bar pullout. Resin-filled sleeves were used on both smooth and deformed CFRP bars. The deformed CFRP bars featured 3.8-mm (0.15-in.) indentations spaced 13 mm (0.5 in.) along the bar, as shown in Figure 3-5. Two specimens had an indentation depth of 0.13 mm (0.005 in.), and one specimen had an indentation depth of 0.25 mm (0.1 in.). All resin-filled sleeves with smooth bars failed due to bar pullout. The resin-filled sleeves with deformed CFRP bars failed due to bar pullout and bar fracture regardless of the indentation size. The swaged sleeve was formed from a low-carbon stainless steel tube with an outer diameter of 9.5 mm (0.375 in.) and wall thickness of 1.2 mm (0.049 in.). The tube was swaged until the outer diameter was reduced to 8.6 mm (0.34 in.). The swaged length varied from 53 mm (2.1 in.) to 94 mm (3.7 in.). Swaged sleeves with a conventional wedge anchorage failed due to either sleeve yielding or bar pullout. Swaged sleeves with a longer barrel and wedges failed due to bar fracture, which was the desired failure mode. Although the combination of swaged sleeves and a longer barrel proved to be successful, the major practical drawback is the implementation process, which is time consuming and requires highly skilled workers. Furthermore, swaged sleeves are not reusable because the swaging process permanently attaches the sleeve to the bar.

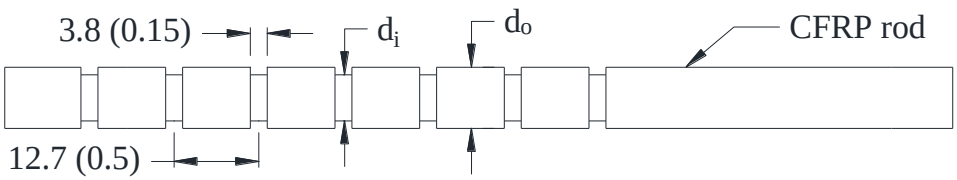

$(d_o + d_i)/2$ = 0.127 (0.005) (specimens RF1-D and RF2-D)
= 0.254 (0.010) (specimen RF3-D

Figure 3-5. CFRP Bar Indentations (Pincheira 2005).

The performance of the conventional anchorage with plastic wedges developed by the manufacturer of AFRP ARAPREE® bars has been recently investigated by Pirayeh Gar (2012). The conventional anchorage was tested using an MTS® testing machine with a monotonically applied load at the rate of 22 kN (5 kips) per minute according to ASTM 638. The applied load was recorded via a load cell connected to the MTS® machine, and the elongation of the specimen was measured through strain gages mounted at the middle of the bar. The anchorage consisted of hard plastic wedges with a steel casing. All specimens failed in a brittle fashion near the anchorage location before reaching the ultimate stress, as shown in Figure 3-6. The failure stress for each specimen is presented in Table 3-1 and compared with the failure stresses observed in the uniaxial tests conducted by Pirayeh Gar et al. (2013). This anchorage was also tested to investigate if the anchorage could sustain a prestressing load for a significant period of time. The anchorage was tested in an MTS® testing machine at a prestressing load equal to 55 percent of the ultimate capacity. After about 20 hours, the bar failed near the anchorage, similar to the failure shown in Figure 3-6. This implies that the anchorage was unable to sustain the prestressing load for a long period of time. For both tests, transverse stresses, caused by the hard plastic wedges, crushed the AFRP bar and caused premature failure since AFRP bars are weak in the transverse direction.

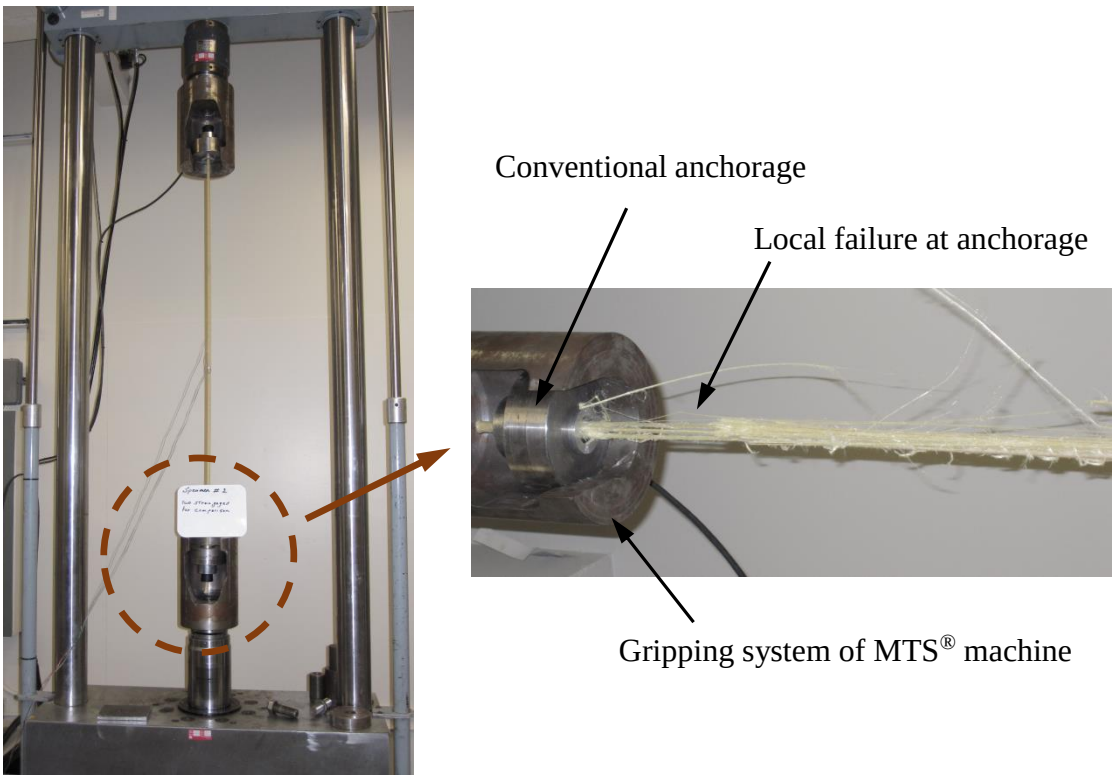

Figure 3-6. Failure of AFRP in Conventional Wedge Anchorage (Pirayeh Gar 2012).

Table 3-1. Comparison of Uniaxial and Conventional Anchorage Test Results (Pirayeh Gar 2012).

Conventional AFRP Anchorage Results		Uniaxial Test Results	
Specimen No.	Failure Stress (MPa [ksi])	Specimen No.	Ultimate Stress (MPa [ksi])
1	1030 (149.4)	1	1549.9 (224.8)
2	1010 (146.5)	2	1448.2 (210.0)
3	1006 (145.9)	3	1431.3 (207.6)
4	1058 (153.4)	4	1358.8 (197.1)
5	1015 (147.2)	5	1464.2 (212.4)
Mean	**1024 (148.5)**	6	1489.1 (216.0)
Standard Deviation (Unbiased Estimator)	**21**	Mean	**1457 (211.3)**
		Standard Deviation (Unbiased Estimator)	**63.4**

As discussed, the prestressing system using wedge-type anchorages benefits from their compactness, ease of assembly, and reusability. However, the main drawback of using wedge anchorages lies in the non-uniform transverse stresses induced by mechanical gripping, which triggers premature failure at the location of stress concentration. Using a sleeve as an intermediate part between the wedge and FRP bar to alleviate the stress concentration and to transfer the load in a more distributed manner could potentially weaken the bond strength. To compensate for the lack of bond strength, some solutions such as increasing the contact pressure, enlarging the contact area, and raising the friction coefficient between anchorages' components have been investigated by researchers, as previously discussed. Although some relative success can be seen in the experimental results, none of these options could be considered a reliable and practical anchorage for universal application. Using a wedge-type anchorage with a sleeve and enhanced bond strength does not offer a simple solution that can be broadly applied in the field for large-scale construction and may not be effective either cost-

wise or time-wise. Furthermore, this type of anchorage might be very sensitive to the material type of the sleeve, bond length and bond strength between the sleeve and FRP bar, contact pressure, and accuracy of assembling. Also, the sustainability of the anchorage needs to be investigated once the load capacity has proved to be sufficient.

3.2.2 Potted Anchorage Systems

A competitor to the wedge-type anchorage with a sleeve and enhanced bond strength, the potted anchorage does not suffer from many of these drawbacks and hence has been widely investigated by researchers. Potted anchorages consist of an FRP bar embedded in a potting material that is confined by the walls of a casing. The potting material can vary from non-shrink cement to expansive grout. Potted anchorages grip the FRP by either bonding and interlocking the anchorage components, or generating circumferential pressure, depending on the potting material used. The effectiveness, therefore, is highly dependent on the geometry and bonded length of the anchorage (Zhang and Benmokrane 2004). Potted anchorages, particularly those using expansive grout, do not crush the FRP bar because the radial pressure is uniformly applied and independent of the prestressing load. Hence, the only major failure mode that needs to be designed against is pullout of the FRP from the potted anchorage.

There are basically two types of potted anchorages, a contoured sleeve and a straight sleeve. Contoured anchorages feature a tapered inner profile, such as conical or segmental, and have the ability to generate high radial pressure as the specimen is loaded (ACI 440R-04). The success of this anchorage is highly dependent on the internal geometry of the anchorage. The most common contoured anchorage uses a conical profile with a linear taper. Contoured sleeve anchorages are costly and difficult to manufacture, so straight sleeve anchorages are more widely accepted. Straight sleeve anchorages are easy to manufacture and have been used successfully in engineering practices (Zhang and Benmokrane 2004). Straight sleeve anchorages are also easier to design because the performance of the anchorage is mostly dependent on the bond length, geometry, and potting material.

There are two common types of potting material, resin and cementitious grout. The load transfer mechanism for resin relies on interlocking of the anchorage components. Resin has a high strength and fast curing time, but it is expensive and has the potential to deteriorate. Therefore, cementitious grout is more commonly used as the potting material in potted

anchorages. The load transfer mechanism for cementitious grout is based on the circumferential pressure generated by the expansive grout, which must fully fill the anchorage. The performance of the grout is largely dependent on the stiffness properties, moisture of curing, and degree of confinement of the grout (Bennitz and Schmidt 2012).

Straight sleeve anchorages were investigated by Zhang and Benmokrane (2004). Three different bond lengths—250 mm (9.8 in.), 300 mm (11.8 in.), and 500 mm (19.7 in.)—were tested on a 7.9-mm (0.311-in.) diameter CFRP Leadline® bar. The steel sleeve had a 35-mm (1.38-in.) outer diameter and 25.4-mm (1-in.) inner diameter with a serrated inner surface to increase the bond strength. A cementitious grout with a 28-day compressive strength of 70 MPa (10.2 ksi) was used in the straight sleeve anchorage. The experimental setup for the pullout tests is shown in Figure 3-7. The anchorage was tested in a universal testing machine with the load applied monotonically at a rate of 22 kN/min. (5 kips/min.). The results show that all specimens tested failed due to bar rupture, regardless of bond length. Therefore, a bond length of 250 mm (9.8 in.) is sufficient to reach the ultimate capacity of the CFRP bar. However, increasing the bond length improves the stiffness of the anchorage.

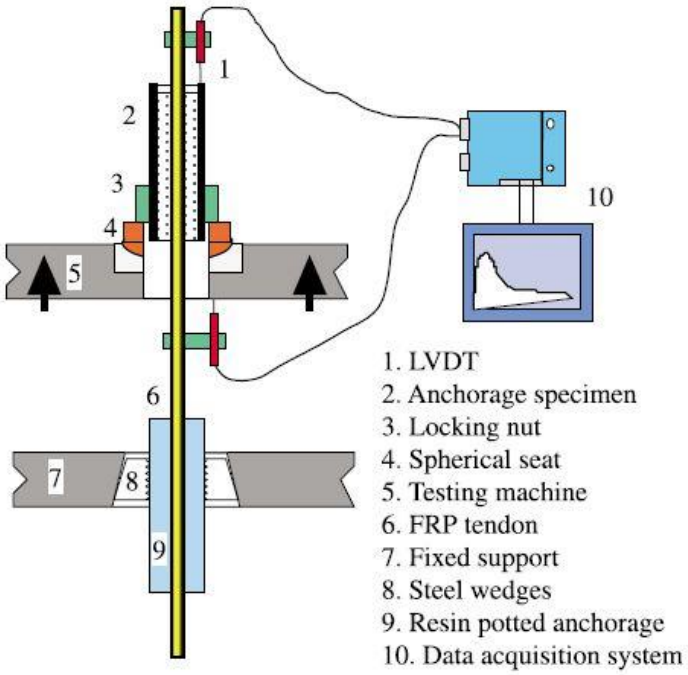

Figure 3-7. Tensile Test Setup (Zhang and Benmokrane 2004).

As previously discussed, Pirayeh Gar (2012) investigated the load capacity of a wedge-type anchorage developed by the manufacturer for AFRP ARAPREE® bars. This anchorage proved to be insufficient because it caused premature failure of the AFRP bars because the hard plastic wedges crushed the bar. The wedge-type anchorage was also unable to sustain the prestressing load for a long period of time. Therefore, Pirayeh Gar (2012) developed a practical and reliable anchorage system for prestressing precast panels of FRP concrete bridge deck slabs. The anchorage system was composed of a steel pipe with a 457-mm (18-in.) length, 48-mm (1.9-in.) outer diameter, and 5-mm (0.2-in.) wall thickness filled with an expansive and quick-setting grout. The AFRP ARAPREE® bar was placed in the center of the pipe and held in place by plastic stoppers with central holes. The grout was poured through the first hole until it flushed the pipe's surface at the second hole to ensure that no air bubbles were present. Relaxation and creep tests were also performed using this anchorage. The experimental setup is shown in Figure 3-8. The pipe at the dead end was grouted first and left to set. The live end consisted of one pipe in front of and one behind the hydraulic jack. The front pipe was grouted,

and then after 3 hours, the hydraulic jack was pumped to push the front pipe. The rear locking pipe was then injected with grout to lock the bar, and after 3 hours, the hydraulic jack was released. The anchorage was able to successfully prestress the AFRP bar up to 60 percent of the bar's ultimate capacity, and the anchorage was able to sustain the load without significant prestressing losses. This anchorage was used in the uniaxial tests conducted by Pirayeh Gar et al. (2013), in which the anchorage was able to successfully reach the bar's ultimate stress.

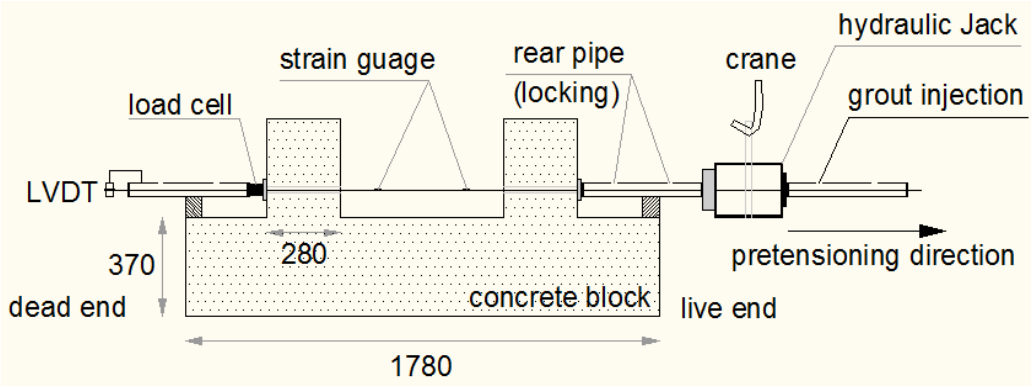

Figure 3-8. Experimental Setup for Preliminary Anchorage Tests (Pirayeh Gar 2012).

Although this anchorage proved to be applicable and reliable, it is not suited for prestressing the AASHTO I-girder Type I. According to Pirayeh Gar (2012), the hydraulic jack was used to prestress the AFRP bars, held in place while the locking pipe was grouted, and then released after 3 hours once the grout had fully set. However, this is not a feasible solution for prestressing the girder because the prestressing bars are congested in the bottom flange and do not allow the hydraulic jack to be held in place. Therefore, another anchorage system is required.

Potted anchorages have been used in laboratory tests and engineering practices to successfully prestress FRP bars. Potted anchorages generally consist of an FRP bar embedded in a potting material inside a steel housing. The main drawback of potted anchorages is their

long curing times, which make them impractical for use in the field. Cementitious grout is the recommended potting material because it is consistent, reliable, and less susceptible to deterioration when compared to resin. Cementitious grout transfers the prestressing load by generating significant circumferential pressure on the bar due to the expansive properties of the grout. This circumferential pressure grips the FRP bar without crushing it. The performance of potted anchorages is strongly dependent on factors such as geometry and the potting material of the anchorage. Research shows that a straight sleeve anchorage with a 457-mm (18-in.) length, 48-mm (1.9-in.) outer diameter, and 5-mm (0.2-in.) wall thickness filled with an expansive and quick-setting grout is capable of prestressing 10-mm (0.393-in.) diameter AFRP ARAPREE® bars to their ultimate capacity.

3.2.3 Research Summary

Two types of anchorage systems are commonly used to prestress FRP, wedge anchorages and potted anchorages. Wedge anchorages are composed of a number of wedges, a conical barrel, and an optional sleeve. The load transfer in a wedge anchorage is primarily through the interlocking of the components of the wedge anchorage. The most significant drawback to wedge anchorages is the fact that high stress concentrations tend to form at the loading end of the anchorage. Because FRP is weak in the transverse direction, stress concentrations often cause premature failure due to the wedges crushing the FRP bar. A sleeve can be added to the FRP bar to uniformly distribute the stress and protect the bar from premature failure. Much experimental research has been conducted on wedge anchorages, but a reliable universal wedge anchorage that can be used with all types of FRP has yet to be produced. Potted anchorages consist of an FRP bar embedded in a potting material that is confined by the walls of a housing (ACI 440R-04). Straight sleeve anchorages are preferred because they are simpler to design and manufacture. Cementitious grout is preferred over resin as the potting material because of its availability, low cost, and ease of preparation (Zhang and Benmokrane 2004). The load transfer mechanism for potted anchorages is based on the circumferential pressure that the grout generates. Because of this, the performance of potted anchorages is highly dependent on the geometry and potting material used. The most significant drawbacks to potted anchorage systems are their difficulty of assembly, long setting times, non-reusability, and the fact that if changes are made, the entire anchorage and bar assembly has to be replaced.

3.3 The Developed Prestressing Anchorage System

As discussed previously, a wedge-type anchorage system is not recommended due to the weakness of the AFRP bars in the transverse direction triggering premature failure. The anchorage developed by Pirayeh Gar (2012) was used to prestress AFRP bars for use in prestressed precast AFRP concrete bridge deck slabs. This anchorage system would not be appropriate for use in prestressing the AFRP bars in the AASHTO I-girder Type I because the bars are spaced too closely. Also, in order to use the anchorage system developed by Pirayeh Gar (2012), the AFRP bars would have to span the entire length of the prestressing bed, which would be uneconomical. Therefore, a new potted-type anchorage system was developed to prestress the bridge girder.

The initial design of the potted anchorage system is presented in Figure 3-9. The anchorage system was composed of a steel pipe with a 914-mm (36-in.) length, 48-mm (1.9-in.) outer diameter, and 5-mm (0.2-in.) wall thickness filled with an expansive and quick-setting grout. A 10-mm (0.394-in.) diameter AFRP bar and a 15-mm (0.6-in.) diameter steel strand were passed through the center of the pipe on either side and held in place by plastic stoppers, which had central holes. Styrofoam was placed in the center of the pipe to separate the grout and allow each side to be grouted individually. Surface holes were drilled in the pipe for injecting the grout. The grout was poured through the first hole until it flushed the pipe's surface at the second hole to ensure that no air bubbles were entrapped.

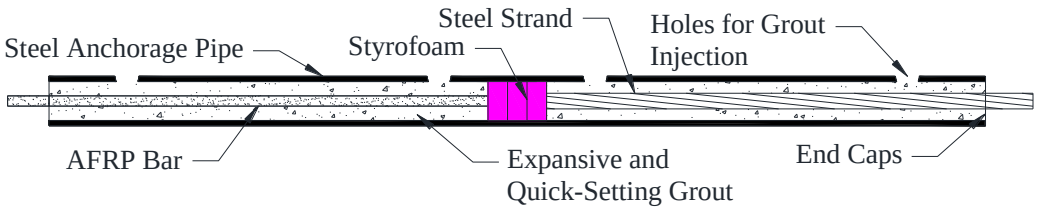

Figure 3-9. Initial Anchorage Design.

3.4 Anchorage Tests

The prestressing anchorage system should be able to sustain the target prestressing load of 60 percent of the bar's ultimate capacity without facing any major loss in prestressing force or premature failure. To verify the capacity and sustainability of the anchorage, short-term and long-term tests were conducted, respectively. The experimental setup for the short-term or load capacity test is shown in Figure 3-10. Two steel angles were anchored to the strong floor at the High Bay Structural and Materials Testing Laboratory via 51-mm (2-in.) diameter threaded rods. The dead end was composed of a steel pipe with a 914-mm (36-in.) length, 48-mm (1.9-in.) outer diameter, and 5-mm (0.2-in.) wall thickness filled with an expansive and quick-setting grout. The AFRP bar was passed through the center of the pipe and held in place by a plastic stopper on one end. An internally threaded bushing was pot-welded inside the pipe on the other end, and a piece of Styrofoam was placed in front of the bushing to prevent the grout from leaking onto the threads. A steel plate with a central bolt was secured to the steel angle to accommodate the dead end. A center-hole jack pushing against a conventional wedge anchor was used to stress the system. A load cell was placed in front of the center-hole jack to measure the prestressing force, and LVDTs were placed at each of the strand-anchorage interfaces to measure the slip of the bars inside the anchorage. The hydraulic center-hole jack was pumped manually in a slow, smooth fashion until failure occurred somewhere in the system. For the load capacity tests, AFRP rupture outside the anchorage zone is the desired failure mode because it indicates that the load capacity of the anchorage is not less than the bar's ultimate capacity.

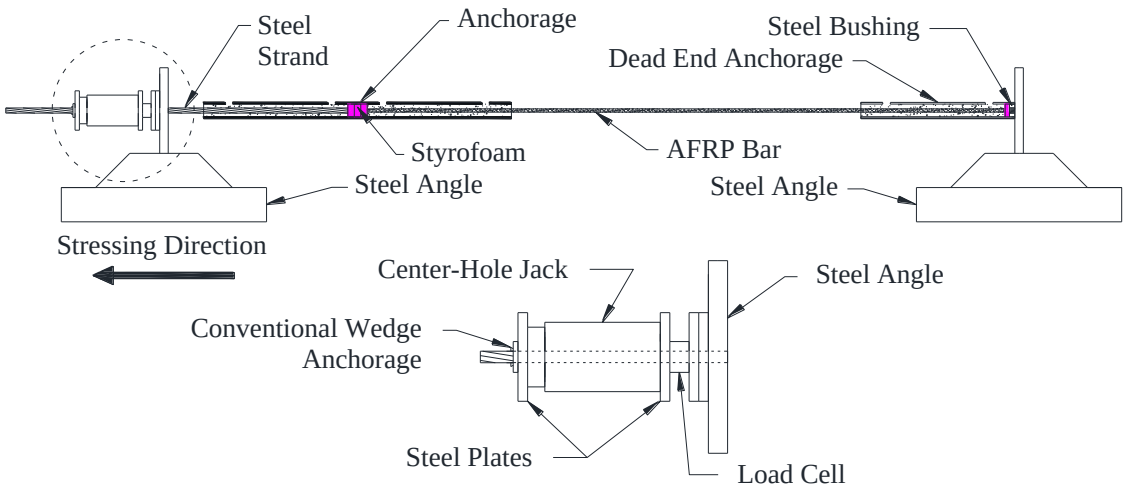

Figure 3-10. Load Capacity Test Experimental Setup.

3.5 The Load Capacity Tests

Two specimens using the initial anchorage design were tested in tension until failure. In both cases, the test was terminated due to grout pullout at the steel end of the anchorage and the dead end, respectively. An example of grout pullout failure is shown in Figure 3-11. Both failures were premature, occurring at about 42 and 50 percent of the bar's ultimate capacity, respectively. Grout pullout failure suggests that the bond between the grout and the anchorage pipe was insufficient. Further investigation after the test revealed an oily residue on the surface of the grout that had been pulled out from the anchorage. A third specimen was tested using anchorage pipes that had been cleaned thoroughly. The dimensions and instrumentation were identical to the previous test. The test was terminated due to grout pullout at the steel end at a prestressing load of about 54 kN (12 kips), corresponding to 50 percent of the bar's ultimate capacity. Figure 3-12 presents the results of the load capacity test of the initial anchorage design. As seen, the load drops significantly any time the grout slips.

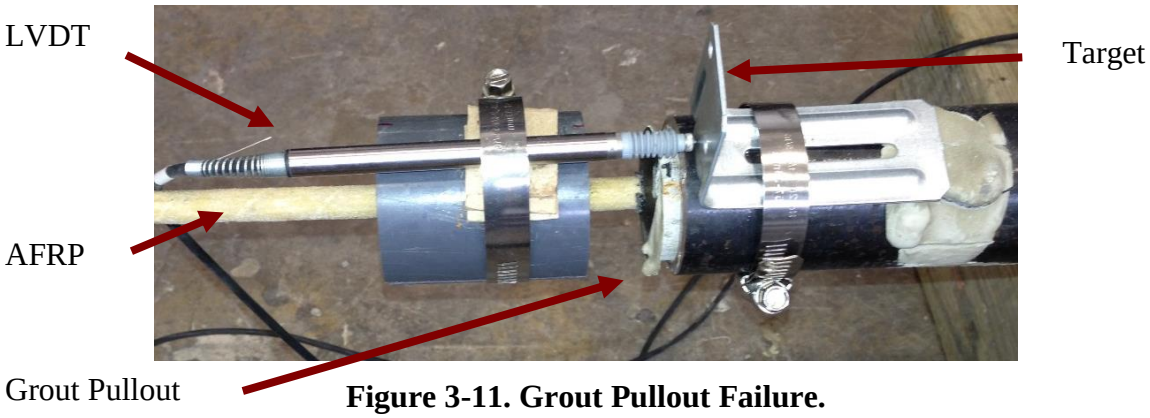

Figure 3-11. Grout Pullout Failure.

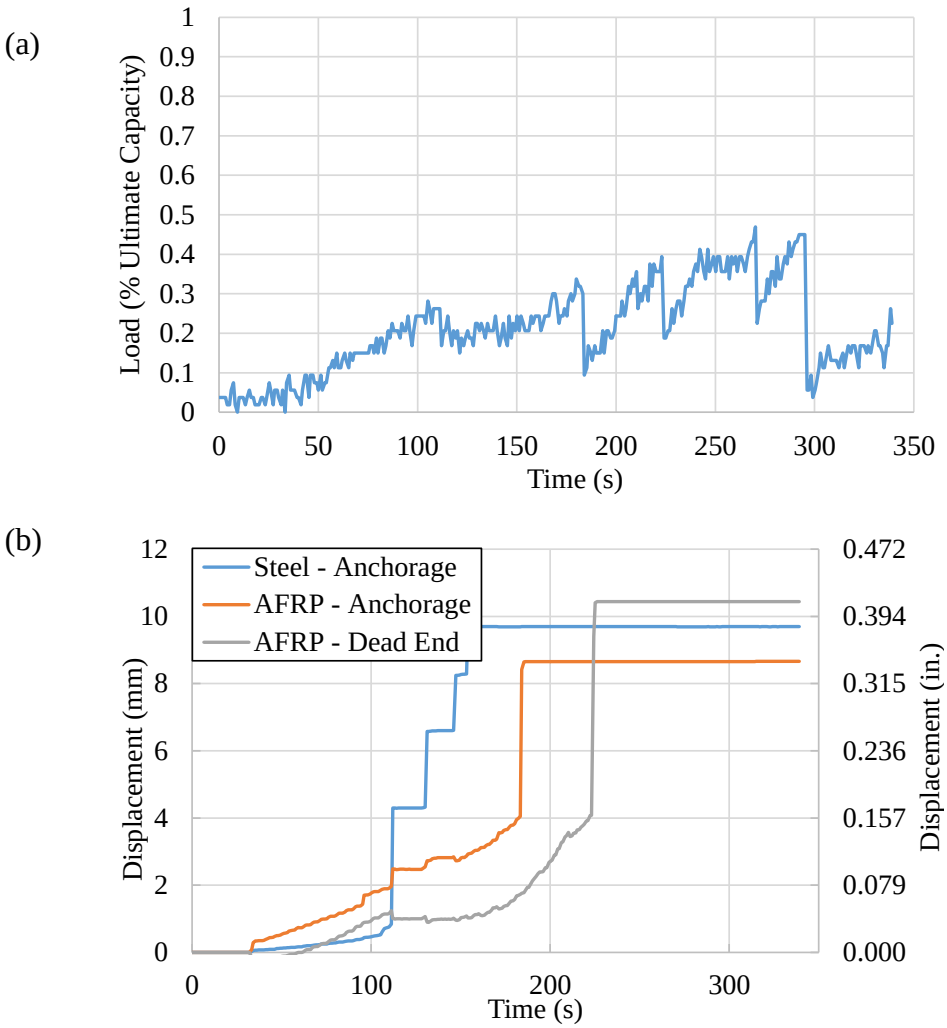

Figure 3-12. Load Capacity Test Results of Initial Anchorage Design: (a) Load Capacity and (b) Anchorage Slip.

In order to increase the bond between the grout and the anchorage pipe, the anchorage pipes were crimped as shown in Figure 3-13 to add a mechanical feature. The pipes were crimped using an MTS® machine set to a specific displacement. A 12.7-mm (0.5-in.) deformation was placed every 50.8 mm (2 in.) along the length of the pipe, with a 90° rotation in between crimps. The new crimped anchorage system was tested in tension until failure. The test was terminated due to AFRP pullout at the dead end at a load approximately equal to the bar's ultimate capacity. The results of the load capacity test using the crimped anchorage system are presented in Figure 3-14. As shown, minimal slip was seen in the anchorage system before failure. Although the crimped anchorage system was able to resist a high prestressing load, the desired failure mode was not present. Bar pullout suggests that the bond strength between the grout and the bar was insufficient. Therefore, the test was repeated to see if the results would be similar. In this test, the anchorage failed due to AFRP pullout at the anchorage location at a load approximately equal to 45 kN (10 kips), corresponding to 42 percent of the bar's ultimate capacity. In all tests, there was a significant amount of torsion occurring in the system. This torsion was likely caused by the steel prestressing strand attempting to unwind as it was pre-tensioned. The presence of torsion could have caused the system to fail prematurely. Although the first test of the crimped anchorage system was a success, the second test suggested that the anchorage was unreliable and should be redesigned.

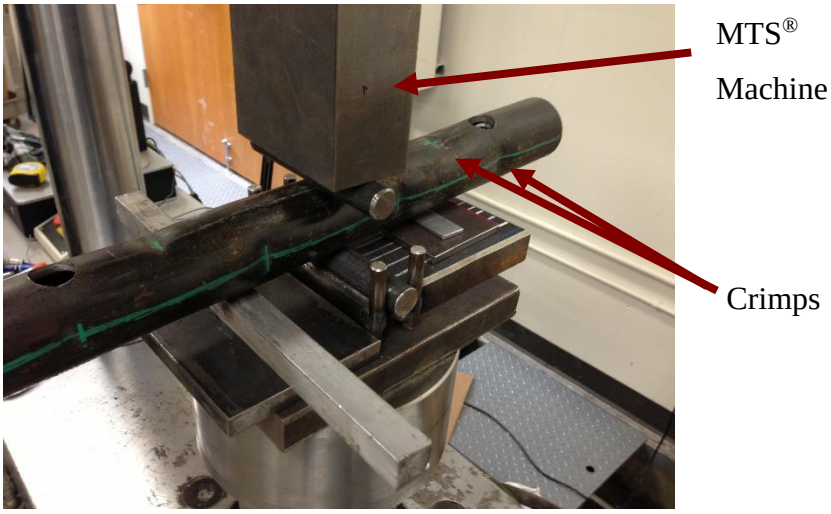

Figure 3-13. Crimped Anchorage Pipe.

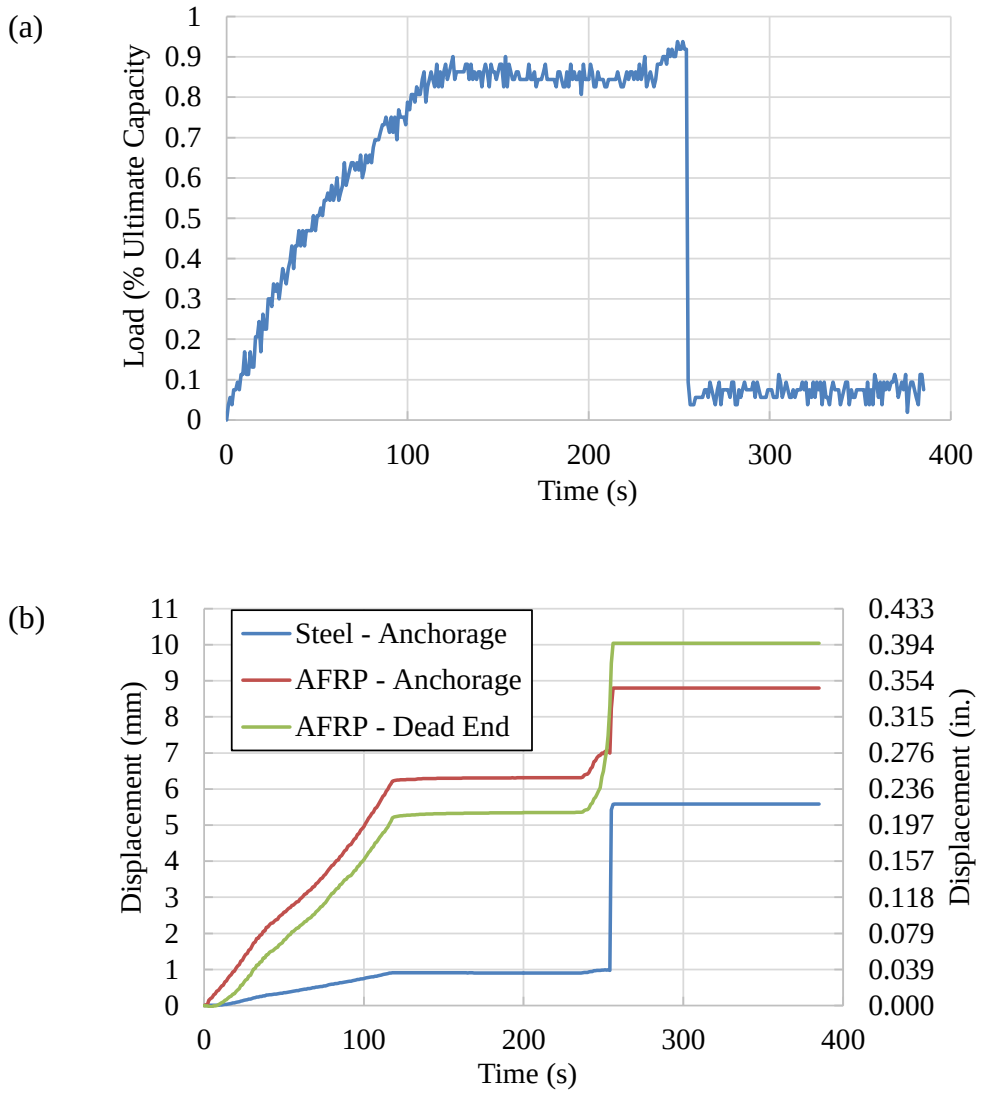

Figure 3-14. Load Capacity Test Results of Crimped Anchorage System: (a) Load Capacity and (b) Anchorage Slip.

To find out if the torsion was really causing the anchorage to fail prematurely, the steel strand was removed from the system, and two tensile tests of AFRP ARAPREE® bars were performed using the same potted anchorage pipe. Two steel pipes were used as anchorages having a 457-mm (18-in.) length, 48-mm (1.9-in.) outer diameter, and 5-mm (0.2-in.) wall thickness filled with an expansive and quick-setting grout. A 10-mm (0.394-in.) diameter AFRP ARAPREE® bar with a 1420-mm (56-in.) length was passed through the center of the

pipes and held in place by plastic stoppers that had a central hole. The specimen was gripped by the jaws of the MTS® machine, as shown in Figure 3-15, and the load was applied at a constant rate of 22 kN (5 kips) per minute, according to ASTM 638. Both specimens failed in a sudden fashion due to AFRP pullout at 78 kN (17.6 kips) and 81 kN (18.2 kips), respectively. Displacements for the tensile tests are shown in Figure 3-16. No slip was seen before the specimen failed due to bar pullout, which implied that the bond between the grout and the bar was insufficient regardless of any torsional effect. However, in both tests the load at failure was higher than that of the load capacity tests, confirming that torsion did not help to increase the strength of the anchorage.

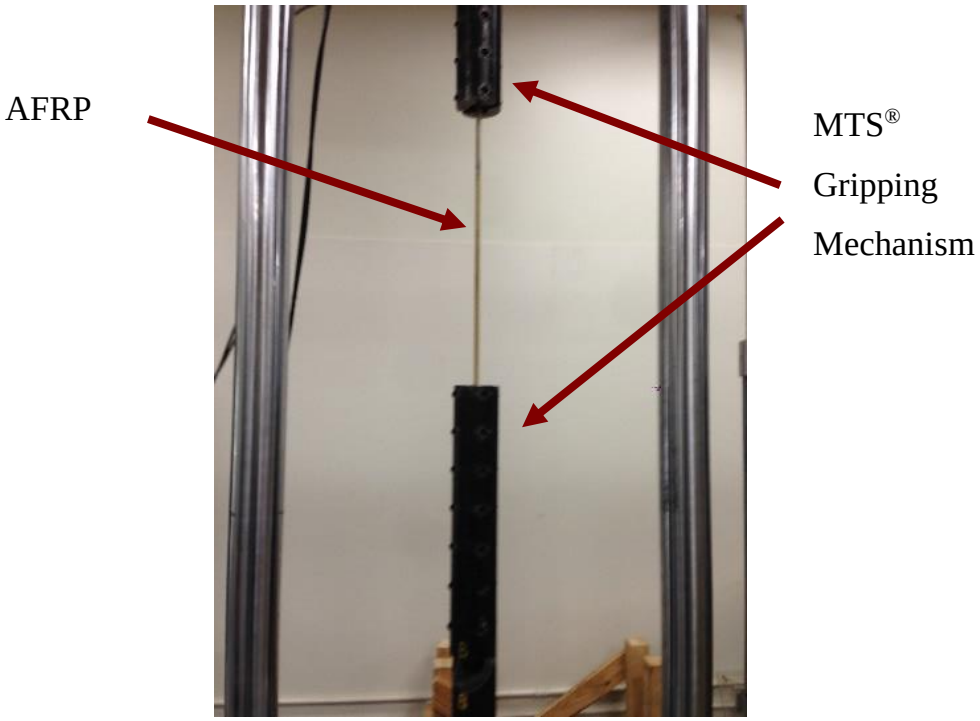

Figure 3-15. Tensile Test Setup.

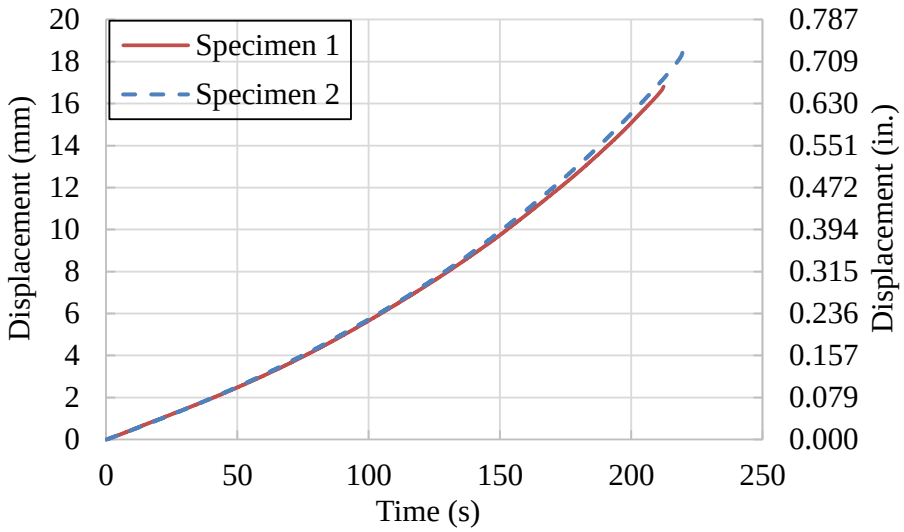

Figure 3-16. Tensile Test Displacement.

The anchorage was redesigned to remove any torsional effect and also to increase the bond strength between the bar and the grout. The 15-mm (0.6-in.) diameter steel strand was replaced with a 14.3-mm (0.563-in.) diameter threaded rod with a minimum tensile strength of 860 MPa (125 ksi) to remove any torsional effects. Furthermore, the grout length was extended to 916 mm (36 in.) at the dead end and 610 mm (24 in.) at the AFRP end of the anchorage, and decreased to only 203 mm (8 in.) at the steel end of the anchorage to enhance the bond strength between the AFRP bar and the grout. The plastic stoppers were replaced with 25.4-mm (1-in.) steel bushings with a central hole pot-welded inside the pipe to prevent grout pullout failure. This pot-welded steel bushing also created a compressive stress on the grout, which increased the tensile capacity of the grout. A long-term test was carried out on the anchorage. The experimental setup for the long-term test is shown in Figure 3-17. The conventional wedge anchorage behind the hydraulic jack was replaced with a steel plate, a washer, and a high-strength nut. A high-strength locking nut was added to hold the load once the desired prestressing load was reached. A steel pipe with a surface hole was placed in front of the jack to adjust and set the locking nut. Once the prestressing load was reached, the locking nut was tightened to sustain the load, and the hydraulic jack was released. The data acquisition system recorded data every 5 minutes for 3 days. A load cell was placed in front of the center-hole

jack to measure the prestressing force, and LVDTs were placed at each of the strand-anchorage interfaces to measure the slip of the bars inside the anchorage. The slips inside anchorage components are presented in Figure 3-18. The anchorage was able to sustain the prestressing load with minimal slip for about 50 hours. After 50 hours, significant slip was seen at the AFRP end of the anchorage. Minimal to no slip was seen at the dead end, however. Considering that the grout length at the dead end was 306 mm (8 in.) longer than at the anchorage, a 916-mm (36-in.) grout length at the anchorage should be able to sustain the desired prestressing load with minimal to no slip.

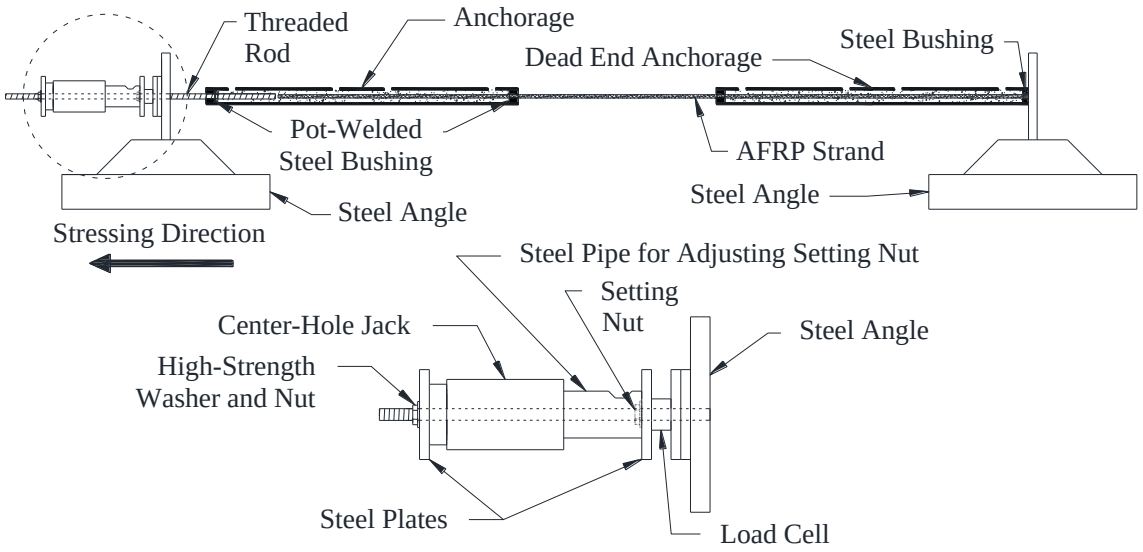

Figure 3-17. Long-Term Test Setup.

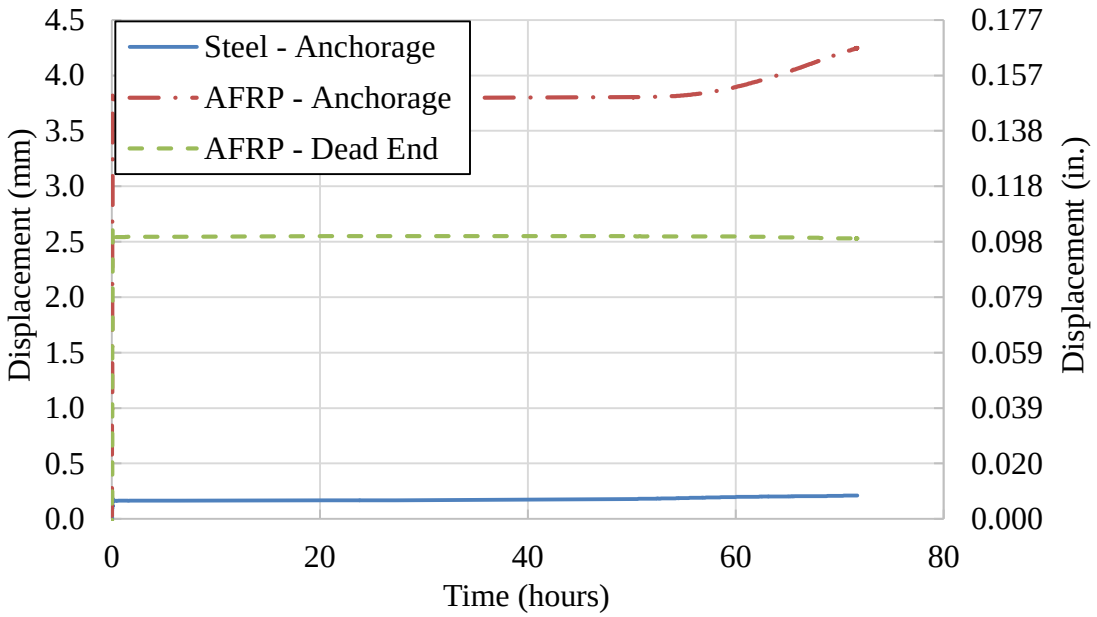

Figure 3-18. Long-Term Anchorage Slip.

The anchorage was eventually redesigned to prevent slip at every location on the anchorage. The grout length was extended to 916 mm (36 in.) at the dead end and the AFRP end of the anchorage, and was removed at the steel end of the anchorage to increase the bond strength between the AFRP bar and the grout. The steel end of the anchorage consisted of a high-strength washer and nut on the threaded rod that was bearing on the pot-welded steel bushing inside the pipe. The final anchorage was tested using a procedure identical to the previous long-term test. The results of the final anchorage test are shown in Figure 3-19. The anchorage proved to be reliable by sustaining the desired prestressing load for 3 days with minimal to no slip. The final anchorage design is presented in Figure 3-20.

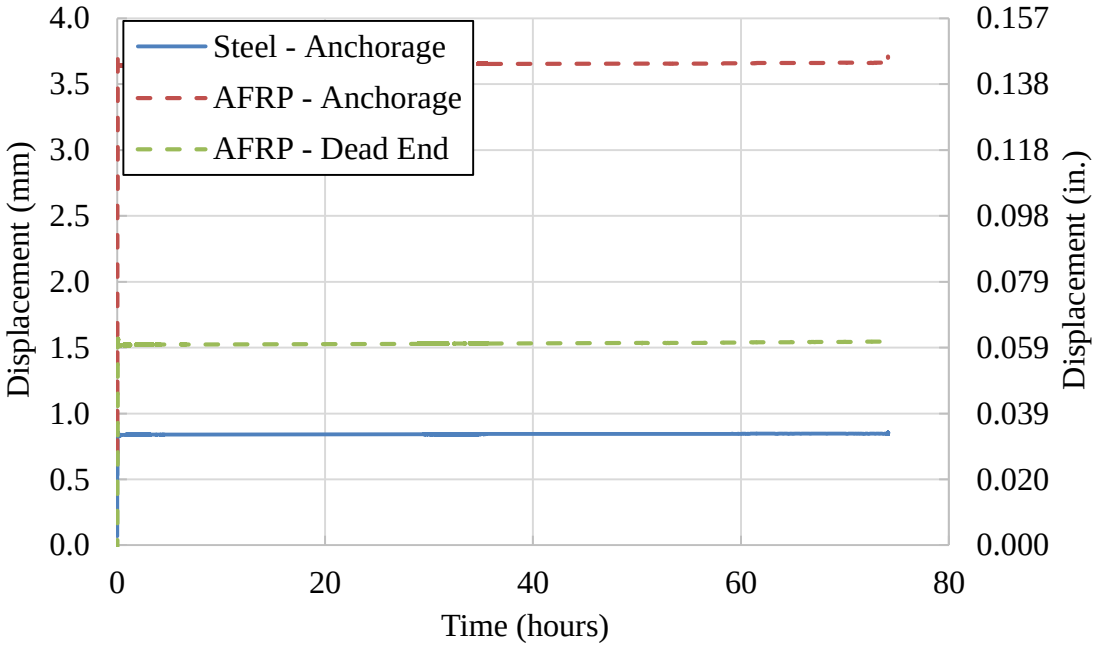

Figure 3-19. Long-Term Slip of Final Anchorage Design.

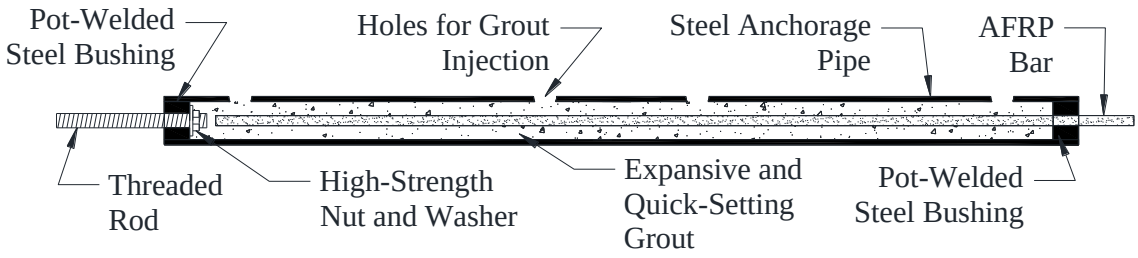

Figure 3-20. Final Anchorage Design.

4 CONSTRUCTION PROCESS

4.1 Introduction

Construction of the AFRP concrete AASHTO I-girder Type I took place over a span of 6 days at a prestressing plant in San Marcos, Texas. The weather was in the high 90s to low 100s for all six days. The special anchorage, as discussed in Chapter 3, was used to pretension all 24 prestressed AFRP bars. Steel side forms in the shape of the AASHTO I-girder Type I and wooden end forms were placed to confine the concrete. Once the girder was constructed, it was transported to a separate prestressing bed, and the formwork for the deck was built around the existing girder. The deck was longitudinally and transversely reinforced with conventional steel rebar. Once the AASHTO I-girder Type I with the topping deck was constructed as a composite section, it was transported to the High Bay Structural and Materials Testing Laboratory on the campus of Texas A&M University for further testing. This chapter discusses the construction process of the AASHTO I-girder Type I composite with the topping deck and points out the construction advantages and issues.

4.2 Girder Reinforcement

As discussed in Chapter 2, the cross-section of the AASHTO I-girder Type I is composed of self-consolidating concrete reinforced with both prestressed and non-prestressed AFRP bars having a 10-mm (0.393-in.) diameter. The dimensions and longitudinal reinforcement layout are shown in Figure 2-1. Twenty-four prestressed AFRP bars were used within the girder section: 22 in the bottom flange and two in the top flange. The two prestressed AFRP bars in the top flange of the girder were attached to the stressing bed using steel extension plates, as shown in Figure 4-1. The extension plates were connected to the stressing bed using a 14.3-mm (0.563-in.) diameter threaded rod and high-strength nuts and washers. Eight non-prestressed AFRP bars were used within the girder section: six in the web and two in the top flange. The non-prestressed bars were placed with the aid of the wooden end form, which will be discussed later.

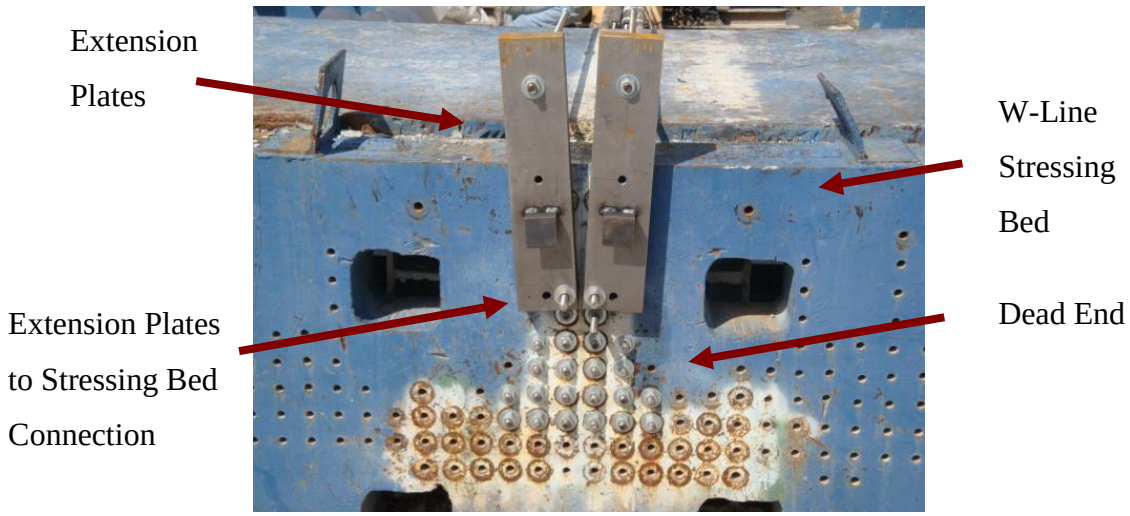

Figure 4-1. Dead End of the Stressing Bed.

The shear reinforcement layout is presented in Figure 2-1 and Figure 2-2. R-shape AFRP ARAPREE® bars of a 10-mm (0.393-in.) diameter formed the shear reinforcement. Steel shear bolts with a 381-mm (15-in.) length were added at the girder-to-deck interface to provide additional shear resistance against the horizontal shear force developed through the composite action. All shear reinforcement was attached to the longitudinal reinforcement with conventional steel rebar ties. The process of placing the shear and non-prestressed longitudinal reinforcement was convenient and quick due to the light weight of the AFRP bars.

4.3 AFRP Bar-Bending Procedure

The R-shape stirrups were bent out of the straight AFRP bars at Texas A&M University using the bending process previously investigated by Pirayeh Gar (2012). The bending process is shown in Figure 4-2 and includes heating the bar with a heat gun to somewhat soften the resin matrix and then pressing the bar using a rubber mallet and a mediator plate to avoid damaging the fibers. The bars are eventually bent around the bending apparatus and are kept in their final bent position as the resin cools very quickly.

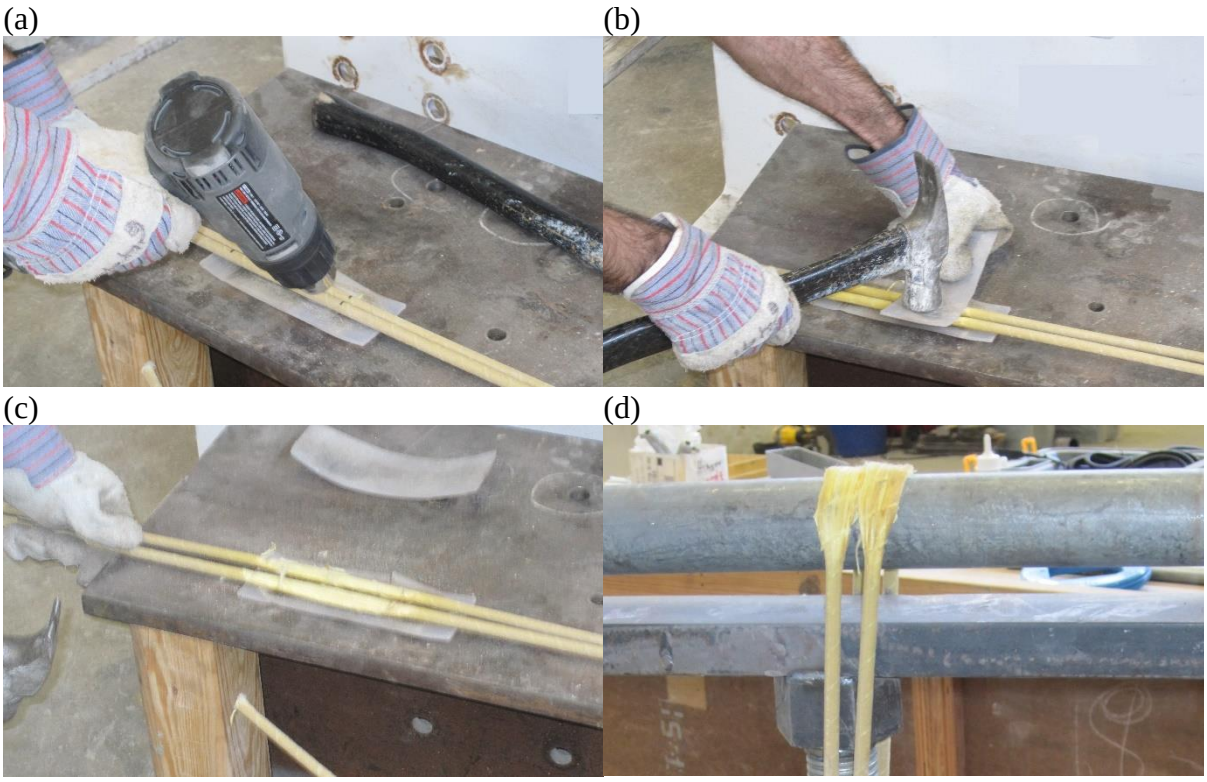

Figure 4-2. AFRP Bar-Bending Process: (a) Heating the Bar with a Heat Gun, (b) Pressing the Bar, (c) Viewing the Softened Resin Matrix, and (d) Bending the Bars (Pirayeh Gar 2012).

4.4 Deck Reinforcement

Conventional steel rebar was placed within the topping deck to reinforce the slab either longitudinally or transversely. AFRP reinforcement was not used in the topping deck because the deck was built only to provide a composite action with the girder. The longitudinal reinforcement was composed of two D16 (#5) rebar bisecting the center, six D13 (#4) rebar spaced at 203 mm (8 in.) apart on the bottom, and nine D13 (#4) rebar spaced at 178 mm (7 in.) centered on the top. The transverse reinforcement was composed of sixty D13 (#4) rebar placed 203 mm (8 in.) apart on the top and bottom. The deck reinforcement detail is shown in Figure 2-3.

4.5 Prestressing Operation

The AASHTO I-girder Type I, with composite deck, was constructed using a 24-m (79-ft.) long W-line stressing bed at a prestressing plant in San Marcos Texas. The 16.75-m (55-ft.) AFRP bars were pre-tensioned using the anchorage system as discussed in Chapter 3. The prestressing anchorage consisted of a 914-mm (36-in.) long steel pipe filled with an expansive and quick-setting grout and is shown in Figure 3-20. The AFRP bar was passed through the length of the pipe and held in the center by a steel bushing pot-welded inside the pipe with a central hole. A 14.3-mm (0.563-in.) diameter threaded rod was fastened at the opposite end of the pipe with a high-strength nut and washer bearing on a pot-welded steel bushing. The anchorage at the dead end for each AFRP bar was grouted at Texas A&M University and transported to the prestressing plant.

The threaded rods at the dead ends were passed through the holes in the stressing bed and anchored with high-strength washers and nuts. The AFRP bars were then passed through the holes of two wooden formworks shaped as the cross-section of the AASHTO I-girder Type I. The anchorages at the live end were then grouted and left to set before the bars were pre-tensioned. Once the live end anchorages were set, the threaded rod at the live end was passed through the holes in the stressing bed and secured with a setting nut and washer. The live end of the prestressing system is shown in Figure 4-3 and Figure 4-4. A hydraulic center-hole jack was used to pre-tension the AFRP bars individually, where the prestressing load was monitored through the pressure from the hydraulic jack. The steel pipe had a surface hole to allow the setting nut to be adjusted as the bar was pre-tensioned. The hydraulic jack pushed against a steel plate held in place by a high-strength nut and washer to stress the AFRP bar. The threaded rod at the live end was extended via a coupling nut and another section of threaded rod. As the hydraulic jack was extended, the setting nut in front of the coupling nut was tightened periodically with a screwdriver to hold the prestressing load. This process was repeated for each AFRP bar in the girder's cross-section. Each bar required about 10 minutes to be prestressed. Due to some failures that occurred, as will be discussed, the entire prestressing operation lasted approximately 6 hours.

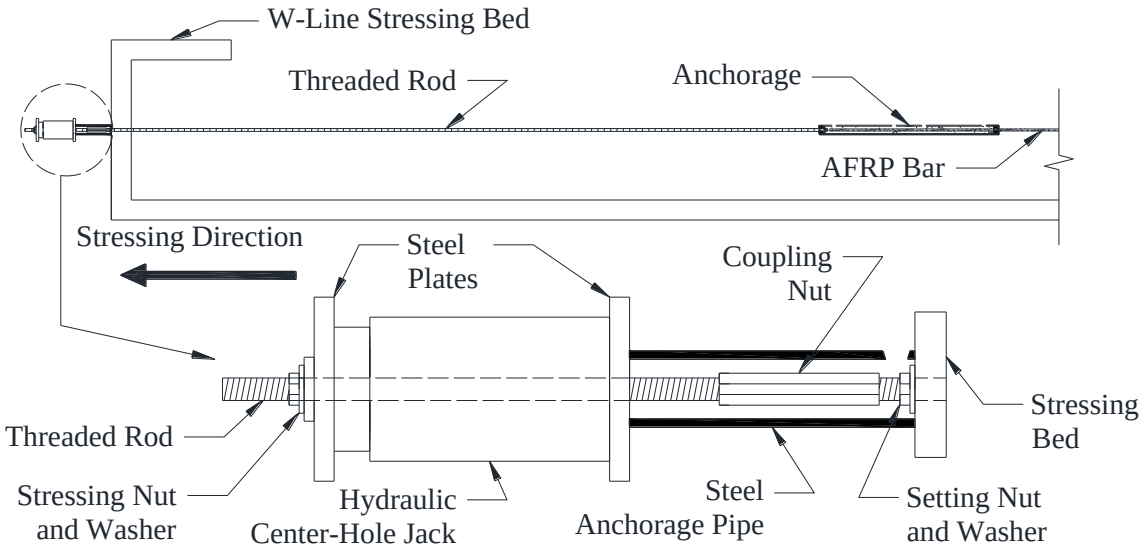

Figure 4-3. Stressing End Detail.

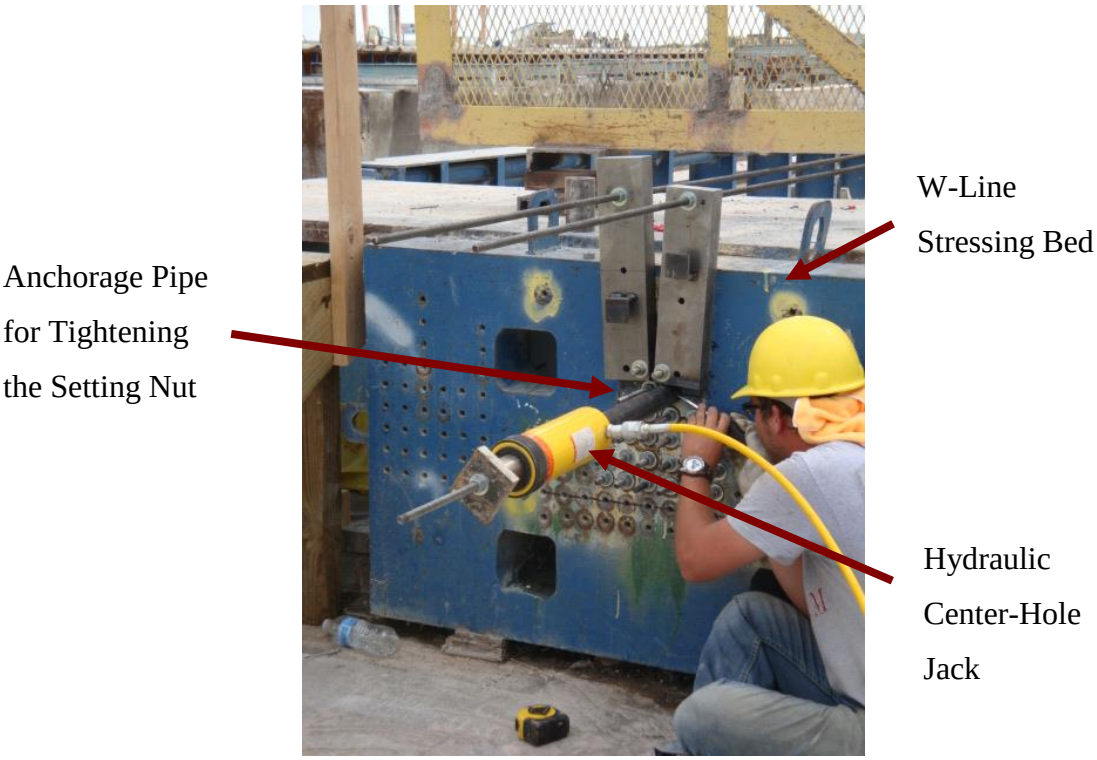

Figure 4-4. Prestressing Setup—Live End.

Once all of the AFRP bars were pre-tensioned, the wooden end forms were placed to create a girder with a 12.2-m (40-ft.) length. The non-prestressed AFRP bars were cut to the target length, placed in the proper position, and held in place by the wooden end form. Once all of the longitudinal reinforcement was in place, the shear reinforcement was placed and tied to the AFRP bars using conventional steel rebar ties. Form oil was applied to the steel formwork and wooden end forms for the AASHTO I-girder Type I and placed using a Mi-Jack crane. The formwork and reinforcement of the girder are presented in Figure 4-5. Steel brackets were used at the top and bottom of the steel forms to keep them in place while the concrete was poured. Two lifting points made of steel strands were placed at 2.5 m (8 ft.) from each end to transport the girder.

Figure 4-5. Girder Formwork and Reinforcement.

4.6 Concrete Placement

The concrete for the girder was poured using one batch of self-consolidating concrete and left to cure for 3 days. Before the concrete was poured, a sample was taken in order to determine the fresh characteristics of the concrete including slump, unit weight, and concrete strength. The target 28-day strength of concrete was about 69 MPa (10 ksi). The falling height

of the concrete did not exceed 1.5 m (5 ft.) at any time during the pour. Self-consolidating concrete does not require vibration; however, the steel side forms were vibrated in order to remove any unwanted air bubbles. The concrete itself was not vibrated to avoid possible damage to the AFRP bars. Once the concrete for the girder was poured, the top surface of the girder was roughened using a steel brush to provide more shear interlocks at the girder-to-deck interface. The concrete was covered with burlap, and moisture was added using a mechanical soaker for the duration of the curing period. Figure 4-6 shows the casted concrete girder.

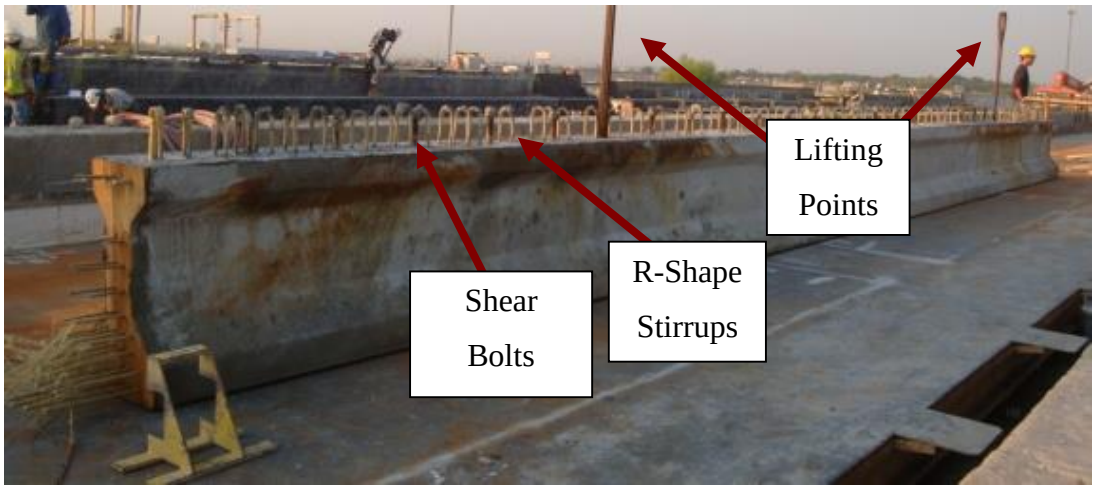

Figure 4-6. AFRP Reinforced AASHTO Type-I Bridge Girder.

After 3 days of concrete curing, compressive strength tests showed a concrete strength of 55 MPa (8 ksi). The AFRP bars were then cut with a hacksaw, and the specimen was transported to a separate stressing bed to build the formwork for the deck. A plywood platform was built up around the girder and used as the bottom formwork for the topping deck. Prefabricated wooden forms were then secured to the plywood platform to create a 203-mm (8-in.) high formwork for the sides of the deck. The formwork was coated with form oil, and the conventional steel reinforcement for the deck was placed. The formwork and steel reinforcement for the deck are shown in Figure 4-7.

The concrete for the topping deck was poured using two batches of self-consolidating concrete and left to cure overnight before the formwork was removed. Before each batch was poured, a sample was taken to determine the fresh characteristics of the concrete. The target 28-day strength of concrete was about 69 MPa (10 ksi). The falling height of the concrete did not exceed 1.5 m (5 ft.) at any time during the pour. The concrete was vibrated using a mechanical vibrator to ensure no unwanted air bubbles were present. The top surface of the deck was finished with a concrete float to create a smooth surface. The concrete was covered with burlap, and moisture was added using a mechanical soaker for the duration of the curing period. After 1 day of curing, the concrete reached a strength approximately equal to 34.5 MPa (5 ksi), and hence the formwork was removed. The AASHTO I-girder Type I with composite deck is presented in Figure 4-8.

Figure 4-7. Deck Formwork and Reinforcement.

Figure 4-8. AFRP Reinforced AASHTO I-Girder Type I with Composite Deck.

4.7 Constructability Issues

The original prestressing plan required each AFRP bar to be prestressed up to 54 percent of the AFRP bar's ultimate capacity. During the prestressing process, three AFRP bars failed due to AFRP rupture outside of the anchorage. These bars were replaced, re-grouted, and pre-tensioned up to 40 percent of ultimate capacity successfully except one, which was prestressed up to only 24 percent of ultimate capacity. Therefore, to reduce the risk of further failures, the remaining AFRP bars were all similarly pre-tensioned to 40 percent of the ultimate capacity. The final prestressing load for each AFRP bar is presented in Figure 4-9.

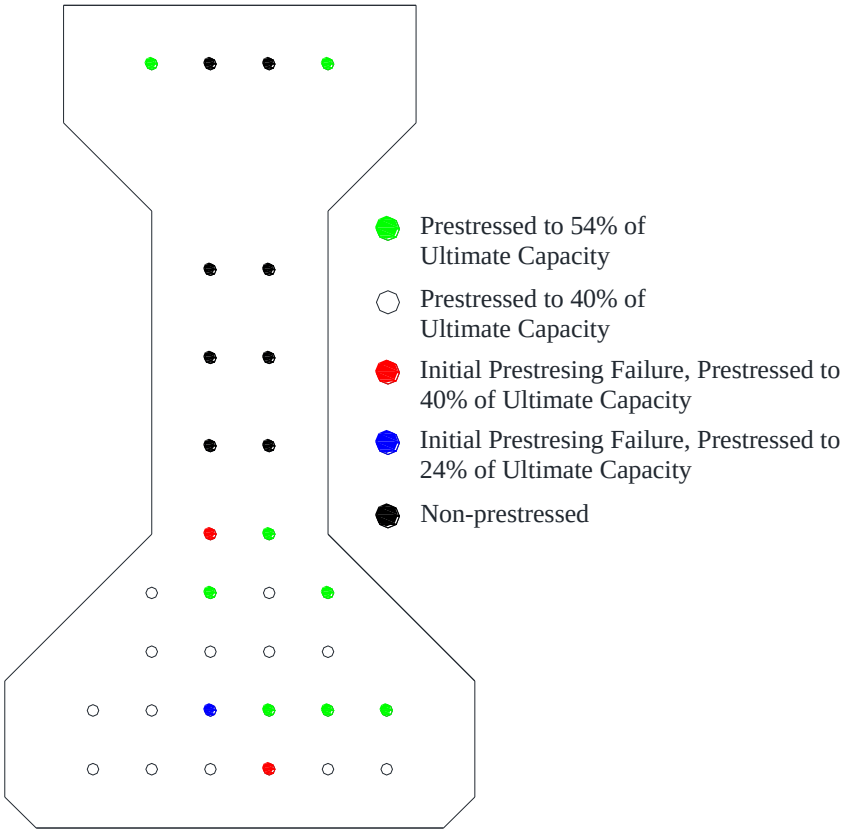

Figure 4-9. Individual Prestressing Loads.

Due to the intense heat, complications arose during the grouting process. The water used for mixing the grout was too hot, which caused the grout to set extremely quickly. Because of this, grouting was delayed until very early the next morning when the outside temperature was more reasonable. The authors recommend to use ice water during the grouting process when the outside temperature is very high to avoid premature setting of the grout.

4.8 Conclusion

The process of placing the shear and non-prestressed longitudinal reinforcement was convenient and quick due to the light weight of the AFRP bars. One person could easily carry and place the bars without assistance from heavy machinery. This is the main advantage of AFRP bars for construction compared to conventional steel rebar. The transportation of reinforcement alone can be costly and time consuming when constructing large structural

members reinforced with conventional steel reinforcement. The light weight of AFRP provided ease of placement in the field and lower transportation costs. Furthermore, any possible replacement of reinforcement due to future repair and rehabilitation plans will cause shorter downtime compared to conventional reinforcement.

Also, once the AFRP bars are bent, the shape can be easily adjusted to fit the need. For example, if the angles of the bends for the top and bottom bars are not exactly correct, they can be adjusted by hand to fit into the cross-section of the girder. This is not an option with conventional steel reinforcement.

The construction process took place over a span of 6 days. The main constructability issue was the premature failure that occurred for some of the AFRP bars during the prestressing operation. A few of the prestressed AFRP bars failed during the pre-tensioning process due to AFRP rupture outside of the anchorage. This suggests that the anchorage itself had a sufficient grip on the bar, but the capacity of the AFRP bar was exceeded. This failure could be attributed to either inconsistencies in the material properties or damage during transportation. The prestressing operation required the majority of the time spent manufacturing the girder. A large component of this time was the fact that the potted anchorages at the live end required on-site manufacturing. Prefabrication of the potted anchorages at both ends of the prestressed AFRP bars would have significantly shortened the construction schedule.

5 EXPERIMENTAL RESULTS

5.1 Introduction

This chapter discusses the experimental performance of the AASHTO I-girder Type I in both flexure and shear. The specimen was tested at the High Bay Structural and Materials Testing Laboratory on the campus of Texas A&M University. The main focus of the flexure test was on the load and deformation capacities, moment-curvature relationship, failure mode, and crack patterns. Furthermore, the experimental deflection profile and curvature distribution along the girder were also studied to better understand the global response of the girder at post-cracking levels of loading. After the flexure test, two shear tests were conducted at both uncracked ends of the girder to measure the shear capacity, failure mode, and crack patterns, and to verify the embedment length. Finally, all the experimental results were compared with the control specimen reinforced with conventional steel rebar and prestressing strands (Trejo et al. 2008).

5.2 Flexure Test

The flexure test was conducted under a four-point configuration of loading, which was increased monotonically until flexural failure. The flexure test setup is illustrated in Chapter 2. A 2700-kN (600-kips) actuator, which was attached to the steel loading frame, was used to apply load to the specimen. The load points were spaced 914 mm (36 in.) apart and provided a constant moment region at the midspan of the specimen. The specimen was manually loaded under displacement control at a rate approximately equal to 44 kN (10 kips) per minute before first cracking at the midspan, and then decreased to 22 kN (5 kips) per minute. The load was halted periodically to record and mark the flexural cracks.

5.2.1 Load and Deformation Capacity

Figure 5-1 presents the experimental and analytical moment-curvature graphs. As shown, the moment-curvature behavior of the specimen is linear before and after cracking. However, the experiment also shows a plateau around M = 550 kNm (406 kft.) corresponding to a trilinear behavior, with clear pre-cracking, cracking, and post-cracking regions instead of the expected bilinear behavior. The cracking and ultimate moment of the experimental specimen were M_{cr} = 542.3 kNm (400 kft.) and M_n = 1563.2 kNm (1153 kft.), respectively. Excluding

the dead load of the girder and deck from the service loads calculated by Pirayeh Gar et al. (2014), gives service live loads equal to 611 kNm (450 kft.) which is greater than the cracking moment. For this reason the girder is classified as a partially prestressed beam and minor cracking might be permitted under service loads.

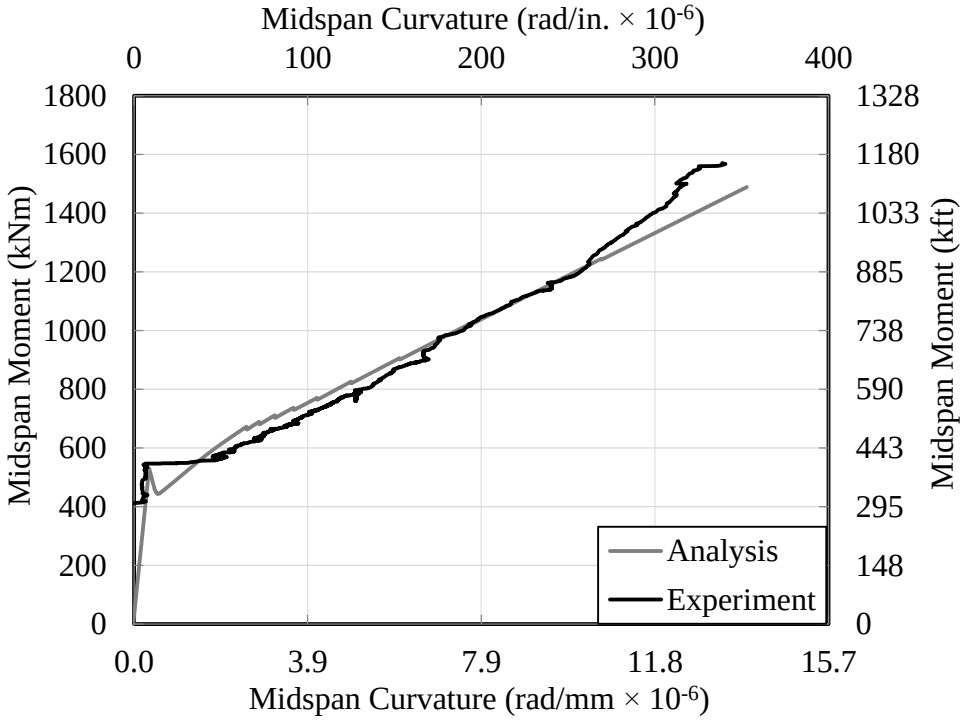

Figure 5-1. Moment-Curvature Response. (Pirayeh Gar et al. 2014)

The capacity of the experimental specimen was equal to M_n = 1563.2 kNm (1153 kft.) which satisfies the ultimate state by exceeding the maximum factored load of 1326 kNm (978 kft.), per the AASHTO LRFD *Bridge Design Specification* (2010). As shown the curvature at the ultimate state equal to 1.34×10^{-5} rad/mm (3.36×10^{-4} rad/in.) is about 25 times greater than that of the cracking curvature. The reduced elastic modulus of the AFRP bars when compared to conventional steel strands allows the specimen to show improved ductility. The analytical

result conducted by Pirayeh Gar et al. (2014) compared very well to the experimental specimen.

Unlike the moment-curvature response, the load-deflection response (Figure 5-2) displays the expected bilinear behavior. The cracking and ultimate loads of the experimental specimen were equal to P_{cr} = 197.5 kN (44.4 kips) and P_u = 569.8 kN (128.1 kips), respectively. Again the analytical load-deflection behavior was calculated by Pirayeh Gar et al. (2014) and compared very well to the experimental specimen.

The serviceability limit for live load deflection control governed by the AASHTO *LRFD Bridge Design Specification* (AASHTO 2010) was equal to the girder's length divided by 800 corresponding to a live load deflection of 14.8 mm (0.58 in.). The experimental live load deflection of the girder was equal to 11 mm (0.44 in.) which satisfies the serviceability limit corresponding to deflection control.

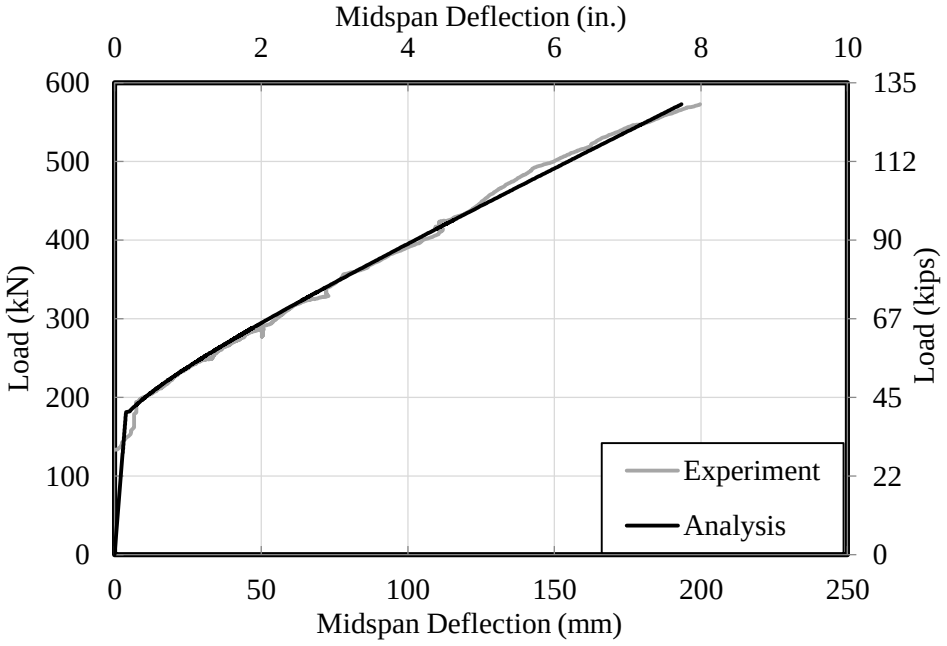

Figure 5-2. Load-Deflection Response. (Pirayeh Gar et al. 2014)

5.2.2 Failure Mode and Cracking Pattern

Flexural cracks were observed at the midspan upon reaching the cracking load, and then propagated beyond the constant moment region (shear span) as the load was monotonically increased. In the shear span, the flexural cracks were inclined due to the presence of shear and propagated toward the end supports. The crack spacing was between 152.4 mm (6 in.) and 203.2 mm (8 in.), which is close to the stirrup spacing. Because the shear-span-to-depth ratio (a/d = 6.9) was close to 7, the beam was categorized as a very slender beam (Park and Paulay 1975), and hence the failure mode of the girder was expected to be mostly governed by flexure or beam action. Such a failure mode was confirmed by the test where the girder failed due to tendon rupture before the compressive concrete within the topping deck could reach a strain capacity of 0.003.

Figure 5-3 presents the cracking pattern at three different load levels: close to cracking, post-cracking, and prior to failure. A grid net of vertical lines with a 305-mm (12-in.) spacing was used to map the cracks. After a load level of P = 300 kN (67.4 kips), the flexural cracks at the midspan began to enter the topping deck labeled from A to Q. The extensive flexural cracks with considerable width, particularly at the midspan, provided enough warning to imply an impending failure. As discussed, the failure mode of the girder was predicted as tendon rupture since the reinforcement ratio was considerably less than the brittle ratio and the section was categorized as an under-reinforced section. A close view of the failure zone at the bottom flange with tendon rupture is presented in Figure 5-4.

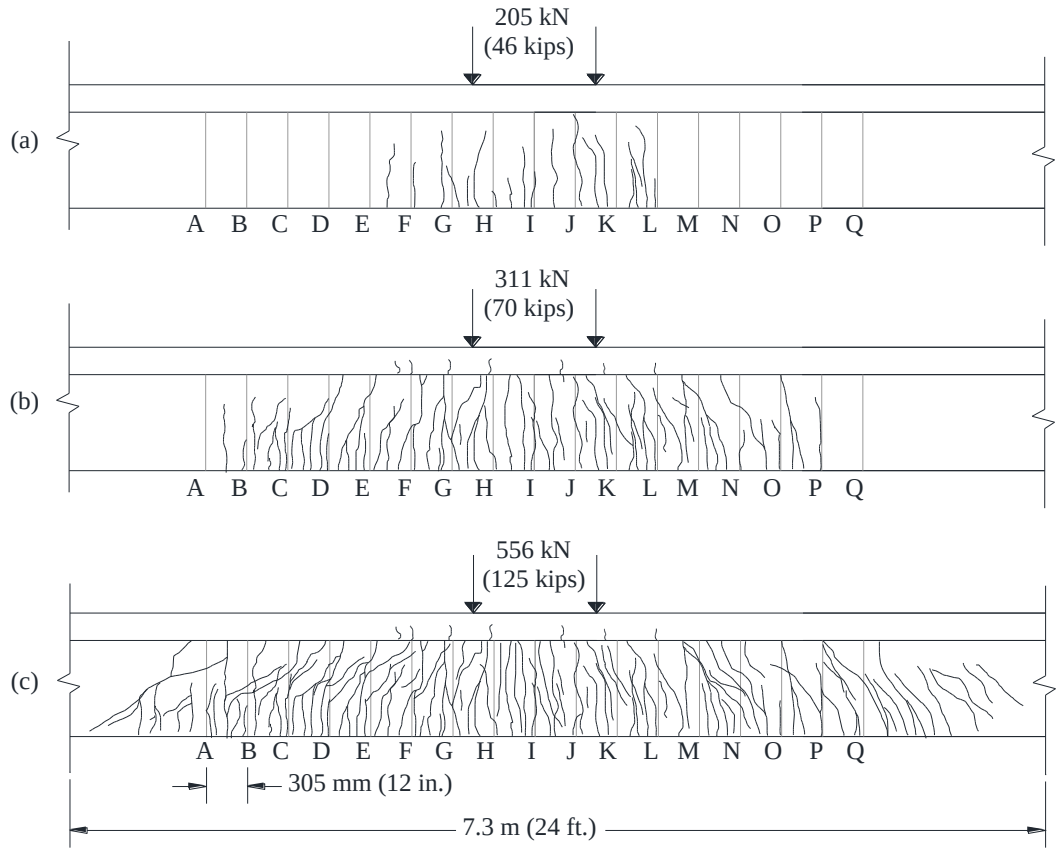

Figure 5-3. Crack Pattern at Different Load Levels: (a) Cracking, (b) Post-cracking, and (c) Prior to Failure.

Figure 5-4. Tendon Rupture at the Bottom Flange as the Failure Mode.

5.2.3 Strain Measurement

During the test, strain was measured at different locations over the height of the section, including at the top fiber of the section, at the bottom of the girder, and at the top of the girder underneath the deck. By knowing the strain at the top and bottom fibers of the section, curvature could be computed assuming the plane section remained plane after bending. The strains were measured using LVDTs distributed within and beyond the constant moment region. Figure 2-8 shows the layout of the LVDTs with a gage length of 609.6 mm (24 in.). The strain can be measured if the output of the LVDT is divided by the gage length.

Figure 5-5 presents the strain at different locations over the height of the section. As shown by LVDTs #1 and #2, which were located on the top of the deck (Figure 2-7) the maximum compressive strain was equal to 0.002 verifying that the girder did not reach the compressive strain corresponding to concrete crushing failure (0.003). The maximum tensile strain at the bottom flange of the girder (LVDTs #6, #7, #8, #9 and #10) were greater than that of the strain available for flexure of the AFRP equal to 0.0125, further confirming that the experimental specimen failed due to FRP rupture. Somewhat unexpectedly, the greatest strains were observed LVDTs #7 and #9 which just outside the constant moment region. This can be explained by recalling that outside the constant moment region, showed significant diagonal flexure-shear cracking. These cracks allowed the strain outside the constant moment region to exceed the strain inside the constant moment region.

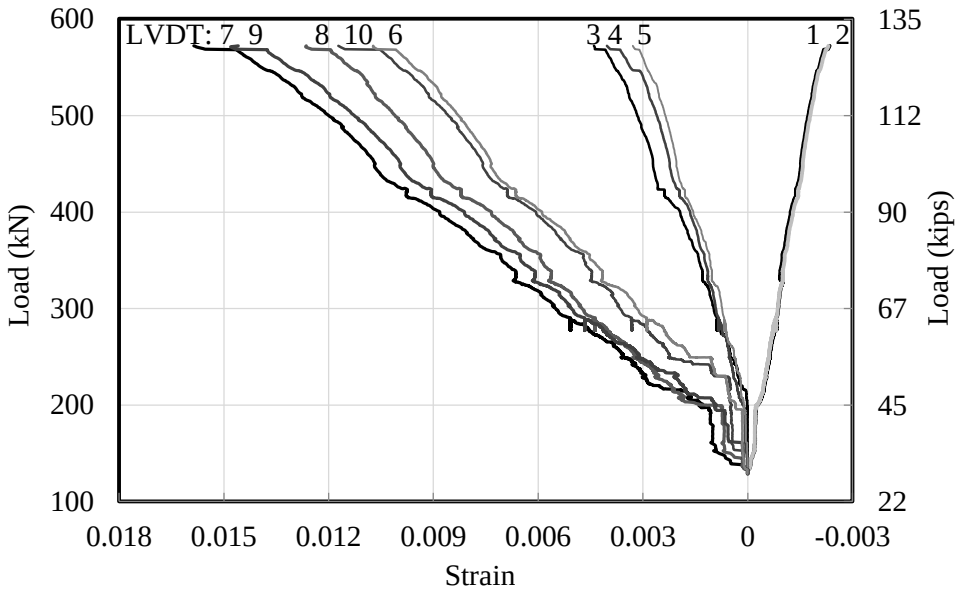

Figure 5-5. Strain at Different Locations over the Height of the Section. (Pirayeh Gar et al. 2014)

5.2.4 Deflection Profile and Curvature Distribution

To better understand the flexural response of the AFRP prestressed girder, the experimental and analytical deflection profile and curvature distribution are studied here. The experimental deflections were recorded through the string pots, as discussed in Chapter 2. The experimental curvatures were calculated based on the experimental deflections using the finite difference method. Knowing the curvature distribution provides insight into the deflection calculations, where the serviceability requirements need to be satisfied.

Figure 5-6 and Figure 5-7 present the deflection profile and curvature distribution graphs for two different post-cracking load levels. The experimental and analytical results are in good agreement and show small negative curvatures close to the end supports. Further investigation revealed that these negative curvatures are due to a small amount of friction at the end supports between the concrete girders and rubber pads. This friction was accounted for in the numerical analysis conducted by Pirayeh Gar et al. (2014).

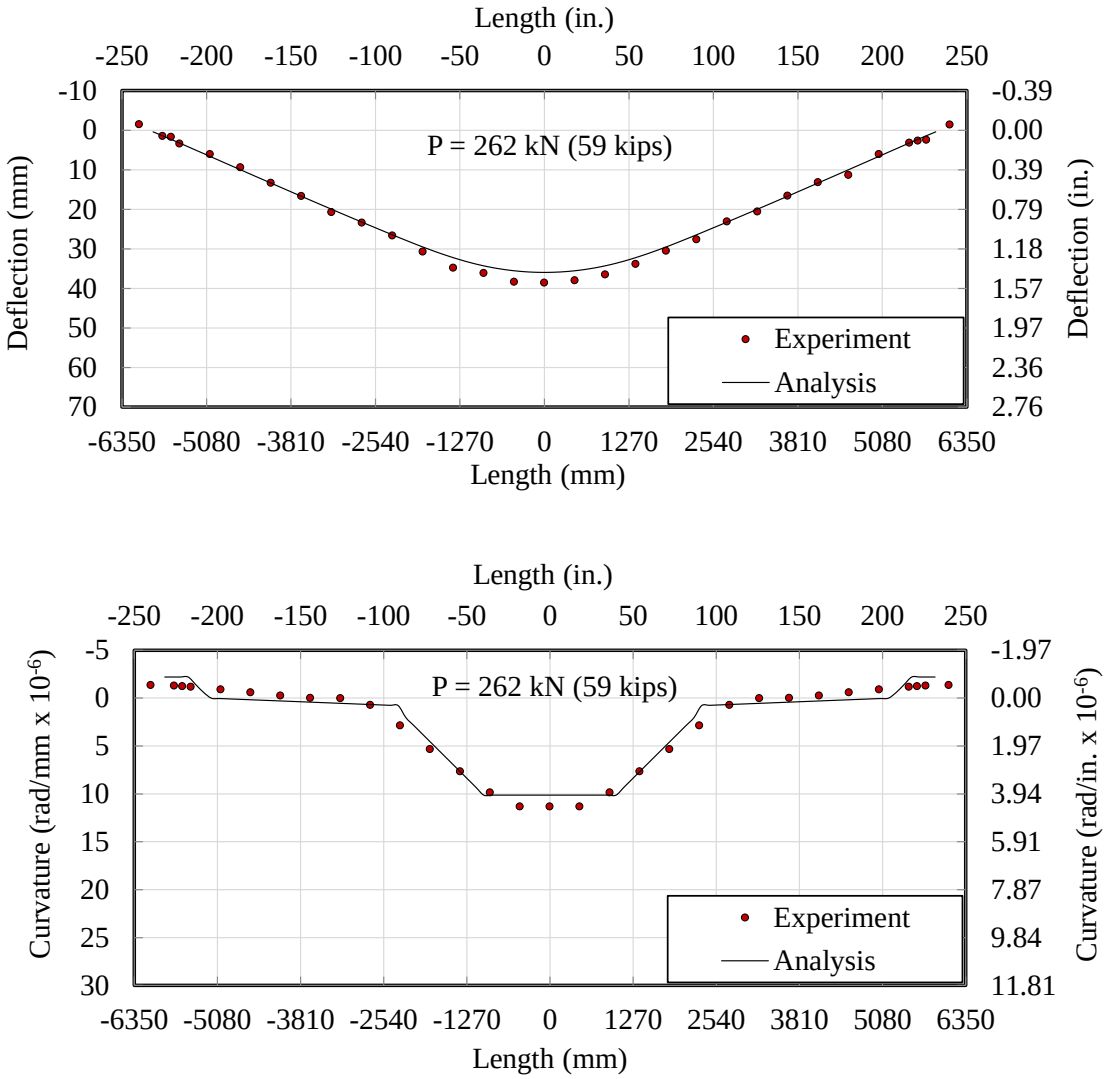

Figure 5-6. Deflection Profile and Curvature Distribution along the Girder P = 262 kN (59 kips). (Pirayeh Gar et al. 2014)

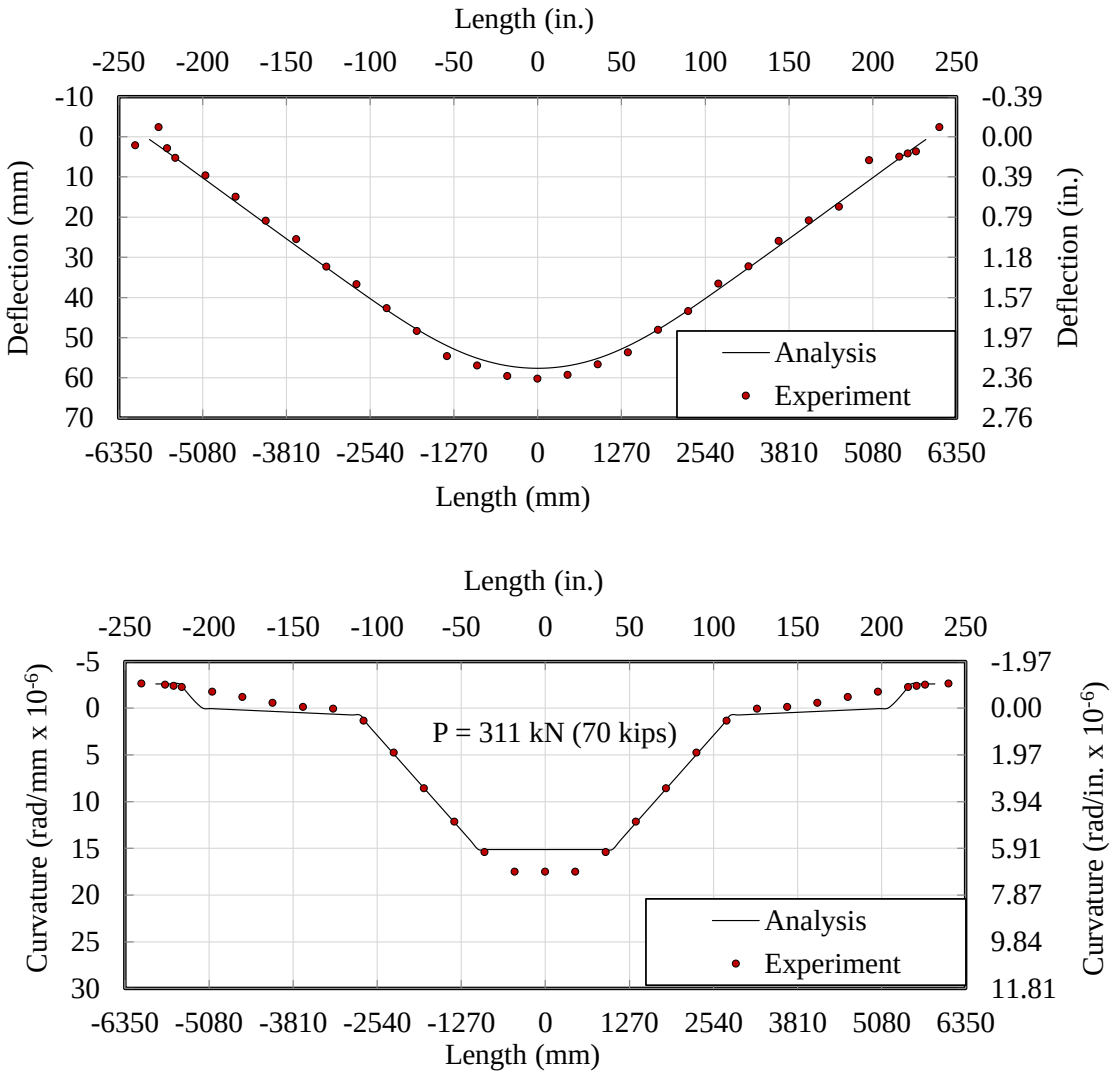

Figure 5-7. Deflection Profile and Curvature Distribution along the Girder P = 311 kN (70 kips). (Pirayeh Gar et al. 2014)

The diagonal flexure-shear discussed earlier were also accounted for in the adjustment of the constant moment region and calculation of the curvatures. As shown in Figure 5-7 the numerical analysis conducted by Pirayeh Gar et al. (2014) showed good agreement with the experimental specimen but underestimated the deflection by about 6 percent. This error can be explained by the fact that the numerical analysis assumed a perfect bond between the AFRP bars and concrete which was not true in the experiment.

5.2.5 Comparison with Control Specimen

Figure 5-8 shows the comparative moment-curvature graph between the AFRP and control specimen. As shown the control specimen shows a much greater cracking moment than the AFRP specimen. This can be attributed to the fact that the control specimen features a much greater overall prestressing force. Despite the variance in cracking moment, the ultimate moment capacities were very similar between the control specimen and the AFRP specimen, with both exceeding the maximum factored AASHTO load of M_u = 1326 kNm (978 kft.), by about 18 percent. The failure mode, however, was very different between the control and AFRP specimens. The AFRP specimen failed due to rupture of the AFRP bars in the bottom flange, while the control specimen failed due to concrete crushing (Trejo et al. 2008).

Although the AFRP specimen showed a more ductile post-cracking response, when compared to the control specimen, the ultimate curvatures between the two specimens were also very similar. This proves that substituting AFRP for conventional steel will yield very similar performance at the ultimate state, while the AFRP specimen will show more ductility and greater warning of impending failure due to extreme flexure cracking.

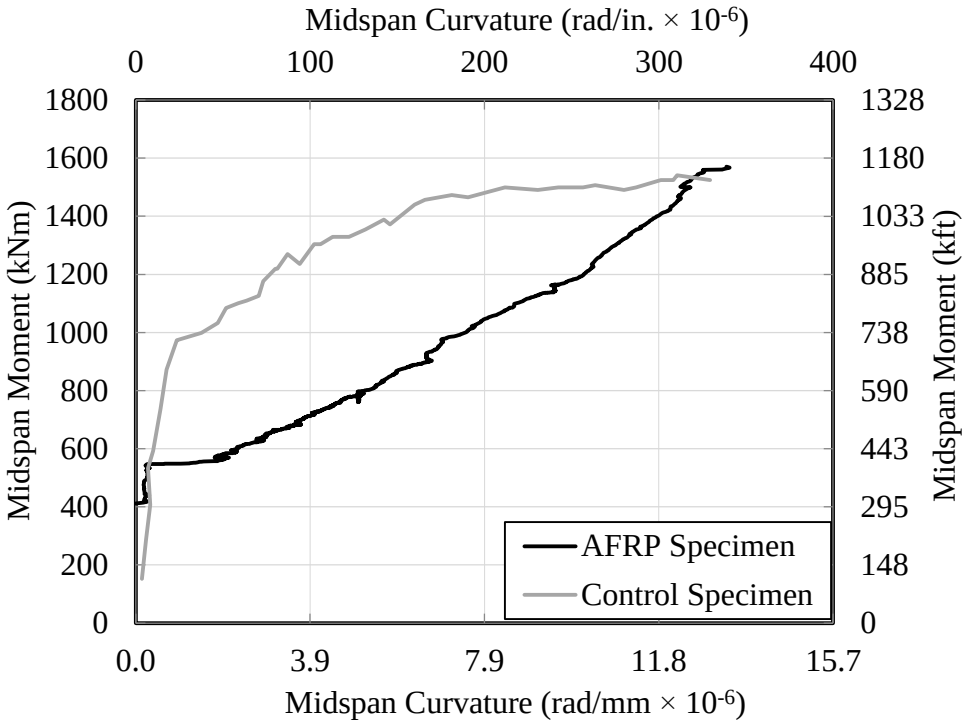

Figure 5-8. Comparative Moment-Curvature Graphs for AFRP and Control Specimens. (Pirayeh Gar et al. 2014)

Figure 5-9 presents the comparative load-deflection graphs of the AFRP and control specimens. As discussed, the control specimen showed a greater cracking load due to a greater prestressing force. Despite the difference however, the load and deflection capacities were very similar. Also the lower elastic modulus of the AFRP bar compared to the conventional steel strand caused the post-cracking flexural stiffness to decrease. However, as discussed the AFRP specimen satisfied the deflection-based serviceability limit per the AASHTO LRFD *Bridge Design Specification* (2010).

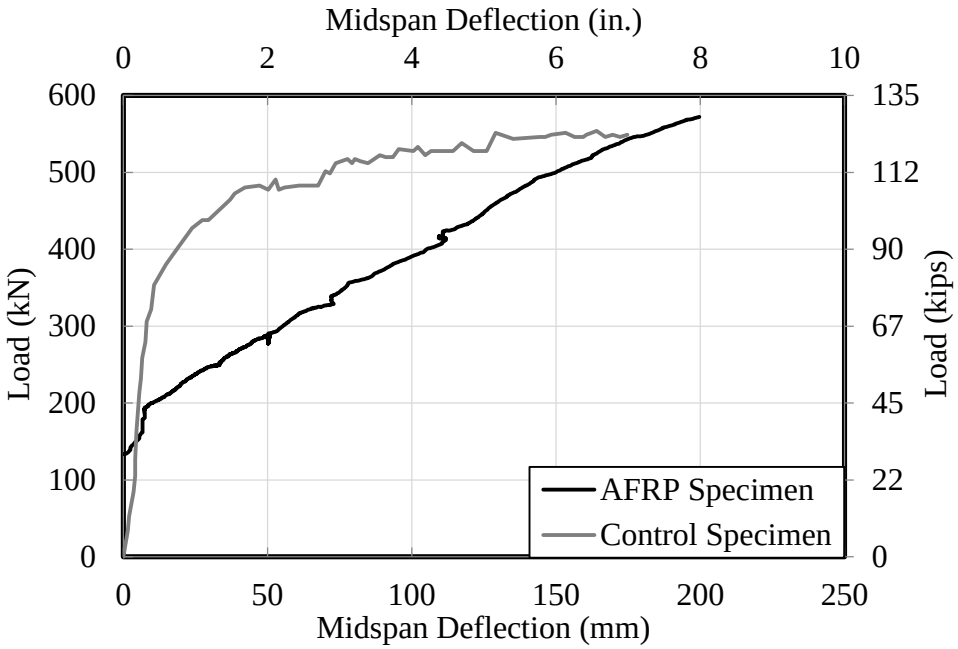

Figure 5-9. Comparative Load-Deflection Graphs for AFRP and Control Specimens. (Pirayeh Gar et al. 2014)

Figure 5-10 shows the comparative flexural crack pattern for both AFRP and control specimens. As shown, the AFRP specimen shows significantly greater cracking when compared to the control specimen at the same load. Also it is important to note that there are a greater number of flexure-shear cracks in the AFRP specimen. These cracks are an obvious sign of impending failure to the design engineer.

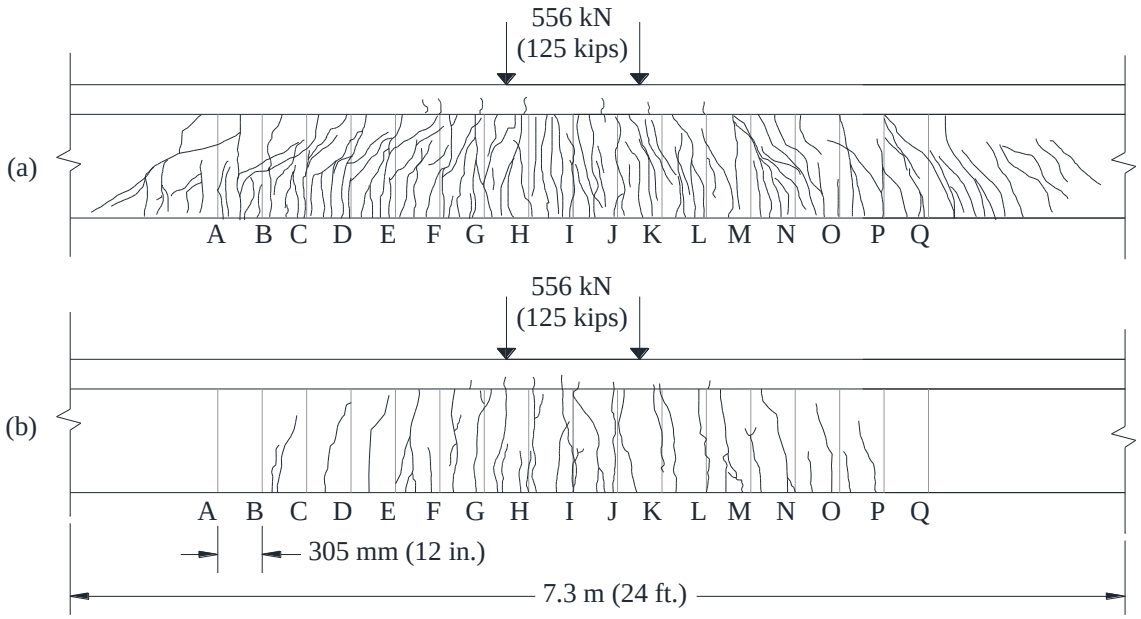

Figure 5-10. Comparative Crack Pattern under Flexure Test: (a) AFRP Specimen and (b) Control Specimen.

5.3 Shear Test

As explained in Chapter 2, two shear tests were conducted at the uncracked ends of the AFRP specimen. In shear test 1, the concentrated load was located 1.78 m (70 in.) away from the right end support of the girder. Eight LVDTs were mounted on both sides of the girder's web, four on each side, where the center of the LVDTs was located 813 mm (32 in.) away from the support. The LVDTs were mounted to measure the strain at the girder's web in *x*, *y*, and two diagonal directions, each with a 45° inclination angle. The second shear test was similarly conducted; however, the concentrated load and the center of the LVDTs were respectively located 1.5 m (60 in.) and 686 mm (27 in.) away from the left end support of the girder.

5.3.1 Shear Load Capacity

Figure 5-11 presents the location of LVDTs on the girder's web to measure tensile and compressive strains. The load was monotonically increased at a rate of 44.5 kN/min. (10 kips/min.) until shear failure occurred. In the first shear test, the specimen failed at a load of 1149 kN (258 kips) due to concrete crushing of the web. This failure could have been

somewhat premature due to the fact that the cracks from the flexure test, extended to the support. However, the cracks from the flexure test were not a factor in the second shear test due to the combination of the flexure cracks not reaching the support and the concentrated load being closer to the support. The second shear test failed at a load of 1218 kN (274 kips). The cracking loads of the first and second shear tests were 900 kN (202 kips) and 934 kN (210 kips), which were very similar. Both tests exceed the maximum factored AASHTO shear load of V_u = 566 kN (127 kips) by a factor of 2 (Pirayeh Gar et al. 2014).

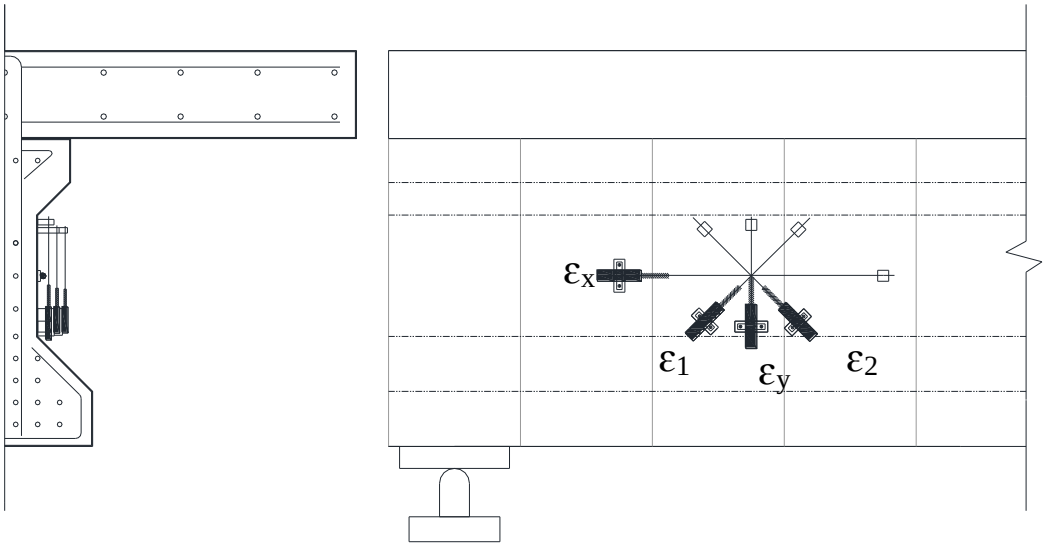

Figure 5-11. LVDT Layout.

5.3.2 Crack Pattern and Strain Measurement

Figure 5-12 shows the crack pattern for both shear tests at different load levels prior to failure. Greater load capacity was observed in the second shear test because the concentrated load was closer to the support, and the arch action was fully developed. This was implied by the crack pattern where more disturbed regions with lesser crack spacing, compared to shear test 1, were observed between the load and support.

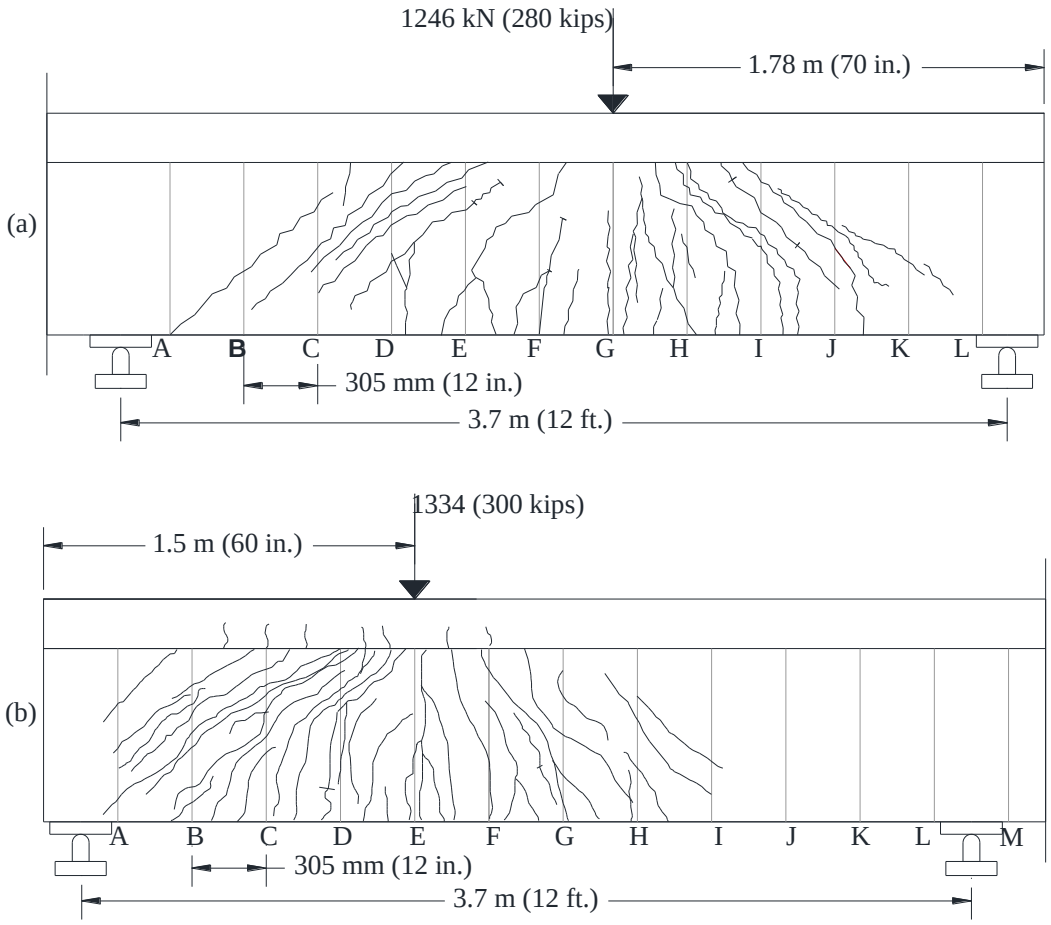

Figure 5-12. Crack Pattern under Shear Tests: (a) Shear Test 1 and (b) Shear Test 2.

The tensile and compressive strains in *x*, *y*, and diagonal directions were respectively ε_x = +0.0013, ε_y = +0.0021, ε_1 = +0.0019, and ε_2 = −0.0002 for shear test 1. For the second shear test, considerably greater values of strains were measured due to complete shear failure of the girder: ε_x = +0.0068, ε_y = +0.0089, ε_1 = +0.0116, and ε_2 = −0.0004.

5.3.3 Comparison with Control Specimen

The control and AFRP specimens were tested in a similar manner (Trejo et al. 2008), and both specimens failed due to the crushing of the girder's web. The control specimen showed a higher failure load of 1290 kN (290 kips), which was 3 percent greater than the AFRP specimen. The shear behavior of both specimens were similar due to the fact that the shear

performance is strongly dependent on the concrete compressive strength and the geometric properties of the section. The crack patterns corresponding to the AFRP specimen and control specimen are displayed in Figure 5-13. As shown both specimens had very similar cracking patterns as well.

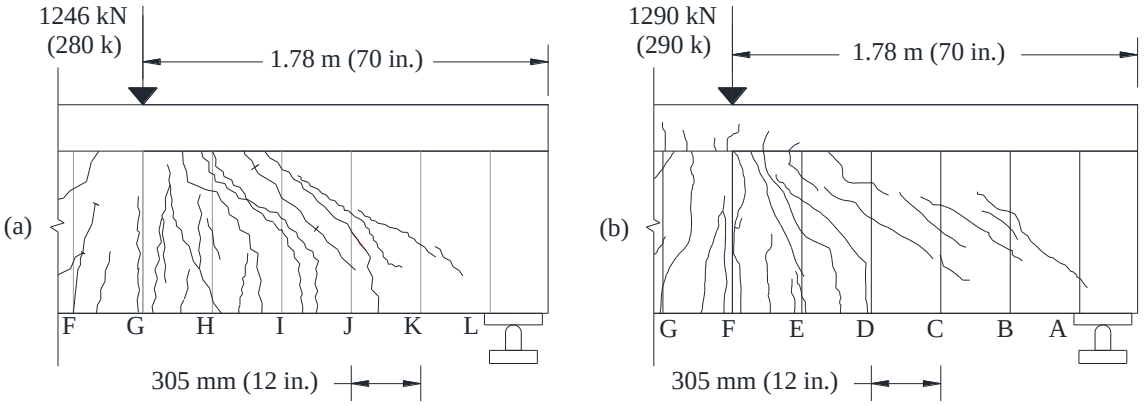

Figure 5-13. Crack Patterns under Shear Tests: (a) AFRP Specimen and (b) Control Specimen.

6 ANALYTICAL PROGRAM

6.1 Introduction

The analytical program of this research was basically divided into three different tasks: creation, verification, and implementation. An analytical program was created to reliably evaluate changes in prestressing layout. This chapter includes the assumptions, theories, and equations used to create the analytical program. Once the program was created, it was verified with multiple research examples. The program was then used throughout the analytical study.

6.2 Prestressed Concrete Design

The analytical program was designed based on the basic principles used in prestressed concrete design. Prestressed concrete is typically designed for serviceability limit states and then checked for ultimate limit states. Therefore, the available compressive stress due to prestressing at the bottom of the girder is a critical design parameter that helps resist and close flexural cracks under service loads. However, in partially prestressed girders, minor flexural cracks under service loads might be permitted.

6.2.1 Assumptions

A few important assumptions were made in the formation of the analytical program. FRP reinforced and prestressed sections can fail due to FRP rupture or concrete crushing. When the section was assumed to fail by FRP rupture, failure was assumed to be governed by the rupture of only one layer of FRP bars. When a layer of FRP ruptures, the stress in that layer is distributed to the remaining layers. Due to the congestion of the bars, when one layer of FRP ruptures, the remaining layers will rupture soon after. The neutral axis was assumed to remain in the topping deck, allowing the section to be analyzed as a rectangular section. A prestressing loss of ten percent was also assumed in the calculation of the cracking moment and available compressive stress.

6.2.2 Cracking Moment

The cracking moment consists of two terms; rupture stress of the concrete, and stress due to prestressing of the FRP bars. The rupture stress of the concrete is equal to

$$f_r = 7.5\sqrt{f_c'}\,, \tag{6-1}$$

where f_r and f'_c respectfully is the rupture stress of the concrete and the compressive strength of the concrete in units of psi. The compressive stress due to the prestressing of the FRP bars can be calculated as

$$f_{bp} = \frac{P}{A} + \frac{Pe}{S_b}\,. \tag{6-2}$$

It is important to note that a ten percent reduction due to prestressing losses was accounted for in the calculation of the prestressing force, *P*. The dead and live service loads acting on the girder were not accounted for in the cracking moment calculation in order to compare the total cracking moment to the applied moment due to service loads. Combining these stresses and multiplying by the composite section modulus will yield the cracking moment

$$M_{cr} = \left[7.5\sqrt{f_c'} + \left(\frac{P}{A} + \frac{Pe}{S_b}\right)\right] S_{bc}\,. \tag{6-3}$$

The cracking curvature is then derived from the elastic flexure formula

$$f = \frac{My_b}{I_g}\,, \tag{6-4}$$

where y_b is the distance from the bottom fiber of the girder to the neutral axis, and I_g is the moment of inertia of the gross section. Using Hooke's law, $f = E\varepsilon$, and the elastic flexure formula gives cracking strain at the bottom fiber of the girder equal to

$$\varepsilon_{cr} = \frac{M_{cr} y_b}{I_g E_c}\,. \tag{6-5}$$

The cracking curvature is simply calculated as the cracking strain divided by the distance from the bottom fiber of the girder to the neutral axis

$$\Psi_{cr} = \frac{M_{cr} y_b}{I_g E_c y_b} = \frac{M_{cr}}{I_g E_c}\,. \tag{6-6}$$

6.2.3 Ultimate Moment

The behavior of the section at the ultimate limit was designed based on basic force equilibrium and strain compatibility equations. In order to calculate the flexural strength of the section, the failure mode and concrete behavior must be known. FRP reinforced and prestressed sections can fail due to FRP rupture or concrete crushing, and the concrete can behave either elastically or inelastically depending on the flexural strain profile. Figure 6-1 displays the general solution to a cracked prestressed concrete section reinforced and prestressed with linear elastic FRP tendons. As shown, the real concrete stresses are approximated using an equivalent rectangular stress block that results in the magnitude and location of the compressive force, *C*, to remain unchanged (Karthik and Mander 2011).

There are three cases (E, C, and T) that need to be considered when determining the compressive stress behavior and ultimate moment of the section. In Case E, all material behaves elastically until tendon rupture failure. In Case C, the section fails due to concrete crushing and the concrete behaves inelastically, and Case T is the transition between Cases E and C.

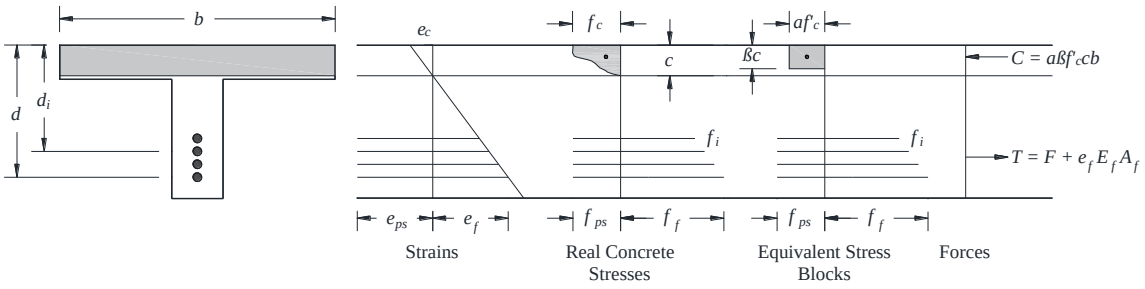

Figure 6-1. General Solution for a Cracked Prestressed Concrete Section with Linear Elastic Tendons.

6.2.3.1 *Case E: All Materials Remain Elastic*

In the first case, it is assumed that the section fails due to FRP rupture and the concrete remains essentially elastic. Unconfined concrete begins to behave inelastically when the compressive strain exceeds 0.001 (Karthik and Mander 2011). Conversely, essentially elastic behavior may be presumed providing the concrete strain does not exceed 0.001, that is $f_c \le f_c^{'}$. If the concrete remains elastic, the compressive stress block acting on the section can be assumed to be linear. The concrete compressive force generated by the triangular stress block is

$$C = \frac{1}{2} f_c bc \,, \tag{6-7}$$

where f_c is the compressive stress at the top fiber, *c* is the location of the neutral axis of the flexural strain distribution, and *b* is the width of the section. However, for the general case using the Karthik and Mander (2011) stress blocks as shown in Figure 6-1, the concrete compressive force is equal to

$$C = \alpha\beta f_c^{'} bc \,. \tag{6-8}$$

Thus, for the elastic case, $\alpha = 0.75$ and $\beta = 0.67$.

6.2.3.2 *Case C: Concrete Compression Failure*

Case C assumes that the section fails due to concrete crushing, causing the concrete to behave fully inelastically. A prestressed and reinforced concrete section fails due to concrete crushing when the compressive strain at the top fiber of the section reaches its ultimate limit of 0.003 before the tendons rupture. The concrete compressive stress is significantly non-linear at its ultimate state so the well-known Whitney's stress block may be used, where in Equation 6-8, $\alpha = 0.85$, and β is dependent on the concrete compressive strength as follows:

$$\beta = \begin{cases} 0.85 & f_c^{'} \le 4ksi \\ 1.05 - 0.05 f_c^{'}(ksi) & 4ksi \le f_c^{'} \le 8ksi \\ 0.65 & f_c^{'} \ge 8ksi \end{cases}. \tag{6-9}$$

6.2.3.3 *Case T: Tension Failure: A Transition between Cases E and C*

In the transition case, it is assumed that the section fails due to FRP rupture, but the concrete behaves partially inelastically, that is the compressive strain is between 0.001 and 0.003. It follows from cases E and C above that β will typically be in the range of 0.67 but not more than 0.85 for weak concrete, and α ranges from 0.75 to 0.85. The equivalent stress block parameters α and β for any level of specified maximum compressive strain can be found elsewhere (Karthik and Mander 2011).

In any case, the vertically distributed layers of FRP bars in a prestressed concrete section can either be analyzed separately or as a single equivalent layer acting at an equivalent eccentricity. Given that FRP sections with large compressive regions tend to fail due to FRP rupture instead of concrete crushing (Abdelrahman et al. 1995), analyzing each layer individually allows for a more accurate representation of failure. This is especially true for a section with many vertically distributed layers, as the centroid of the prestressed tendons could be very far from the layer that ruptures and causes failure.

Therefore, each vertical layer was analyzed separately using a method developed by Dolan and Swanson (2001) for determining the strength of a section with vertically distributed tendons. This method is based on a cracked section with a stress-strain distribution similar to that shown in Figure 6-1. All bars were assumed to be stressed to the same level, f_{ps}. The neutral axis of the flexural strain distribution was assumed to be in the flange of the T-section. The concrete compressive force can be calculated corresponding to the cases mentioned previously.

The total tensile force can be determined by summing the tensile forces in each layer

$$T = \sum_{i=1}^{m} \rho_i b d f_i \,, \tag{6-10}$$

where ρ_i and f_i are the reinforcement ratio and FRP tendon stress at layer i. The reinforcement ratio at each layer can be defined as $\rho_i = A_i / bd$, where A_i is the area of the reinforcement at layer i. Since FRP is linearly elastic, the stress. f_i, in each layer of FRP tendons can be determined as

$$f_i = E_f \varepsilon_{t,i}, \tag{6-11}$$

where E_f and $\varepsilon_{t,i}$ are the modulus of elasticity and total strain in layer *i*, respectively. The total strain can be simplified as the sum of initial and flexural strain in the layer, $\varepsilon_t = \varepsilon_{ps} + \varepsilon_f$. Combining Equations 6-10 and 6-11 gives

$$T = bdE_f \sum_{i=1}^{m} \left[\rho_i \left(\varepsilon_{ps} + \varepsilon_f \right) \right]. \tag{6-12}$$

In order to satisfy equilibrium, the tensile force is equated to the compressive force, and can then be solved for *c*, allowing flexural strain distribution to be fully defined.

If the section belongs to Cases E or T, the flexural strain distribution for the section can be calculated by first assuming which layer of prestressed tendons ruptures. The rupture layer is verified by checking the strains at all levels to ensure that only the rupture layer has reached its ultimate strain. Since the strain distribution is linear throughout the height of the section, the total strain in each layer can be determined as

$$\varepsilon_{t,i} = \varepsilon_{ps,i} + \frac{\varepsilon_{fd} \left(d_i - c \right)}{d - c}, \tag{6-13}$$

where d_i and *d* are the depth of layer *i* and the depth of the rupture layer, respectively. $\varepsilon_{ps,i}$ and ε_{fd} are the initial strain in layer *i* and the strain due to flexure of the rupture layer, respectively.

If the section belongs to Case C the compressive strain at the top fiber is known, and the total strain in each layer is

$$\varepsilon_{t,i} = \varepsilon_{ps,i} + \frac{\varepsilon_{cu} \left(d_i - c \right)}{c}, \tag{6-14}$$

where $\varepsilon_{cu} = 0.003$ is the ultimate compressive strain of the concrete.

Once the stress-strain distribution of the section is determined, the nominal moment can be calculated as

$$M_n = \sum_{i=1}^{m} T_i \left(d_i - \frac{\beta c}{2} \right), \tag{6-15}$$

where *m* is the total number of layers in the section.

For Cases E or T, the ultimate curvature can be determined from the flexural strain profile as

$$\Psi_n = \frac{\varepsilon_{fd}}{d - c}, \tag{6-16}$$

whereas for Case C, the ultimate curvature is

$$\Psi_n = \frac{\varepsilon_{cu}}{c}. \tag{6-17}$$

6.3 Validation of the Analytical Program

The analytical program was validated using five specimens tested by Nanni (2000). This particular research was chosen because it included simple cross-sections, FRP reinforcement, and a mixture of fully and partially prestressed sections. All specimens featured a rectangular section with a width of 152.4 mm (6 in.), and heights varying between 228.6 and 304.8 mm (9 and 12 in.). The reinforcement layout for each section is shown in Figure 6-2. As shown, each section's designation consisted of three parts: the height (9 or 12 inches), the amount of reinforcement (2 or 4 bars), and fully or partially prestressed (F or P). For example, section B9-4F features a 228.6 mm (9 in.) height with four fully prestressed FRP bars.

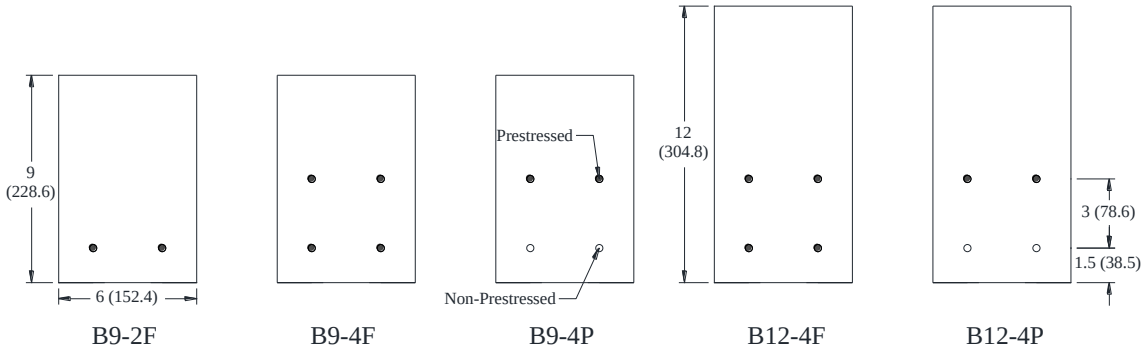

Figure 6-2. Reinforcement Layout (Nanni 2000)

FRP reinforcement known as Strawman tendons, with 7.94 mm (0.31 in.) diameter, were stressed to 60 percent of the tendon's ultimate stress. Strawman tendons had a tested average modulus of elasticity, tensile strength, and tensile elongation, of 153.3 GPa (22240 ksi), 1.86 GPa (270 ksi), and 1.2 %, respectively. All five specimens were tested as simply supported beams, under four point bending, with a total span of 5.5 m (18 ft.). The ultimate moment and curvature of each specimen tested by Nanni is presented in Table 6-1. As seen, the error in the ultimate moment is less than twelve percent for all specimens which ensures that the results of the study are valid.

Table 6-1. Experimental and Theoretical Results (Nanni 2000)

	Specimen	B9-2F	B9-4F	B9-4P	B12-4F	B12-4P
Ultimate Moment, kNm (kin.)	Experimental	28.9 (256)	40.2 (356)	35.1 (311)	78.9 (698)	57.9 (512)
	Theoretical	32.9 (291)	43.7 (387)	39.2 (347)	70.5 (624)	60.1 (532)
	Percentage (%)	88	92	89.6	112	96.2
Ultimate Curvature, rad/mm×10^6 (rad/in.×10^6)	Experimental	32.3 (821)	31.8 (808)	41.3 (1048)	25.1 (637)	26.0 (660)
	Theoretical	34.3 (870)	39.4 (1000)	59.0 (1498)	24.7 (628)	35.5 (902)
	Percentage (%)	94.4	80.8	70	101.4	73.2

The theoretical results from the study conducted by Nanni (2000) were used to validate the analytical program. The compared results are presented in Table 6-2. As shown, there is significant error for the B9-4P specimen. This specimen was the only specimen that was assumed to fail due to concrete crushing (Nanni 2000). If the section fails due to concrete compression, the top fiber of the concrete reaches a strain of 0.003, and the compressive stress is significantly nonlinear. This specimen shows the greatest error at the ultimate state; however, comparing the results of this specimen to the experiment conducted by Nanni (2000) shows that the error is only five percent. All other specimens have an error of less than seventeen percent. The ultimate curvature showed similar results with every specimen having an error of less than eight percent. These results prove that the analytical program can be considered valid.

Table 6-2. Specimen Comparison

Specimen		B9-2F	B9-4F	B9-4P	B12-4F	B12-4P
Cracking Moment, kNm (kin.)	Nanni	20.0 (177)	22.9 (203)	12.0 (106)	41.9 (371)	20.5 (181)
	Present Study	18.4 (163)	21.7 (192)	10.4 (92)	36.2 (320)	20.8 (184)
	Error (%)	-7.6	-5.6	-13.5	-13.7	+1.4
Cracking Curvature, rad/mm×10^{-6} (rad/in.×10^{-6})	Nanni	4.2 (106)	4.6 (118)	2.8 (72)	3.9 (100)	1.9 (48)
	Present Study	3.7 (93)	4.6 (118)	1.9 (49)	3.3 (84)	1.7 (42)
	Error (%)	-12.6	-0.3	-31.5	-16.4	-13.2
Ultimate Moment, kNm (kin.)	Nanni	32.9 (291)	43.7 (387)	39.2 (347)	70.5 (624)	60.1 (532)
	Present Study	31.6 (280)	39.5 (350)	33.4 (296)	69.3 (613)	59.7 (528)
	Error (%)	-3.9	-10.6	-17.2	-1.7	-0.8
Ultimate Curvature, rad/mm×10^{-6} (rad/in.×10^{-6})	Nanni	34.3 (870)	39.4 (1000)	59.0 (1498)	24.7 (628)	35.5 (902)
	Present Study	34.3 (871)	39.8 (1011)	53.0 (1345)	26.6 (676)	35.6 (903)
	Error (%)	+0.1	+1.1	-11.4	+7.7	+0.1

Specimen B12-4F was used to further verify the analytical program. Nanni varied the prestressing level from 0 to 70 percent for all four prestressed bars. The ultimate moment and curvature were reported and the comparison of the results are displayed in Table 6-3. As shown, the errors in moment and curvature at the ultimate state are less than ten percent for all cases. This conclusion further verifies the program is accurate.

Table 6-3. Comparison of Specimen B12-4F

Prestressing Level (%)		0	10	20	30	40	50	60	70
Ultimate Moment, kNm (kin.)	Nanni	60.8 (538)	63.5 (562)	66.4 (588)	69.6 (616)	70.3 (622)	70.7 (626)	71.4 (632)	71.4 (632)
	Present Study	66.3 (587)	67.0 (593)	67.7 (599)	68.2 (604)	68.8 (609)	69.2 (612)	69.4 (614)	69.2 (612)
	Error (%)	+9.2	+5.5	+1.9	-1.9	-2.1	-2.2	-2.8	-3.2
Ultimate Curvature, rad/mm×10^{-6} (rad/in.×10^{-6})	Nanni	52.8 (1341)	50.0 (1270)	47.0 (1194)	43.6 (1107)	37.7 (957)	31.7 (806)	24.7 (626)	19.7 (499)
	Present Study	54.9 (1395)	50.1 (1272)	45.1 (1147)	40.2 (1022)	35.2 (895)	30.2 (767)	25.1 (637)	19.8 (504)
	Error (%)	+4.0	+0.2	-3.9	-7.7	-6.5	-4.8	+1.8	+1.0

The program was further investigated for accuracy by comparing with a fiber element analysis (Pirayeh Gar et al. 2014) and the experimental results discussed in Chapter 5 of the AASHTO I-girder Type I. The girder had dimensions and reinforcement layout similar to that shown in Figure 2-1. The fiber element analysis investigated only the bottom 20 prestressed tendons. The AFRP bars had theoretical modulus of elasticity, strain capacity, and tensile strength of 69.0 GPa (10000 ksi), 0.02, and 1.4 GPa (200 ksi), respectively. The average prestressing ratio of the AFRP bars in the experimental investigation was equal to 43 percent. The comparative results are given in Table 6-4. The errors between the fiber element analysis and the analytical program are less than five percent at both the cracking and ultimate states. These results further prove that the program is valid.

Table 6-4. Comparison of Controlling Specimen

	Cracking		Ultimate	
	Curvature, rad/mm×10^{-6} (rad/in.×10^{-6})	Moment, kNm (kft.)	Curvature, rad/mm×10^{-6} (rad/in.×10^{-6})	Moment, kNm (kft.)
Experimental	0.22 (5.5)	542 (400)	13.23 (336)	1563 (1153)
Fiber Element Analysis	0.35 (8.9)	529 (390)	14.6 (370)	1540 (1136)
Analytical Program	0.346 (8.8)	551 (406)	14.3 (362)	1608 (1186)

6.4 Analytical Study

The analytical study was basically divided into four different sections corresponding to the layer of prestressed AFRP bars being analyzed. The study began by varying the prestressing ratio of the first layer (bottom layer) of AFRP bars from 0 to 50 percent. The analytical program calculated the moment and curvature for the cracking and ultimate states, along with the available compressive stress at the bottom of the girder due to prestressing. This process was repeated for the first three layers.

The goal of the analytical study was to determine the effect of prestressing layout on the following characteristics:

- Cracking moment and curvature.
- Ultimate moment and curvature.
- Available compressive stress due to prestressing.
- Ductility index.

These characteristics were compared to those of the controlling specimen which will be discussed later. An optimal prestressing layout was then determined which features improved ductility while satisfying the ultimate and serviceability limit states.

6.5 Conclusion

An analytical program was created to analyze changes in prestressing layout for an AASHTO I-girder Type I. The program was designed using force equilibrium and strain compatibility equations. Each layer was analyzed separately due to the fact that the prestressing ratio will vary at every layer.

The program was validated with existing research that reports the theoretical moment and curvature of FRP reinforced and prestressed sections. The comparison of the results shows that the error is within the acceptable range. Because of this low error, the program can be considered valid and will provide reliable results. The analytical program was then used to determine the optimal prestressing layout that improves the performance of the girder at the ultimate limit while still satisfying serviceability limits.

7 ANALYTICAL RESULTS

7.1 Introduction

The analytical program developed in Chapter 6 was used to accurately analyze AASHTO I-girder Type I specimens with varying levels of prestressing throughout their cross-section. Prestressed concrete is designed for serviceability limit states and then checked for ultimate limit states. Therefore the cracking moment, and tensile stress at the bottom fiber of the girder are extremely important design parameters.

The goal of the analytical program was to determine an optimal prestressing layout which improves the performance of the girder at the ultimate limit while still satisfying serviceability limits. The optimal prestressing layout to achieve maximum deformability is critical where ductility demands can be challenging for conventional steel prestressed sections. For instance, at bridge piers in seismic zones the optimal prestressing layout can compensate for the lack of deformability, when compared to the conventional steel prestressed section. Also, reducing the prestressing ratio at any layer allows for a more reliable prestressing operation with less likelihood of premature prestressing failure as discussed in Chapter 4.

All specimens analyzed in this chapter had dimensions of an AASHTO I-girder Type I shown in Figure 2-1, along with a 203.2 mm (8 in.) topping deck, and section properties presented in Table 7-1. The mechanical properties of all analytical specimens are summarized in Table 7-2.

Table 7-1. Section Properties of the Girder (Pirayeh Gar et al, 2014)

Section	A mm^2 (in.^{2})	Y_b mm (in.)	Y^t mm (in.)	I mm^4 (in.^{4})	S_b mm^3 (in.^{3})	S^t mm^3 (in.^{3})
Girder	17.81×10^4 (276)	319.78 (12.59)	391.41 (15.41)	9.47×10^9 (22,750)	29.61×10^6 (1807)	24.19×10^6 (1476)
Girder & Deck	50.83×10^4 (788)	640.08 (25.2)	274.32 (10.8)	38.73×10^9 (93,043)	60.5×10^6 (3692.18)	141.17×10^6 (8615.1)
A	cross-sectional area					
Y_b	distance from neutral axis to the bottom flange					
Y^t	distance from neutral axis to the top flange					
I	moment of inertia					
S_b	section modulus with respect to the bottom fiber of the section					
S^t	section modulus with respect to the top fiber of the section					

Table 7-2. Mechanical Properties of Analytical Specimens.

Concrete	Compressive Strength, f'_c MPa (ksi)	86.2 (12.5)
	Modulus of Elasticity, E_c GPa (ksi)	43.9 (6373)
	Crushing Strain, ε_{cu}	0.003
AFRP	Ultimate Strength, GPa (ksi)	1.4 (200)
	Modulus of Elasticity, E_p GPa (ksi)	68.9 (10000)
	Ultimate Strain, ε_{pu}	0.02

7.2 Control Specimen

The control specimen consisted of twenty-four prestressed AFRP bars within the girder section; twenty-two in the bottom flange and two in the top flange as shown in Figure 7-1. In addition, eight non-prestressed bars, six in the web, and two in the top flange, were used within the girder section. The first (bottom) layer, was 50.8 mm (2 in.) from the girder's bottom fiber. The next four layers were each spaced 50.8 mm (2 in.) vertically from the previous layer. The three layers of nonprestressed bars in the web were each spaced 76.2 mm (3 in.) vertically from the fifth layer. Finally, the top layer of prestressed and nonprestressed bars were placed 50.8 mm (2 in.) from the top fiber of the girder.

The critical design parameters investigated were the moment and curvature at the cracking and ultimate states, and the available compressive stress due to prestressing at the girder's bottom fiber. These critical design parameters for the control specimen are presented in Table 7-3.

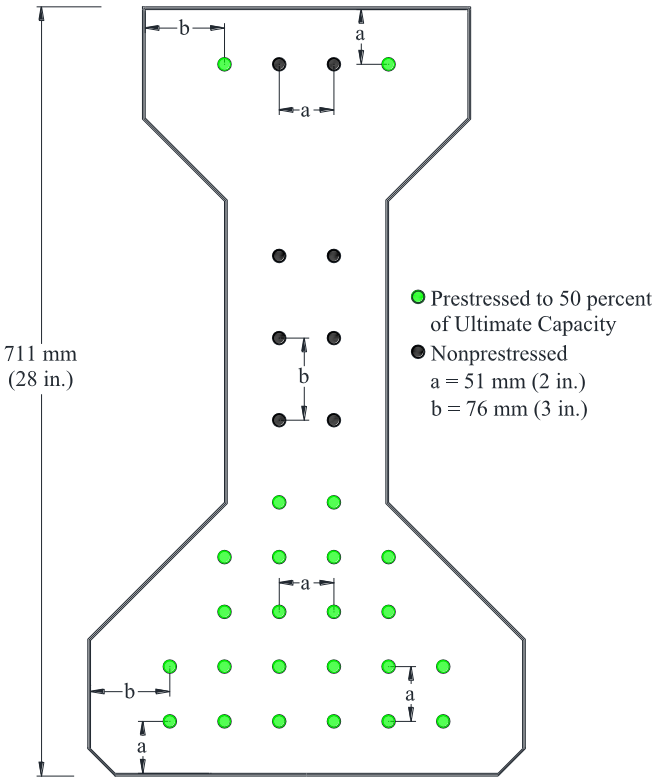

Figure 7-1. Prestressing Layout of the Control Specimen (AASHTO I-girder Type I).

Table 7-3. Critical Design Parameters for Control Specimen.

Critical Design Parameters for Control Specimen	
Cracking Moment, kNm (kft.)	1097.3 (809.3)
Cracking Curvature, rad/mm×10^{-6} (rad/in.×10^{-6})	0.646 (16.4)
Ultimate Moment, kNm (kft.)	1851.0 (1364.9)
Ultimate Curvature, rad/mm×10^{-6} (rad/in.×10^{-6})	12.7 (322.4)
Available Compressive Stress due to Prestressing, MPa (ksi)	12.4 (1.792)

7.3 First Layer Analysis

The analytical program began by varying the prestressing ratio of the first (bottom) layer of AFRP tendons while holding all else constant. The prestressing ratio was varied from 0 to 50 percent with a 5 percent incremental step. The moment-curvature relationship along with the available compressive stress at the girder's bottom fiber was recorded.

The available compressive stress is vital to the performance of the specimen as it determines whether the serviceability requirements are met. The compressive stress required by prestressing to meet serviceability requirements is equal to 12 MPa (1.74 ksi) (Pirayeh Gar et al. 2014). The available compressive stress at the bottom fiber was normalized to the required compressive stress, and is displayed in Figure 7-2. As expected, reducing the prestressing ratio results in less available compressive stress. Since the compressive stress at every level of prestressing is insufficient to meet serviceability requirements, the difference must somehow be compensated.

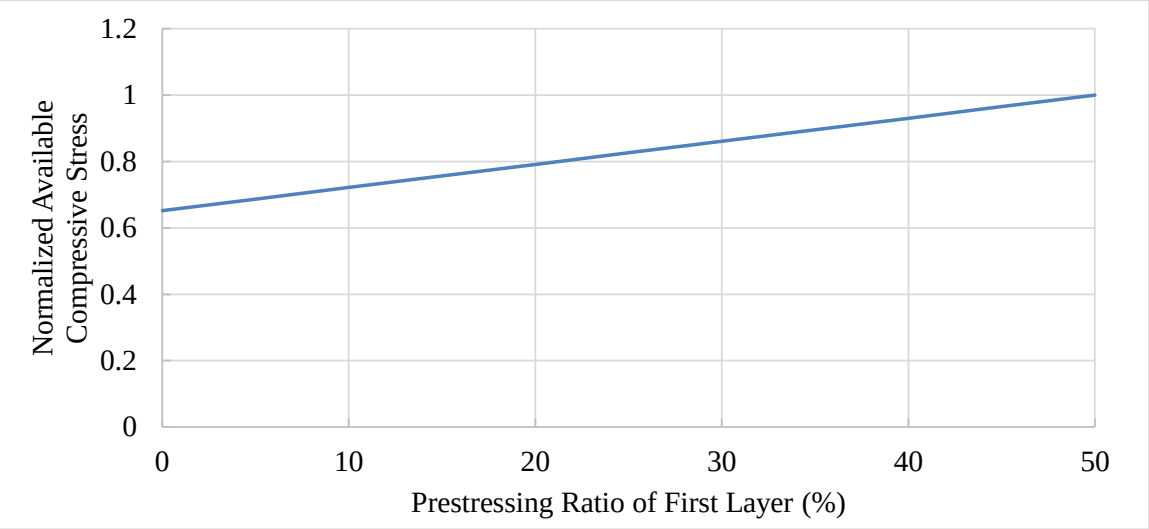

Figure 7-2. Normalized Available Compressive Stress (First Layer Analysis)

The comparison between the cracking and ultimate moment is displayed in Figure 7-3. The cracking moment is linear with varying prestressing ratio of the first layer. Recall that the cracking moment is largely dependent on the total prestressing force and the prestressing eccentricity according to Equation 6-2. In this study, the prestressing eccentricity is dependent on the total prestressing force, causing the cracking moment to be linear assuming the section geometry remains constant.

The ultimate moment shows a linear increase until a maximum of 1889 kNm (1393.5 kft.) at a first layer prestressing ratio of 45 percent, then decreases linearly to 1851 kNm (1364.9 kft.) at a first layer prestressing ratio of 50 percent. Recall from Chapter 6 that the section is assumed to fail when the tendons in any layer reaches their ultimate strain. When the prestressing ratio of the first layer is very low, say 15 percent, it is reasonable to assume that the second layer will reach its ultimate strain before the first layer. In fact, the strain in the second layer controls for all prestressing layouts except when the first layer prestressing ratio is 50 percent. This shift in controlling layer causes the sudden change in linearity seen in Figure 7-3, and the ultimate moment capacity to diminish. It can also be seen that specimens with first layer prestressing ratios of 40 and 45 percent have moment capacities that exceed the controlling specimen.

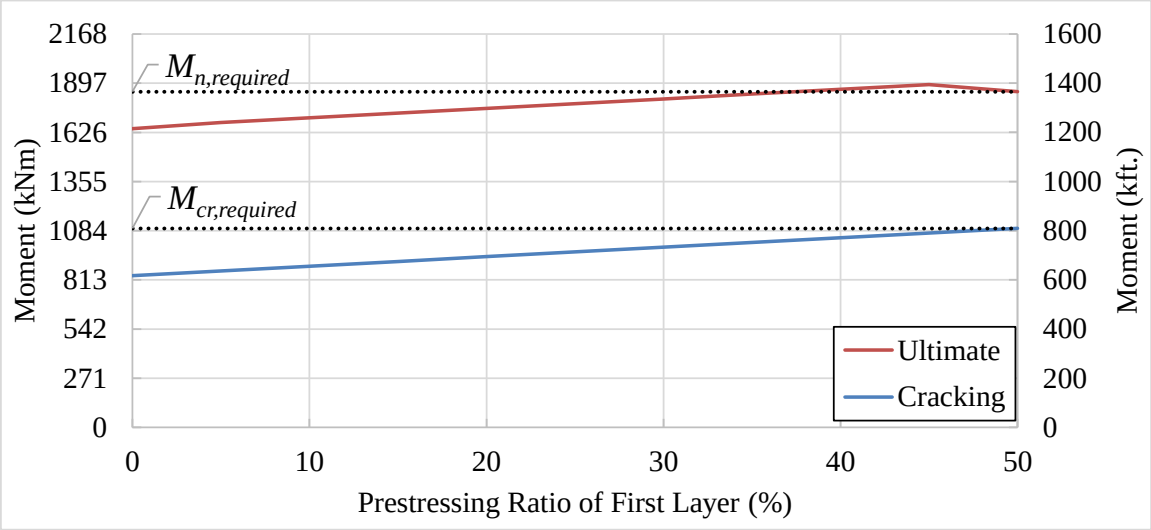

Figure 7-3. Cracking and Ultimate Moment Comparison (First Layer Analysis)

The normalized moment can be defined as the ratio of the moment at any first layer prestressing ratio, M_i, to the moment at first layer prestressing ratio of 0 percent, M_0,

$$M_{norm} = \frac{M_i}{M_0}. \tag{7-1}$$

The normalized moments for the cracking and ultimate states are presented in Figure 7-4. As discussed, the cracking moment increases linearly until it reaches its maximum of 31 percent increase compared to 0 percent prestressed first layer. The ultimate moment behaves similarly to the ultimate moment in Figure 7-3, with a maximum increase of around 15 percent compared to 0 percent prestressed first layer. However, the cracking moment is much more sensitive to the prestressing level as shown by the greater slope when compared to the ultimate moment.

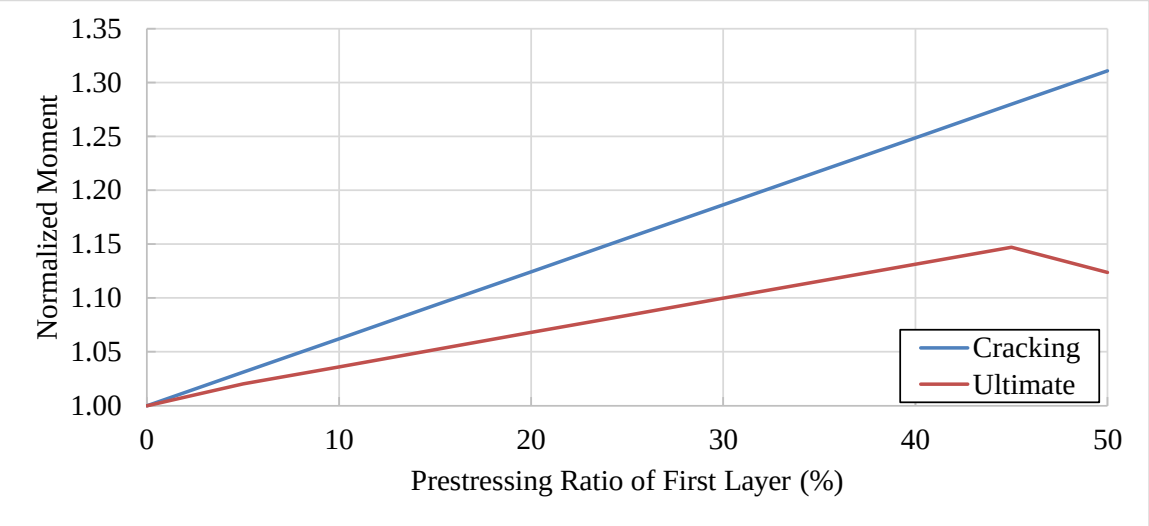

Figure 7-4. Normalized Cracking and Ultimate Moment Comparison (First Layer Analysis)

The ductility index can be defined as the ratio of the total deformation at the ultimate state to the deformation at the elastic limit,

$$\varphi_{du} = \frac{\Psi_n}{\Psi_{cr}}. \tag{7-2}$$

The ductility index for varying first layer prestressing ratios is shown in Figure 7-5. The consistently declining ductility index indicates that as the prestressing ratio of the first layer increases, the cracking and ultimate curvatures approach each other. Given that the minimum value of the ductility index occurs at the controlling specimen, it can be concluded that the ductility improves for all cases. This is an expected result since the lower prestressing ratio of the first layer allows for greater flexural strain.

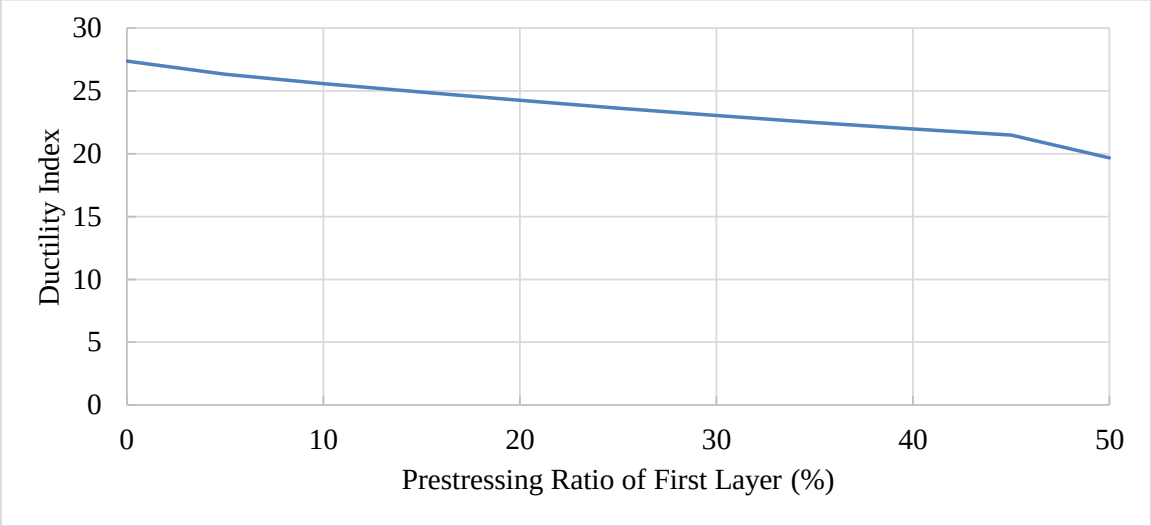

Figure 7-5. Ductility Index (First Layer Analysis)

Recall that the goal of the analytical program is to determine the optimal prestressing layout of the girder that meets both serviceability and ultimate limit states while maximizing ductility. From the analysis of the first layer, it can be concluded that lowering the prestressing ratio of the bottom tendons improves the ductility for all cases, as it leaves more strain available for flexure in the tendons. The analysis also showed increased moment capacity for first layer prestressing ratios of 40 and 45 percent. However, for all specimens, the available compressive

stress at the bottom fiber of the girder is diminished due to the reduction in total prestressing force.

7.4 Effect of Prestressing Middle Bars

In order to compensate for the loss in compressive stress at the bottom fiber, the six non-prestressed bars in the web of the girder can be prestressed up to 50 percent of their ultimate capacity to improve the overall prestressing force. Recall that the compressive stress calculation is a function of the geometric properties of the section, as well as the total prestressing force and prestressing eccentricity. Prestressing the middle bars improves the total prestressing force while the prestressing eccentricity decreases. Since these two values are inversely related and multiplicative, there must exist an optimal prestressing layout of the middle bars that maximizes the available compressive stress.

A short study was conducted using six specimens from the first layer analysis to determine the optimal prestressing layout of the middle bars. The first layer of middle bars were prestressed to 50 percent, and the available compressive stress was recorded for all specimens. The procedure was repeated adding the second layer of middle bars prestressed to 50 percent and so on. The results, displayed in Table 7-4, show that the available compressive stress improves as the number of layers of prestressed middle bars increases. However, every specimen shows that the increase in compressive stress between prestressing only two and all three layers of middle bars is negligible.

Table 7-4. Effect of Prestressing Middle Bars

	Number of Middle Bar Layers Prestressed to 50 Percent	Prestressing Ratio of First Layer (%)					
		0	10	20	30	40	50
Available Compressive Stress, MPa (ksi)	1	8.57 (1.243)	9.43 (1.367)	10.29 (1.492)	11.15 (1.617)	12.01 (1.742)	12.87 (1.866)
	2	8.83 (1.281)	9.69 (1.406)	10.55 (1.530)	11.41 (1.655)	12.27 (1.780)	13.13 (1.905)
	3	8.85 (1.283)	9.70 (1.407)	10.56 (1.532)	11.42 (1.657)	12.29 (1.782)	13.14 (1.906)
Improvement in Compressive Stress (%)	1	6.41	5.74	5.25	4.84	4.49	4.14
	2	9.67	8.75	7.93	7.30	6.77	6.31
	3	9.84	8.83	8.07	7.43	6.89	6.37

Considering that prestressing the bars can be problematic, as discussed in Chapter 4, it is recommended that only the first two layers of middle bars be prestressed to 50 percent to compensate for the loss in available compressive stress and improve constructability. From this point, the subsequent specimens were analyzed with the first and second layers of middle bars prestressed to 50 percent of their ultimate capacity to provide the largest possible compressive stress at the bottom fiber of the girder.

7.5 Second Layer Analysis

The next step was to fix the prestressing ratio of the first layer to a value less than 50 percent, and vary the second layer. The optimal prestressing layout, and the effect that the first layer will have on the performance of the girder, is difficult to speculate at this point in the analysis. Therefore, the prestressing ratio of the first layer was fixed to 0 percent while the second layer was varied from 0 to 50 percent with a 5 percent incremental step. The moment-curvature relationship and compressive stress was recorded, and the section was analyzed again with the first layer's prestressing ratio increased to 5 percent. The analysis continued for all 121 unique combinations of first and second layer prestressing ratios.

The available compressive stress for each specimen is displayed in Figure 7-6. The prestressing ratio of the first and second layer is presented in the legend and horizontal axis respectively. The required compressive stress to satisfy serviceability limit states is also displayed by a horizontal line at a compressive stress of 12.4 MPa (1.79 ksi). As seen, there are five specimens that satisfy the serviceability limit states.

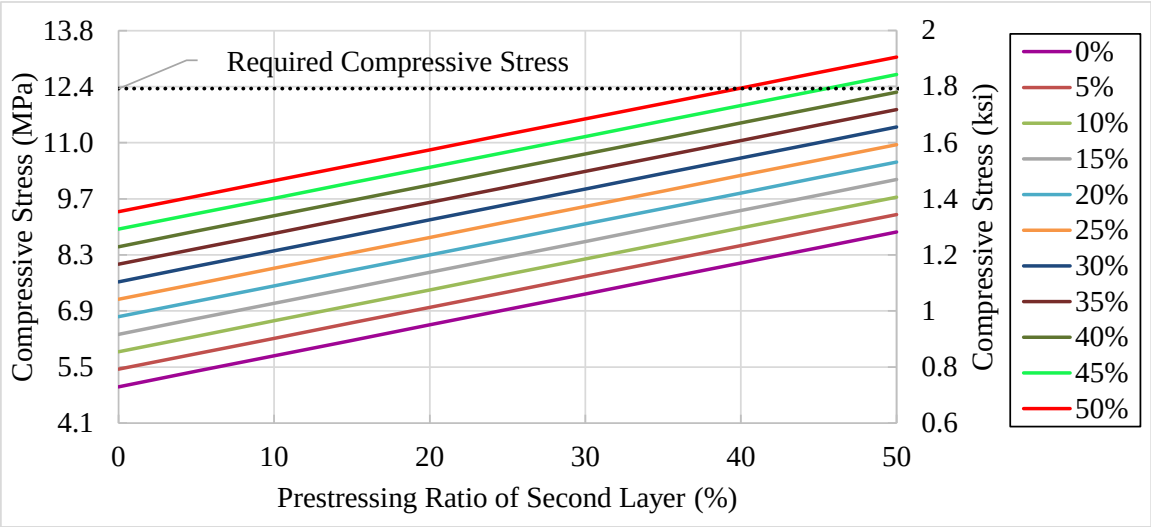

Figure 7-6. Available Compressive Stress (Second Layer Analysis)

The ultimate moment for all specimens is shown in Figure 7-7. All specimens with first layer prestressing ratios less than 45 percent show a similar behavior to that discussed in the first layer analysis. These specimens also show linearly improving moment capacity with increasing second layer prestressing ratios. The most interesting result of this analysis is that the ultimate moment is reduced for first layer prestressing ratios greater than 40 percent. This reduction in moment capacity can be attributed to the geometry of the section. When the prestressing ratio of the first layer is less than 45 percent, the third layer fails due to tendon rupture; however, when the prestressing ratio of the first layer reaches 45 percent, it becomes the controlling layer. As the controlling layer shifts down the section, the flexural strain

reduces for all layers excluding the controlling layer, reducing the moment capacity. Notice that for the case of the first layer prestressed to 50 percent, the controlling layer is always the first layer, causing the moment capacity to linearly increase independent of the second layer prestressing ratio.

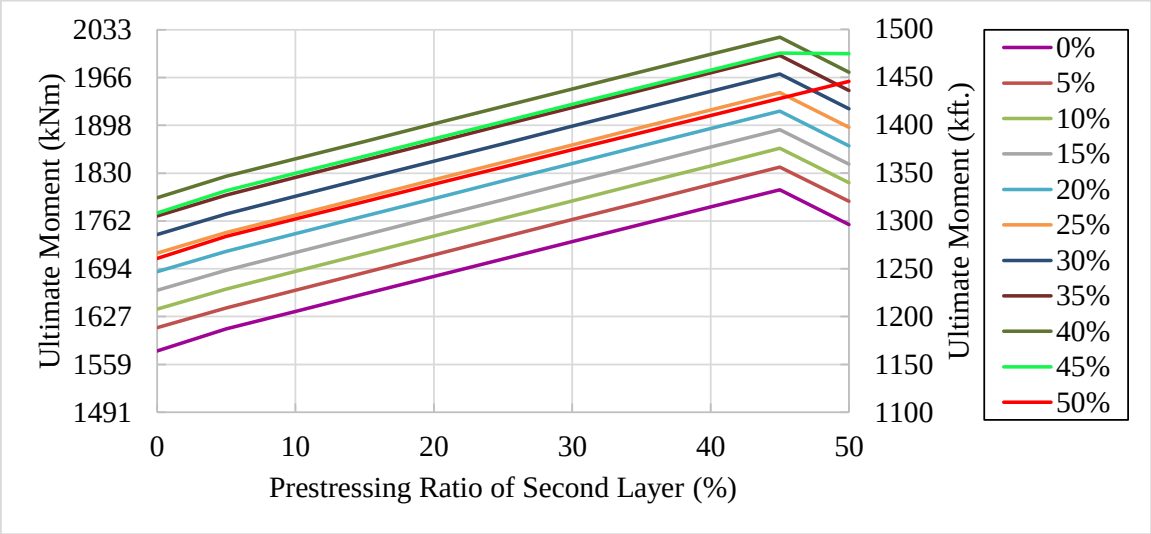

Figure 7-7. Ultimate Moment (Second Layer Analysis)

The ultimate curvature is presented in Figure 7-8. The behaviors of the ultimate moment and curvature are similar in the fact that specimens with first layer prestressing ratios greater than 45 percent diminish significantly in both areas. Other than the case where the first layer is prestressed to 50 percent, the ultimate curvature for every specimen shows three distinct stages.

The first stage features a small decrease in ultimate curvature when the second layer is prestressed between 0 and 5 percent. Recall that the ultimate curvature is a function of the flexural strain of the controlling layer and neutral axis location of the flexural strain (Equation 6-16). Given that the controlling layer does not change in the first stage, the neutral axis location must be the cause of change. The compressive force on the girder is a function of the

average prestressing ratio of the prestressed tendons only. When any layer is prestressed to 0 percent, that layer is excluded from the average prestressed ratio calculation. Hence, second layer prestressing ratios from 0 to 5 percent show a significant drop in average prestressing ratio, which increases the compressive force. Since the controlling layer's depth and flexural strain must remain constant during the first stage, the neutral axis is forced to move up the section, decreasing the ultimate curvature

The second stage includes a gradual rise in ultimate curvature when the second layer is prestressed between 5 and 45 percent. The second stage can be attributed to the gradual increase in total prestressing force. In order to maintain equilibrium the compressive force must increase with the increasing tensile force. Unlike the first stage, the average prestressing ratio is gradually increasing. This combination causes the neutral axis to move down the section, increasing the ultimate curvature.

The third stage consists of a significant decrease in ultimate curvature for second layer prestressing ratios between 45 and 50 percent. This stage is caused by the controlling layer shifting from the third layer to the second layer. From Equation 6-16 it is clear that as the controlling layer moves down the section, the ultimate curvature will diminish. This can also be seen in the examination of the cases of first layer prestressing ratios greater than 40 percent.

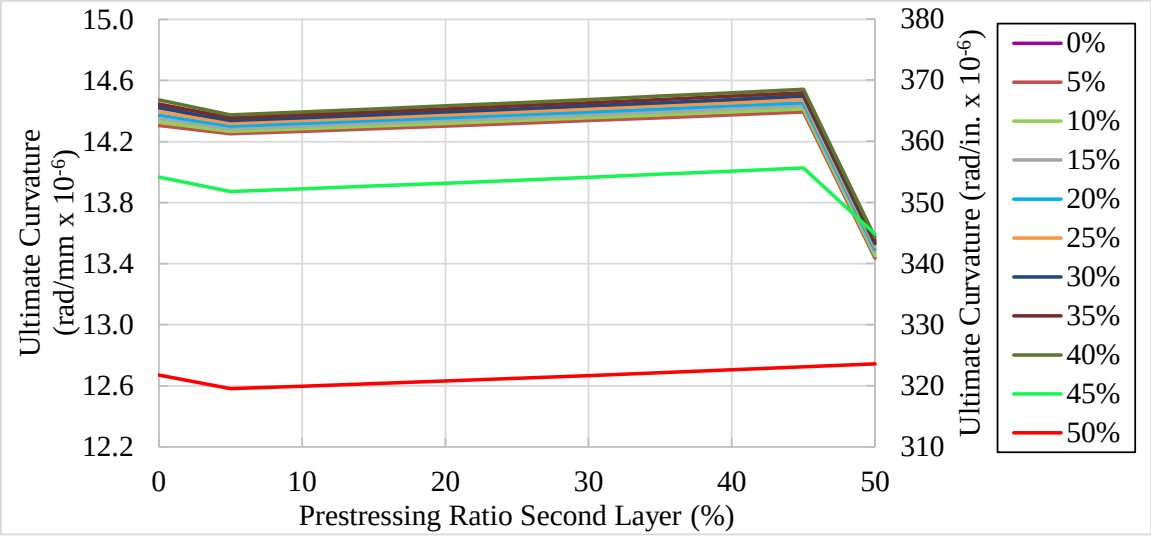

Figure 7-8. Ultimate Curvature (Second Layer Analysis)

Due to the fact that analyzing the third layer would require 1331 unique prestressing combinations for the first three layers, the results were filtered using the acceptance criteria that included any specimen that showed improved moment capacity and ductility when compared to the controlling specimen. Additionally, any specimen where the available compressive stress is reduced by less than 15 percent was accepted since limited cracking under service loads can be acceptable for partially prestressed sections. Nine specimens were selected that satisfied the acceptance criteria and their properties are summarized in Table 7-5. Generally, it can be seen that the specimens with lower prestressing ratios have better ductility, while specimens with higher prestressing ratios have more strength, as shown in Figure 7-9.

Table 7-5. Accepted Specimens (Second Layer Analysis)

Specimen #	1	2	3	4	5	6	7	8	9
f_{pi}/f_{pu} of 1st, 2nd Layer (%)	25, 45	30, 40	30, 45	35, 35	35, 40	35, 45	40, 40	40, 45	45, 45
M_{cr}, kNm (kft.)	991 (731)	994 (733)	1017 (750)	998 (736)	1020 (752)	1043 (769)	1047 (772)	1070 (789)	1096 (808)
Ψ_{cr}, rad/mm×10^{-6} (rad/in.×10^{-6})	0.58 (14.8)	0.58 (14.8)	0.60 (15.2)	0.59 (14.9)	0.60 (15.2)	0.61 (15.6)	0.61 (15.6)	0.63 (16.0)	0.64 (16.4)
M_n, kNm (kft.)	1944 (1434)	1946 (1435)	1970 (1453)	1947 (1436)	1973 (1455)	1997 (1473)	1998 (1474)	2023 (1492)	2000 (1475)
Ψ_n, rad/mm×10^{-6} (rad/in.×10^{-6})	14.44 (367)	14.44 (367)	14.46 (367)	14.44 (367)	14.46 (367)	14.49 (368)	14.49 (368)	14.51 (369)	14.00 (356)
f_{bp}, MPa (ksi)	10.62 (1.54)	10.62 (1.54)	11.03 (1.60)	10.69 (1.55)	11.10 (1.61)	11.45 (1.66)	11.51 (1.67)	11.86 (1.72)	12.34 (1.79)
Gain in Ψ_n, (%)	13.78	13.78	13.94	13.78	13.94	14.12	14.12	14.29	10.31
Gain in M_n (%)	5.06	5.15	6.48	5.24	6.57	7.89	7.98	9.31	8.07
Loss in f_{bp} (%)	14.20	13.79	10.72	13.39	10.31	7.24	6.83	3.75	0.27

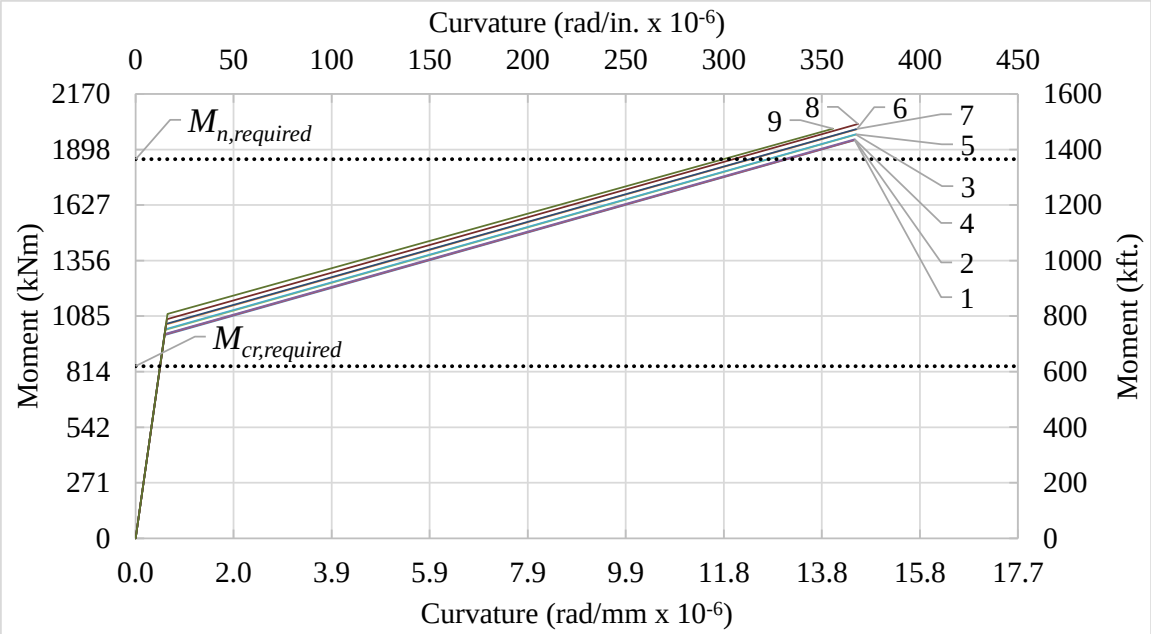

Figure 7-9. Moment-Curvature Relationship (Second Layer Analysis)

7.6 Third Layer Analysis

The nine specimens that met the acceptance criteria in the second layer analysis were considered in the analysis of the third layer. As before, the prestressing ratio of the third layer was varied from 0 to 50 percent with a 5 percent incremental step. The first and second layer prestressing ratios were held constant to values corresponding to one of the specimens that met the acceptance criteria of the second layer analysis.

The available compressive stress for all nine specimens is displayed in Figure 7-10. As discussed, none of the specimens satisfy the serviceability limit states; however, since the section is only partially prestressed, minor cracking can be acceptable. As seen in previous analyses, the compressive stress at the bottom fiber of the girder improves linearly with increasing prestressed ratio of the third layer. However, unlike the previous analyses, there is more separation between the compressive stresses. The compressive stresses can be allocated into five sets. The separation between the sets is based on the total prestressing force. The average prestressing ratios between the first and second layers is respectively, 45, 42.5, 40,

37.5, and 35 percent. Hence, the specimens with the highest cracking moment are those with the highest average prestressing ratio between the first and second layers.

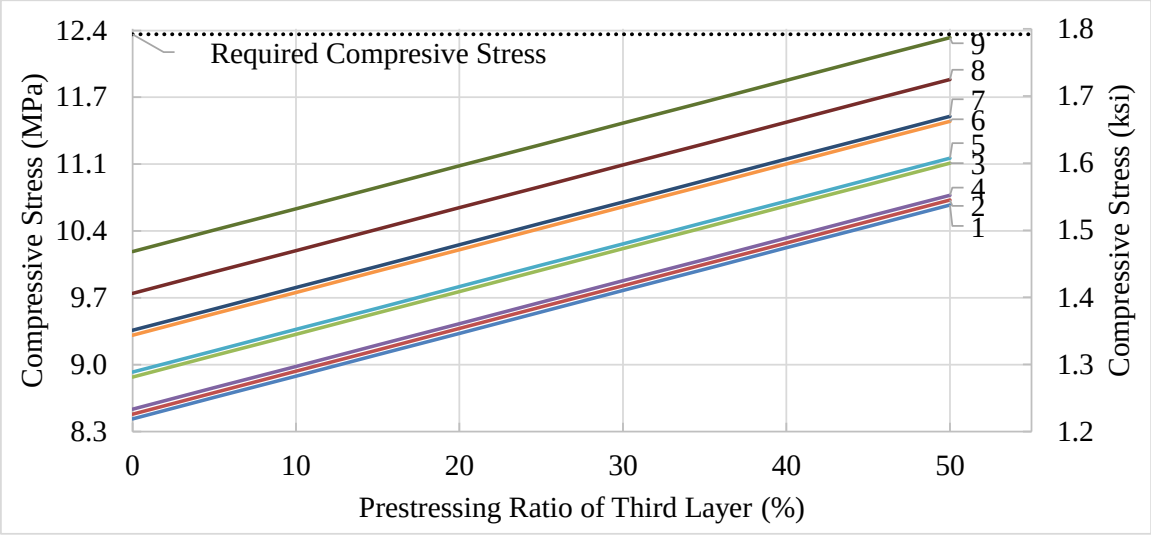

Figure 7-10. Available Compressive Stress (Third Layer Analysis)

The ultimate moment for all considered specimens is presented in Figure 7-11. The most interesting result is the fact that the specimen that has the largest moment capacity has a prestressing layout of 35, 40, and 45 percent for the first three layers, respectively. This specimen has a moment capacity of 1990 kNm (1468 kft.) which is significantly greater than the controlling specimen.

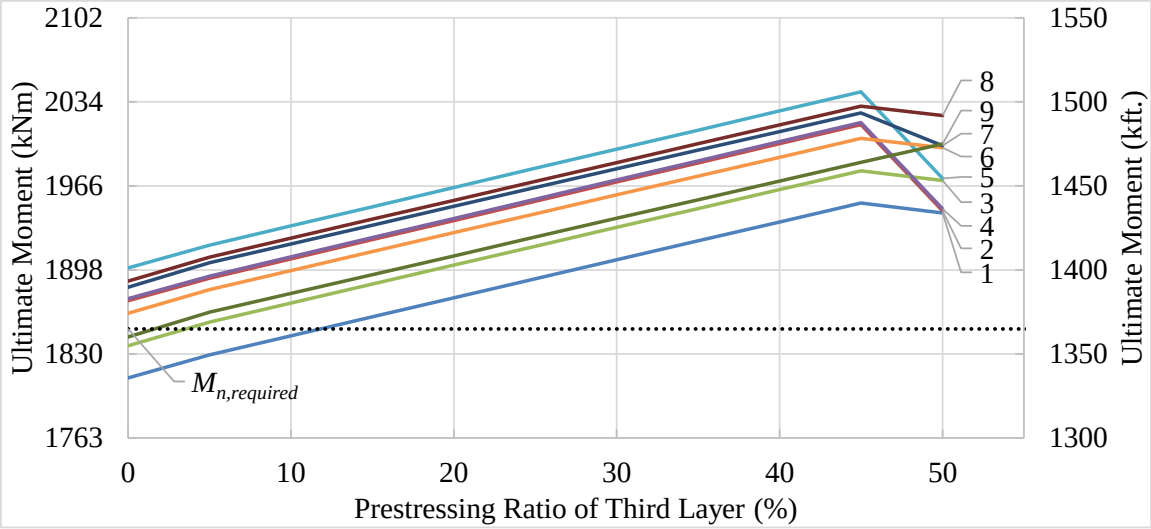

Figure 7-11. Ultimate Moment (Third Layer Analysis)

The ultimate curvature for all considered specimens is shown in Figure 7-12. The behavior of the ultimate curvature is similar to that of the cracking moment in the fact that there are large separations between the sets of specimens, and the specimens in each set are very close together. However, it is clear that there is one specimen that features the greatest improvement in ultimate curvature. This is the same specimen that has the greatest moment capacity improvement with prestressing ratios of the first three layers being 35, 40, and 45 percent, respectively.

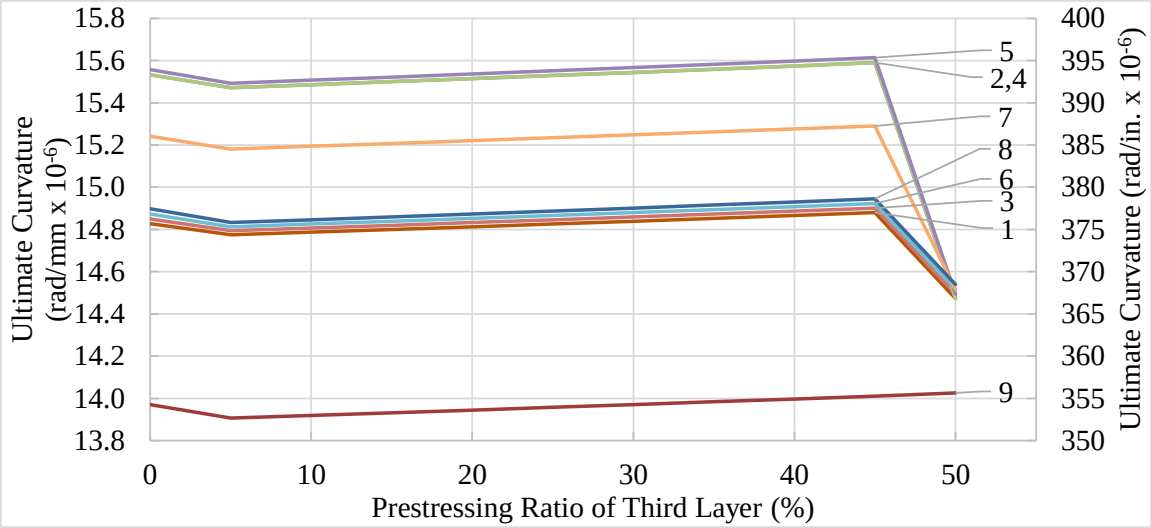

Figure 7-12. Ultimate Curvature (Third Layer Analysis)

The results were filtered as before using the acceptance criteria of improved moment capacity and ductility, along with less than 15 percent reduction in compressive stress. The analysis shows that there are 35 unique specimens that meet the acceptance criteria; therefore, it was determined that analyzing the fourth layer of the section would present diminishing returns, so the analytical study was terminated.

7.7 Optimal Prestressing Layout

The analytical program showed that the prestressing layout corresponding to first, second, and third layer prestressing ratios of 35, 40, and 45 percent, respectfully maximizes the strength and ductility of the girder producing an ultimate moment and curvature of 2042 kNm (1506 kft.) and 15.6 rad/mm$\times 10^{-6}$ (395.4 rad/in.$\times 10^{-6}$), respectively. These values correspond to an increase of 10 and 22 percent in ultimate moment and curvature, respectively. However, this prestressing layout also reduces the compressive stress at the bottom fiber of the girder to 10.9 MPa (1.575 ksi) corresponding to a 12 percent reduction. Since the girder is only partially prestressed, this reduction can be considered acceptable.

Although the analytical program resulted in specimens that showed a lesser reduction in compressive stress, prestressing the bars to a lower level is more reliable considering the

constructability issues discussed in Chapter 4. For this reason, the optimal prestressing layout consists of first, second, and third layer prestressing ratios of 35, 40, and 45 percent, respectfully, along with the first two layers of middle bars prestressed to 50 percent of their ultimate capacity. The optimal prestressing layout is shown in Figure 7-13 and the comparison between the optimal prestressing layout and the control specimen is displayed in Table 7-6.

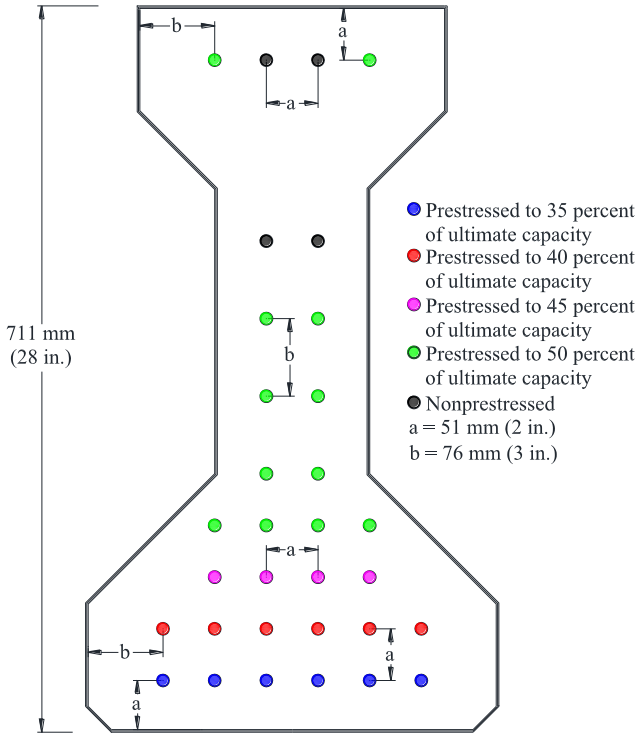

Figure 7-13. Optimal Prestressing Layout

Table 7-6. Comparison of Optimal Prestressing Layout to Control Specimen

	Optimal Prestressing Layout	Control Specimen
Cracking Moment, kNm (kft.)	1007.0 (742.7)	1097.3 (809.3)
Cracking Curvature, rad/mm×10^{-6} (rad/in.×10^{-6})	0.591 (15.0)	0.646 (16.4)
Ultimate Moment, kNm (kft.)	2042.0 (1506.0)	1851.0 (1364.9)
Ultimate Curvature, rad/mm×10^{-6} (rad/in.×10^{-6})	15.6 (395.4)	12.7 (322.4)
Ductility Index	26.3	19.7

7.8 Improving Compressive Stress

As discussed, the control specimen meets the serviceability limit states, but reducing the prestressing ratio of the lower layers causes the available compressive stress at the bottom fiber of the girder to be insufficient. Since the girder is only partially prestressed, minor cracking can be accepted under service loads. However, the compressive stress can improve further by adjusting the geometric placement of the bars.

The third layer of reinforcement contains only four AFRP bars as shown in Figure 7-13. The figure also shows that the minimum cover is only 50.8 mm (2 in.); therefore, two AFRP bars can be added to the third layer to further improve the compressive stress at the bottom fiber. Using the optimal prestressing layout and adding two bars to the third layer gives a compressive stress of 11.9 MPa (1.719 ksi), which corresponds to an increase of nearly 10 percent compared to the same prestressing layout with only four bars in the third layer.

Another solution to improve the compressive stress includes decreasing the vertical spacing of the middle bars in the web. Decreasing the vertical spacing between the middle bars in the web from 76.2 mm (3 in.) to 50.8 mm (2 in.) improves the compressive stress of the optimal prestressing layout to 11.1 MPa (1.61 ksi). This corresponds to an increase of about 2.5 percent compared to the same layout with middle bars spaced at 76.2 mm (3 in.). However, this solution may be much more difficult to implement, since it may require a custom stressing bed with the

correct dimensions. Combining both of these solutions gives a compressive stress of 12.1 MPa (1.76 ksi) corresponding to a reduction in compressive stress of only 2.1 percent.

Finally, the two prestressed bars in the top flange of the girder can be non-prestressed. This change improves the compressive stress of the optimal prestressing layout to 11.4 MPa (1.65 ksi) corresponding to an increase of about 5 percent. Combining all of the solutions gives a compressive stress of 12.7 MPa (1.84 ksi) which exceeds the control specimen, thus satisfying the serviceability limits.

8 CONCLUSION

An FRP prestressed concrete girder (AASHTO I-girder Type I) was experimentally investigated under full-scale flexure and shear tests to evaluate its structural performance. AASHTO LRFD criteria were used to evaluate the experimental results. The results were also compared with a companion control specimen prestressed with conventional steel strands. The major conclusions for the experimental research are as follows:

- The experimental results show that AFRP bars can successfully replace conventional steel prestressing strand and rebar, while also satisfying the serviceability limit states.
- The AFRP prestressed specimen showed a moment capacity of M_n = 1563.2 kNm (1153 kft.) exceeding the maximum factored load of M_u = 1326 kNm (978 kft.) by about 18 percent.
- The cracking moment of the experimental specimen was unable to exceed the moment caused by the unfactored dead and live loads. For this reason, the experimental specimen was categorized as a partially prestressed beam allowing limited cracking to occur under service loads.
- It was difficult to provide a fully prestressed girder due to the limited capacity of the prestressing anchorage system used for AFRP bars.
- Due to the fact that the AFRP specimen was partially prestressed, the moment-curvature showed clear pre-cracking, cracking, and post-cracking stages. The deflection of the girder was also very close to the serviceability limit per the AASHTO LRFD *Bridge Design Specification* (2010). The live load deflection of the experimental specimen was only 3.8 mm (0.15 in.) less than the allowable deflection under service loads; therefore, the deflection should be examined as a critical design parameter.
- The AFRP prestressed specimen failed due to AFRP rupture at the bottom flange of the girder unlike the control specimen, which failed due to concrete crushing. The AFRP specimen also showed much more cracking prior to failure when

compared to the conventional steel specimen. This extensive cracking can be an obvious warning sign of impending failure.

- The shear capacity of the experimental specimen was nearly twice the maximum factored shear load according to AASHTO LRFD *Bridge Design Specification* (2010). The failure mode of both shear tests was crushing of the girder's web, and the AFRP specimen showed a similar shear capacity and cracking pattern when compared to the conventional steel prestressed specimen.
- Full composite action was achieved by the combination of AFRP R-bars and high strength steel bolts used as shear studs at the girder-to-deck interface.
- The placement of the AFRP bars was much easier due to the low weight of the bars when compared to steel prestressing strand.
- The main constructability issues occurred during the prestressing operation when a few AFRP bars failed due to tendon rupture from possible surface damage during transportation. Hence, an appropriate anchorage system that suits both the design and construction requirements should be used.
- The large deflections and significant cracking shown in the experimental analysis of the AFRP specimen could be very appealing to the design engineer because it is an obvious sign of impending failure.

The girder (AASHTO I-girder Type I) was also analytically investigated to determine an optimal prestressing layout that will improve performance at the ultimate state, while satisfying serviceability limits. The results were compared with a control specimen to evaluate the analytical results. The major conclusions for the analytical study are as follows:

- Improving the ductility could prove beneficial where ductility demands can be challenging, for instance, at bridge piers in seismic zones.
- The prestressing layout of the control specimen can be successfully changed to create a section that improves performance at the ultimate state, while sufficiently satisfying the serviceability limits.

- The optimal prestressing layout consists of first, second, and third layer prestressing ratios of 35, 40, and 45 percent, respectfully, along with the first two layers of middle bars prestressed to 50 percent of their ultimate capacity.

- The ultimate moment and curvature of the optimal prestressing layout was equal to M_n = 2042 kNm (1506 kft.) and Ψ_n = 15.6 rad/mm×10^{-6} (395.4 rad/in.×10^{-6}), which is about 10 and 22 percent greater than the control specimen, satisfying the ultimate limit state.

- The optimal prestressing layout shows a reduction in available compressive stress at the bottom fiber of the girder of only 12 percent compared to the control specimen. This reduction in compressive stress will result in minor cracking under service loads which can be acceptable for partially prestressed sections.

- The performance of the specimen can also be improved by changing the geometric placement of the tendons, but could be difficult to implement.

The following items are recommended for further research and future work:

- The long-term structural performance of the AFRP girder needs to be verified.
- Due to the fact that the AFRP R-bars and high strength steel shear bolts provided sufficient girder-to-deck shear resistance, it is recommended that further research investigate if the R-bars are adequate to resist the entire shear force at the girder-to-deck interface.
- A reliable method to compute the shear capacity is needed.
- A compatible strut and tie model is recommended to be studied for FRP application.
- Experimental verification of the optimal prestressing layout should be performed and compared to the analytical program.

REFERENCES

AASHTO. (2010). "AASHTO LRFD Bridge Design Specification." 5th Edition, Washington, D.C.

Abdelrahman, A. A., Tadros, G., & Rizkalla, H. S. (1995). "Test Model for the First Canadian Smart Highway Bridge." *ACI Structural Journal*, 92(4): pp. 451–458.

Abdelrahman, A. A., & Rizkalla, H. S. (1997). "Serviceability of Concrete Beams Prestressed by Carbon Fiber-Reinforced-Plastic Bars." *ACI Structural Journal,* 94(4): pp. 447-454.

Al-Mayah, A., Khaled, S., & Plumtree, A. (2001a). "Experimental and Analytical Investigation of a Stainless Steel Anchorage for CFRP Prestressing Tendons." *PCI Journal*, 46(2): pp. 88-100.

Al-Mayah, A., Khaled, S., & Plumtree, A. (2001b). "Mechanical Behavior of CFRP Rod Anchors under Tensile Loading." *Journal of Composites for Construction*, 5(2): pp. 128-135.

Al-Mayah, A., Khaled, S., & Plumtree, A. (2005). "Effect of Sandblasting on Interfacial Contact Behavior of Carbon-Fiber-Reinforced Polymer-Metal Couples." *Journal of Composites for Construction*, 9(4): pp. 289-295.

Al-Mayah, A., Khaled, S., & Plumtree, A. (2006). "Development and Assessment of a New CFRP Rod-Anchor System for Prestressed Concrete." *Applied Composite Materials,* 13(5): pp. 321-334.

Al-Mayah, A., Khaled, S., & Plumtree, A. (2007). "Novel Anchor System for CFRP Rod: Finite-Element and Mathematical Models." *Journal of Composites for Construction,* 11(5): pp. 469-476.

Bennitz, A., & Schmidt, J. W. (2012). "Failure Modes of Prestressed CFRP Rods in a Wedge Anchorage Set-up." *ACIC 2009,* Proceedings of the 4th International Conference: pp. 104-114.

Dolan, C.W., Nanni, A., Hamilton, H.R., & Bakis, C.E. (2001). "Design Recommendations for Concrete Structures Prestressed with FRP Tendons." *FHWA, V. III: FRP Prestressing for Highway Bridges,* Cont. DTFH61-96-C-00019.

Dolan, C.W., & Swanson, D. (2001). "Development of Flexural Capacity of a FRP Prestressed Beam with Vertically Distributed Tendons." *Composites Part B Engineering*, 33(1): pp. 1-6.

Karthik, M.M., & Mander, J.B. (2011). "Stress-Block Parameters for Unconfined and Confined Concrete Based on a Unified Stress-Strain Model." *Journal of Structural Engineering, ASCE*, 137(2): pp. 270-273.

Lu, Z. (1998). "Flexural Performance of Fiber Reinforced Polymer Prestressing Bars." M.S. Thesis, Pennsylvania State University, University Park, PA.

NACE. (2013). "Corrosion Cost of Highways and Bridges." Web. 2 September. 2014. < http://www.nace.org/Corrosion-Central/Industries/Highways-and-Bridges/>.

Nanni, A., Yan, X., & Myers, J.J. (2000). "An Assessment of Flexural Behavior of CFRP Prestressed Beams Subjected to Incremental Static Loading." *FHWA, V. III: FRP Prestressing for Highway Bridges*, Cont. DTFH61-96-C-00019.

Park, R., & Paulay, T. (1975). "Reinforced Concrete Structures." *John Wiley & Sons*, New York.

Pincheira, J., & Woyak, J. (2001). "Anchorage of Carbon Fiber Reinforced Polymer (CFRP) Tendons using Cold-Swaged Sleeves." *PCI Journal*, 46(6): pp. 100-111.

Pirayeh Gar, S. (2012). "Structural Performance of a Full-Depth Precast Bridge Deck System Prestressed and Reinforced with AFRP Bars." PhD Dissertation, Texas A&M University, College Station, TX.

Pirayeh Gar, S., Head, M. H., Hurlebaus, S., & Mander, J. B. (2013). "Comparative Experimental Performance of Bridge Deck Slabs with AFRP and Steel Precast Panels." *Journal of Composites for Construction*, 17(6), pp. 1-9.

Pirayeh Gar, S., Hurlebaus, S., Mander, J. B., Cummings, W., Prouty, J. M., & Head, M. H. (2014). "Sustainability of Transportation Structures using Composite Material to Support Trade and Growth." *Southwest Region University Transportation Center*, SWUTC/14/600451-00009-1.

Shahawy, M.A., & Beitelman, T. (1995). "Static Flexural Response of Members Pretensioned with Multiple Layered Aramid Fiber Tendons." *Journal of Composites Part B: Engineering*, 27(3-4): pp. 253-261.

Shrive, N. G. (2000). “Prestressing Anchorage System for Fiber Reinforced Plastic Tendons.” U.S. Patent 6,082,063.

Trejo, D., Hueste, M. B., Kim, Y. H., & Atahan, H. (2008). “Characterization of Self-Consolidating Concrete for Design of Precast, Prestressed Bridge Girders.” Report No. FHWA/TX-09/0-5134-2, *Texas Transportation Institute,* College Station, TX, pp. 1-364.

Zhang, B., & Benmokrane, B. (2004). “Design and Evaluation of a New Bond-type Anchorage System for Fiber Reinforced Polymer Tendons.” *Canadian Journal of Civil Engineering,* 31(1): pp. 14-26.